CARBON-BASED MAGNETIC NANOHYBRID MATERIALS FOR POLYMER COMPOSITES AND ELECTROCHEMICAL ENERGY STORAGE AND CONVERSION

A Dissertation
Presented to
The Academic Faculty

by

Il Tae Kim

In Partial Fulfillment
of the Requirements for the Degree
Doctor of Philosophy in the
School of Materials Science and Engineering

Georgia Institute of Technology
December 2011

CARBON-BASED MAGNETIC NANOHYBRID MATERIALS FOR POLYMER COMPOSITES AND ELECTROCHEMICAL ENERGY STORAGE AND CONVERSION

Approved by:

Dr. Rina Tannenbaum, Advisor
School of Materials Science and Engineering
Georgia Institute of Technology

Dr. Karl Jacob, Advisor
School of Materials Science and Engineering
Georgia Institute of Technology

Dr. Hamid Garmestani
School of Materials Science and Engineering
Georgia Institute of Technology

Dr. Allen Tannenbaum
School of Electrical and Computer Engineering
Georgia Institute of Technology

Dr. Gleb Yushin
School of Materials Science and Engineering
Georgia Institute of Technology

Date Approved: October 28, 2011

ACKNOWLEDGEMENTS

First of all, I would like to express the deepest appreciation to the God for all of the things. My advisors, Dr. Rina Tannenbaum and Dr. Karl Jacob, have guided me through my graduate work, and helped and encouraged me to do my best; thus, to be a researcher I am today. My thesis committees, Dr. Hamid Garmestani, Dr. Allen Tannenbaum, and Dr. Gleb Yushin, have also given me invaluable suggestions and encouragement through the course of this study.

I would like to thank Dr. Justin Schwartz for the assistance with superconducting quantum interference device, Dr. Alexandre Magasinski for his great help and guidiance to complete my secondary battery study, Dr. Rosario Gerhardt and Dr. Chunqing Peng for the impedance analyzer study, Dr. David Safranski for tensile property study, Mr. Ji Hoon Lee for differencial scanning calorimetry study, and Mr. Wei Lin for the assistance with furance. During the work, I have received great assistance from my group members: Dr. Kasi David, Dr. Erin Camponeschi, Dr. Cantwell Carson, Dr. Lex Nunnery, Dr. Larry Pranger, Mrs. Jung Hwa Park, and Mr. Rolando Gittens. I also would like to thank all of my friends who've come and gone throughout my years here at Georgia Tech: Dr. Hyunhyub Ko, Dr. Hangi Chae, Dr. Sungwon Ma, Dr. Young Ho Choi, Dr. Sehoon Chang, Dr. Min Ku Song, Mr. Beom-Jin Yoon, Mr. Min Sang Park, Dr. Seung Geol Lee, Mr. Ikjun Choi, Mr. Yun Sang Kim, Mr. Dohyun Park, Mr. Jung Tae Lee, Ms. Parisa Pooyan, and Dr. Dongsheng Li for their help and friendship.

Last but not least, I would like to deeply thank to my parents, my in-laws, sister, and brother-in-law for their support and sincere pray for me, and to my lovely wife for her patience, great love, and encouragement.

TABLE OF CONTENTS

LIST OF TABLES

LIST OF FIGURES

SUMMARY

Graphene, the parent of all graphitic forms including fullerene, carbon nanotubes, and graphite, is a two dimensional building material for carbon materials of all other dimensionalities. Among them, graphene and carbon nanotubes have been extensively studied in such fields as polymer composites and electrochemical energy storage and conversion due to their high specific surface area, excellent conductivity, good stability, high electron mobility, and good mechanical performance. Thus, the goal of this study is to achieve improved physical properties of polymer composites and enhanced electrochemical performance of composite electrodes for lithium ion batteries by utilizing and modifying carbon nanotubes and graphene, respectively.

When carbon nanotubes are well-dispersed in polymer matrices, it exhibits improved mechanical, electrical, and thermal properties. Furthermore, when they are both dispersed and aligned, it could also show much enhanced anisotropic physical properties. There are various methods to obtain the alignment of carbon nanotubes in polymer matrices, which include electric, magnetic, electro-spinning, spin casting, or shear flow. Among them, the magnetic field is one of the efficient methods for aligning carbon nanotubes. However, the magnetic susceptibility of carbon nanotubes is very low; thus, strong magnetic field strength is required. One way to obtain facile alignment of carbon nanotubes by applying an external magnetic field is to engineer magnetic hybrid nanostructures, which illustrate that carbon nanotubes are tethered with magnetic nanoparticles, such as maghemite (γ-Fe_2O_3) or magnetite (Fe_3O_4). For obtaining the hybrid nanostructures, a novel and easy synthesis method, modified sol-gel process, was

developed, from which individual and separate magnetic nanoparticles could be obtained on the surface of carbon nanotubes. As-prepared magnetic carbon nanotubes (m-CNTs) showed strong magnetic response to a low magnetic field (< 0.3 T) and were aligned parallel to the direction of magnetic field in polymer matrices. If a sufficiently large homogeneous magnetic field is applied, the magnetic moments of the nanoparticles align in parallel, and the resulting dipolar interactions are sufficiently large to overcome thermal motion and to reorient the m-CNTs favoring the formation of chains of aligned carbon nanotubes. These chainlike structures are formed by connecting the m-CNTs in line, touching each other in a head-to-tail fashion, i.e., north to south pole. Since the north and south poles of the dipolar nanomagnets attract each other, while particles coming close to each other side by side with the magnetization direction parallel will repel each other, the m-CNTs could be dispersed as well as aligned. Moreover, due to this end-to-top connectivity, which generates higher aspect ratio, improved anisotropic electrical and mechanical properties could be realized.

Li-ion batteries (LIBs) have been widely used as power sources for portable electronic devices and electronic vehicles, and attracted a variety of attention due to their high energy density and power density. In this system, electrode materials are very significant for the enhanced electrochemical performance. Graphene has been widely used as anode materials for LIBs due to its outstanding properties. However, it has characteristics such as large irreversible capacity loss, low initial columbic efficiency, and rapid capacity fading. One efficient way to improve the capacity and cycle performance of LIBs is to introduce graphene-based hybrid nanostructured electrodes with another component being popular LIB materials such as oxide, metal, and carbon.

Based on this perspective, graphene/iron oxide hybrid nanostructures were developed, where modified sol-gel process for the synthesis was adopted again, and its morphology represented that mono-disperse and individual magnetic nanoparticles were tethered on the graphene sheets as observed in carbon nanotube system. The as-prepared graphene/iron oxide composite, graphene/γ-Fe_2O_3, were used as an anode material for LIBs. This hybrid nanomaterial, due to their specific morphology and characteristics, exhibited improved large reversible capacity, long cycle life, and good rate performance.

CHAPTER 1

INTRODUCTION

1.1 Carbon Nanotubes (CNTs)

It was not until 1991 that Sumio Iijima discovered and launched the research area of carbon nanotubes. Iijima found that carbon fibers in a carbon arc were hollow and on the nanoscale in size.[1] This led to the expansion and continuation of research on the nanotubes, which has allowed for numerous development and achievement in a variety of fields of study such as catalyst synthesis, medicine, and electronics.[2-4]

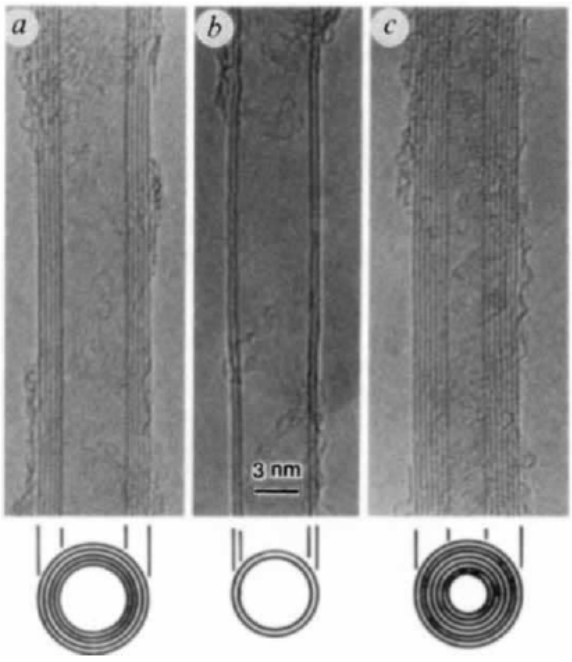

Figure 1.1. Electron micrographs of microtubules of graphitic carbon. Parallel dark lines correspond to the (002) lattice images of graphite. (a) Five graphitic sheets; (b) Two sheets; (c) Seven sheet tube.[1]

There are three different types of carbon nanotubes: single wall carbon nanotubes (SWNTs), double wall carbon nanotubes (DWNTs), and multi wall carbon nanotubes

(MWNTs). A SWNT with a diameter of 1-2 nm is comprised of a single graphene layer wrapped into a cylindrical shape, and hemispherical caps seal both ends of the tube. SWNT can be further divided into three classes; that is to say, zigzag, armchair, and chiral that depend on the arrangement of hexagons in their structures as shown in Figure 1.2.[5] On the contrary, MWNT consists of a number of graphene layers coaxially rolled together to form a cylindrical tube. Each carbon atom within the atomic layer of a graphene sheet is covalently bonded to three neighboring carbon atoms. Three sp^2 orbitals on each carbon form σ-bonds to three other carbon atoms. One 2p orbital remains unhybridized on each carbon; thus, these orbitals perpendicular to the plane of the carbon ring combine to form the π-bonds. The atomic interactions between the neighboring layers are the van der Waals forces.[6]

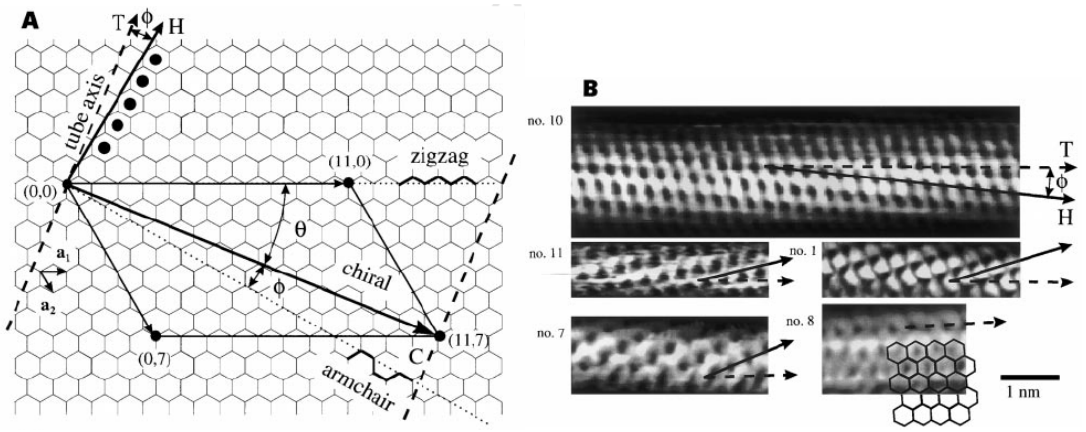

Figure 1.2. (a) The construction of a CNT from a single graphene sheet. Wrapping vectors along the dotted lines lead to tubes having zigzag or armchair. All other wrapping angles lead to chiral tubes whose wrapping angle is specified relative to either the zigzag direction (θ) or to the armchair direction ($\varphi=30^{o}$ - θ). Dashed lines are perpendicular to **C** and run in the direction of the tube axis designated by vector **T**. The vector **H** is perpendicular to the armchair direction and specifies the direction of nearest-neighbour hexagon rows. (b) Atomically resolved STM images of individual SWNTs. Tubes no. 10, 11, and 1 are chiral, whereas tubes no. 7 and 8 have a zigzag and armchair structure, respectively.[5]

1.1.1 Physical Properties of CNTs

1.1.1.1 Mechanical Properties of CNTs

The mechanical properties of CNTs originate from the strong C=C double bonds, which yield a very large Young's modulus in their axial direction (1.4 TPa for SWNTs).[7] CNTs have an expected elongation-to-failure of 20-30%, which, combined with their stiffness, projects to a tensile strength well above 100 GPa (for instance, steel: 1-2 GPa).[8] However, both Young's modulus and tensile strength are strongly reduced by the presence of defects in the graphitic walls of CNTs, such as Stone-Wales defects. Hence, experimental values tend to be considerably smaller than theoretical predictions. Because of their high aspect ratio, CNTs are also very flexible and thus potentially suitable for applications in composite materials that require anisotropic properties.[9]

1.1.1.2 Thermal Properties of CNTs

Theoretical works predicted room temperature thermal conductivities of individual SWNTs of up to 6600 W m^{-1} K^{-1}.[10] CNTs would therefore transmit nearly twice as much heat as isotopically pure diamond. Experimental studies give somewhat lower values, with Hone et al. reporting room temperature thermal conductivities of 300 W m^{-1} K^{-1} for bulk SWNTs and of 3000 W m^{-1} K^{-1} for individual MWNTs.[11]

1.1.1.3 Electrical Properties of CNTs

The electrical resistivity of CNTs is determined by the unique structure of graphite and the quantum mechanical properties associated with their one-dimensional character and small size, which results in the near-total elimination of electron collisions

(or scattering). Thus, CNTs are ballistic conductors, whose resistance is independent on the nanotube length. Furthermore, they can carry the highest current density of any known material, with reported measurement as high as 10^9 A cm^{-2}. For comparison, copper wires burn out at 10^6 A cm^{-2}.[12] Depending on their helicity and diameter, CNTs can be either metallic or semiconducting. Figure 1.3 shows the schematic diagram of how a hexagonal sheet of graphene is rolled to form a carbon nanotube.[13]

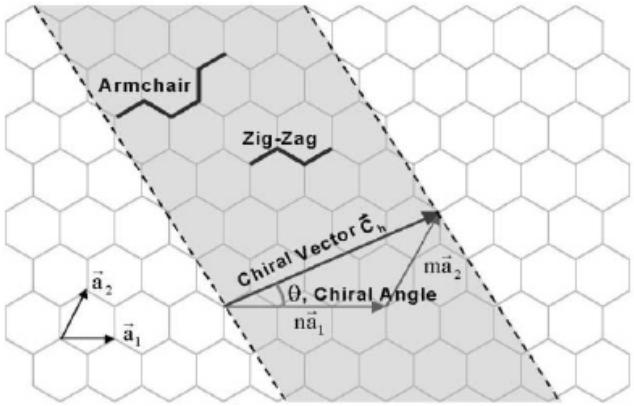

Figure 1.3. Schematic diagram showing how a hexagonal sheet of graphene is rolled to form a carbon nanotube.[13]

The various ways of rolling graphene into tubes are described by the tube chirality (or helicity or wrapping) as defined by the circumferential vector,

$$\vec{C}_h = n\vec{a}_1 + m\vec{a}_2$$

Where the integers (n, m) are the number of steps along the unit vectors ($\vec{a}_1$ and $\vec{a}_2$) of the hexagonal lattice. Using this (n, m) naming scheme, the three types of orientation of the carbon atoms around the nanotube circumference are specified as arm chair (n = m), zigzag (n = 0 or m = 0), or chiral (all others). This is of significance as

semiconducting SWNTs may perform better in applications that involve charge transfer processes, including sensors, field emission devices, and photocatalytic applications, while metallic CNTs are preferred as interconnects in electronic devices or as conductive filler in CNT-composites.

1.1.1.4 Optical Properties of CNTs

The optical properties of carbon nanotubes refer specifically to the absorption, photoluminescence, and Raman spectroscopy of carbon nanotubes. Spectroscopic methods offer the possibility of quick and non-destructive characterization of relatively large amounts of carbon nanotubes. In addition, carbon nanotubes exhibit intrinsic anisotropic optical properties. Orientation of carbon nanotubes can be determined through resonance enhanced Raman spectroscopy as a function of polarization direction.[14-17]

In summary, due to their remarkable mechanical, electrical, optical, and thermal properties, CNTs promise enormous potential for a variety of technological areas in the energy, information, aerospace, medicine, and chemical industries. The overall properties of CNTs in comparison with graphite are summarized in Table 1.1.

Table 1.1. Summary of physical properties of CNTs in comparison with graphite.[18, 19]

Property	MWNTs	SWNTs	graphite
Specific gravity [g cm^{-3}]	~ 1.8	~ 0.8	2.26
Strength [GPa]	10-60	50-500	
Elastic modulus [TPa]	~ 0.3-1	~ 1.4	1 TPa (in plane)
Resistivity [μΩ cm]	5-50		50 (in plane)
Thermal conductivity [W m^{-1} K^{-1}]	3000		3000 (in plane)
Thermal expansion [K^{-1}]	negligible		-1 x 10^{-6} (in plane) 29 x 10^{-6} (c-axis)
Thermal stability [^{o}C]	600-800 in air 2800 in vacuum		450-650 in air
Magnetic susceptibility [EMU g^{-1}]	22 x 10^{6} (perpendicular) 0.5 x 10^{6} (parallel)		0.5 x 10^{6} (parallel)

1.2 CNTs-Inorganic Hybrids

In general, CNTs possess large specific surface areas due to their hollow geometry, while their structural integrity and chemical inertness support high oxidation stability. In addition, they include other advantages like exceptional physical properties as discussed in the previous section. Therefore, due to CNTs' remarkable electrical, mechanical, and thermal properties, CNTs are able to promise enormous potential for various technological areas such as energy, aerospace, medicine, composite reinforcements, chemical sensors, or actuators. For the same reasons, they are promising building blocks for hybrid materials. The decoration of CNTs with various compounds and various structures could increase the tunability of their properties, such as their electrical and magnetic characteristics.[20, 21] Recently, various inorganic nanoparticles

have been attached to the external surface of CNTs or filled inside CNTs through several experimental methods.[22, 23] In this context, the control of the size of these tethered nanoparticles is of primary importance for the purpose of tailoring the physical and chemical properties of these hierarchical materials. Many CNTs-inorganic hybrid structures have been reported.[24-33] Thus, among various CNTs-inorganic hybrid structures, the following Chapter will address and focus on CNT/iron oxide hybrid structures.

1.2.1 Structure of Iron Oxide Nanoparticles

Maghemite (γ-Fe_2O_3) and magnetite (Fe_3O_4) are a type of spinel structure ($A^{2+}B_2^{3+}O_4^{2-}$), but they have an inverse spinel crystal structure. A normal spinel has the formula AB_2O_4 with A atoms in the tetrahedral sites and B atoms in the octahedral sites. Inverse spinels have B atoms in the tetrahedral sites and both A and B atoms in the octahedral sites as shown in Figure 1.4.[34] The unit cell of Fe_3O_4 has 56 ions including 24 Fe cations and 32 oxygen anions organized as $(Fe_8^{3+})_{Te}[Fe_8^{3+}Fe_8^{2+}]_{Oc}O_{32}^{2-}$ and maghemite has 53.3 ions including 21.33 ferric cations and 32 oxygen anions organized as $(Fe_8^{3+})_{Te}[Fe_{40/3}^{3+} \otimes_{8/3}]_{Oc}O_{32}^{2-}$. The arrangements of atoms in Fe_3O_4 and γ-Fe_2O_3 are similar with a slight difference in that the eight Fe^{2+} atoms in the octahedral sites of the Fe_3O_4 unit cell are replaced by 16/3 Fe^{3+} atoms and 8/3 vacancies in the unit cell.

Figure 1.5 shows the structure of maghemtie and magnetitie.[35] The main difference between the two species is the presence of ferric ions only in γ-Fe_2O_3, and both ferrous and ferric ions in Fe_3O_4. As a result, while the magnetic properties of Fe_3O_4 are superior, γ-Fe_2O_3 is more stable, since the iron cannot be further oxidized under ambient conditions. This renders γ-Fe_2O_3 easier to work with, especially in the presence of

organic solvents and organic ligands, and hence, has been widely used for magnetic storage in a variety of fields such as floppy disks and cassette tapes.

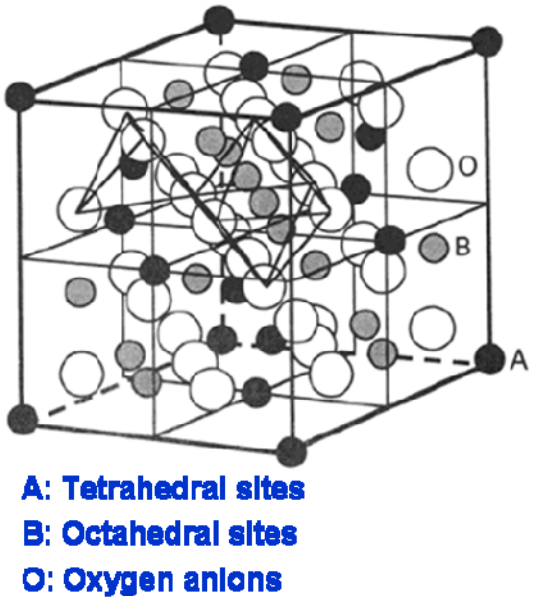

Figure 1.4. Schematic model of the spinel unit cell structure.[34]

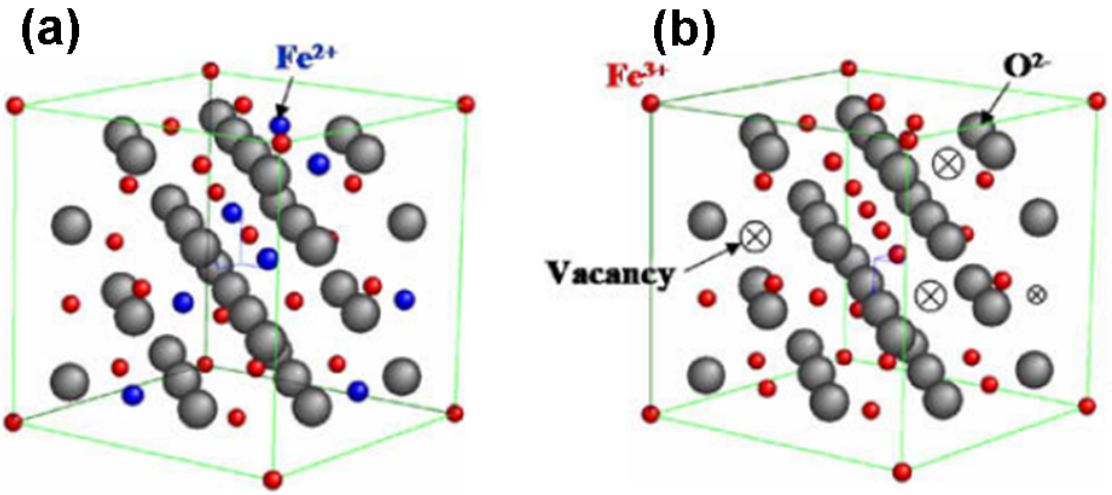

Figure 1.5. The structures of (a) magnetite (Fe_3O_4) and (b) maghemite (γ-Fe_2O_3).[35]

1.2.2 Preparation of Magnetic CNTs (m-CNTs)

Iron oxide nanoparticles, such as magnetite (Fe_3O_4) and maghemite (γ-Fe_2O_3) discussed in previous section, have been of technological and scientific interest due to their unique electric and magnetic properties. These nanoparticles can be used in such diverse fields as high-density information storage and electronic devices.[36-38] Correa-Duarte et al.[39] coated CNTs with iron oxide nanoparticles (magnetite/maghemite) via a layer by layer (LBL) assembly technique and aligned CNT chains in relatively small external magnetic fields as shown in Figure 1.6. Subsequently, the resulting magnetic CNT structures could be used as building blocks for the fabrication of nanocomposite materials.

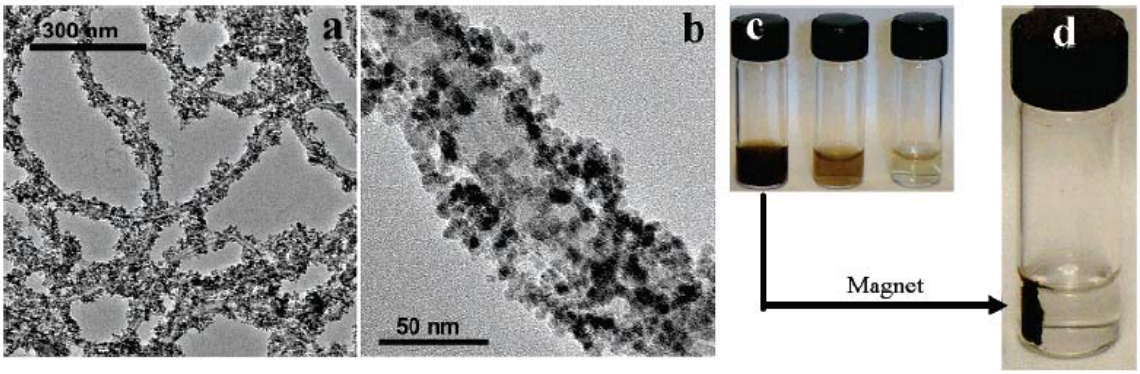

Figure 1.6. TEM images at lower (a) and higher (b) magnifications of iron oxide-coated CNTs and photographs of dispersions in aqueous solution with different concentrations (c) and manipulated by an external magnetic field (d).[39]

Cai et al.[40] decorated CNTs with magnetite nanoparticles in liquid polyols. As a result, these nanoparticles could have significant potential for application in the fields of sensors. In addition, Gao et al.[41] initiated the self-assembly of magnetite particles along MWNTs via a hydrothermal process. The resulting materials feature nanoparticle beads

along the CNT surface, rendering this as an appropriate material to be used as a functional device.

Maghemite, γ-Fe_2O_3, is the allotropic form of magnetite, Fe_3O_4. As discuseed in previous section, these two iron oxides are crystallographically isomorphous. Even though γ-Fe_2O_3 is more stable, since the iron cannot be further oxidized under ambient conditions, maghemite-CNT nanocomposites have not been studied as extensively as magnetite-CNT nanocomposites, with the exception of several examples. Liu et al.[42] decorated MWNTs with maghemite via the pyrolysis of ferrocene at different temperatures. This product is expected to provide an efficient way for the large-scale fabrication of magnetic CNT composites. Youn et al.[43] decorated SWNTs with iron oxide nanoparticles along the nanotube via a magneto-evaporation method. The nanotubes were aligned vertically on ITO surfaces, suggesting the possibility of rendering this process adequate and cost-effective for the mass production. The method described in this work consisted of the use of an iron-oleate complex, oleic acid, and truncated SWNTs to create iron oxide nanoparticles. The research also demonstrated the anisotropic properties of vertically aligned SWNTs in a nanocmoposite by comparing current densities of the aligned and non-aligned CNTs.

Keeping pace with these researches' streaming, for the synthesis of magnetic carbon nanotube hybrid structures, Chaper 2 will describe and report a convenient approach for the decoration of MWNTs with near-monodisperse maghemite nanoparticles by employing a simple modified sol-gel process (*in situ* process) with an iron salt as precursor, followed by calcination in order to create a sound basis for potential future applications. The resulting nanomaterials are superparamagnetic at room

temperature, and hence, are conducive to facile alignment under relatively low magnetic field. This general approach could greatly facilitate the formation of highly anisotropic materials that would benefit from the enhancement of properties mediated by CNT alignment in various matrices.

1.3 Polymer-CNT Nanocomposites

Filler-containing polymer-based composites, affording the development of lightweight strong structures and materials with enhanced electrical and thermal properties, have been widely investigated in recent years. In this context, nanoscale fillers have been considered particularly interesting, since these have a considerable ability to induce important changes in various properties even at low concentrations. For example, carbon black, silicas, clays, and carbon nanofibers have been utilized in order to improve mechanical, electrical, and thermal properties of polymers.[44]

More recently, carbon nanotubes (CNTs)[1] have been extensively examined in the role of nanofillers due to the superior properties that they can impart when adequately dispersed in polymeric matrices.[45-51] Thus, many attempts to make use of CNT's properties in composites have focused on mechanical reinforcement, and the enhancement of electrical and thermal conductivities of polymers. These composite systems have numerous applications.[9, 52] Furthermore, the interface between CNTs and polymer matrices is a significant parameter for the final nanocomposite properties.[53]

The alignment of carbon nanotubes in polymer matrices is also of great importance when attempting to determine the properties of carbon nanotube composites. Hence, the following two sub-sections will address the studies on both the dispersion and

alignment of the carbon nanotubes within the polymer matrix and the properties of semi-crystalline polymer-CNT nanocomposites.

1.3.1 Alignment Strategies of CNTs in Polymer Matrices

Alignments of CNTs by electric, shear induced field, and magnetic field were reported previously by several groups.[54, 55] Bauhofer group[56] successfully demonstrated the application of AC electric fields allowing both the alignment of carbon nanofibers in epoxy resin and their connection into a network. Zhu group[57] studied electric field aligned MWNT/epoxy nanocomposites with a sample size of up to several centimetres using fast UV polymerization, showing significant anisotropic properties for storage modulus and electrical conductivity.

For the characterization of aligned composite systems using shear induced field, Camponeschi et al.[58] probed the effects of shear flow on the alignment of dispersed SWNTs in polymer solutions. The sample solutions were placed in the 8.5 mm gap between the outer cylinder and the spindle. In turn, the spindle was allowed to rotate for one week at several different angular velocities ranging from 12 to 100 rpm. TEM samples were taken in situ from the solutions flowing in circular motion in the gap between the outer cylinder and inner cylinder. In this experimental set up, for systems in which effective dispersion of the carbon nanotubes was achieved by the combined action of both sodium dodecylbenzenesulfonate (NaDDBS) and Carboxymethylcellulose (CMC) as surfactants. The only system in which tube alignment was observed was for the NaDDBS/CMC/SWNT solution that was subjected to shear stresses at the highest angular velocity (i.e. 100 rpm) used in the experiments.

A high magnetic field is another efficient and direct way to align carbon nanotubes. Tanimoto group have found that a high magnetic field of 7 T aligns arc-grown MWNTs.[59] They dried MWNT dispersion in methanol under a constant magnetic field and observed the MWNTs alignment parallel to the magnetic field. This result was explained by the difference between the diamagnetic susceptibilities parallel ($\chi_{//}$) and perpendicular ($\chi_{\perp}$) to the tube axis; if $|\chi_{\perp}|$ is larger than $|\chi_{//}|$, a MWNT tends to align parallel to the magnetic field by overcoming thermal energy.[59] More recently, Steinert and Dean obtained solution cast PET-carbon nanotube composite films by applying a magnetic field, resulting in increased conductivity with the increase of the applied magnetic field.[60] Furthermore, Camponeschi et al.[61] prepared magnetically aligned carbon nanotube composite systems; thus, carbon nanotubes were aligned parallel to the direction of magnetic field, resulting in enhanced mechanical properties. However, due to the low magnetic susceptibility of carbon nanotubes, their alignment by the application of an external magnetic field requires a relatively high magnetic field. This draw-back could be solved by enhancing the magnetic susceptibility of carbon nanotubes by tethering magnetic nanoparticles on their surface.

1.3.2 Semi-crystalline Polymer/CNTs Nanocomposites

Semicrystalline polymer matrices filled with CNTs have been extensively studied, particularly given the fact that CNTs have the potential to nucleate the polymer crystallization.[16, 62-64] One example of semicrystalline polymers is the biodegradable and biocompatible polyethylene oxide (PEO) that has drawn extensive attention because of its potential use in drug delivery, tissue engineering, packing materials, etc.[65-67] Goh et al.

studied the fullerene-capped-PEO(FPEOF)/acid-treated CNTs nanocomposites, and reported that the incorporation of the CNTs into the polymer matrix has no significant effect on the crystallization behavior of FPEOF.[68] Chatterjee et al. studied the dispersion of CNTs in PEO assisted by the presence of surfactants, and reported the reduction in both melting temperature and crystallinity of the resulting nanocomposite with the increase in CNTs content.[69] Furthermore, Jin et al. found reductions in nucleation density, crystallinity, and crystallization rate of PEO embedded with chemically modified CNTs nanocomposites.[70] These nanocomposite systems could be classified as exhibiting anti-nucleation effects of CNTs. Conversely, other cases have shown different results. For example, Shieh et al. studied on PEO/CNT-g-PMMA composites. They found that the PMMA grafted onto CNTs serves as a nucleating agent for the crystallization of PEO, resulting in higher crystallization rate than that of unmodified CNTs.[71] Priftis et al. prepared CNTs grafted with PEO, which also showed higher crystallization rate for the CNTs-g-PEO. The strong impact on the nucleation and crystallization kinetics was attributed to the covalent CNT-PEO bonding.[72]

For the polymer nanocomposite system in this study, hybrid materials, i.e. MWNT/γ-Fe_2O_3, is introduced into a PEO polymer matrix, and as-prepared nanocomposite solution is applied to an external magnetic field (below 0.3 T) in order to generate anisotropic features. The effective alignment of CNTs tethered with magnetic nanoparticles required only a weak magnetic field as compared with other methods in which alignment is obtained only by exposure to high magnetic fields.[61, 73] Thus, Chapter 4 will address a method of fabricating electrically conductive and flexible PEO/magnetic carbon nanotube (m-CNT) composite films that were placed under a weak magnetic field.

1.4 Graphene Nanosheets (GNs)

Following the astonishing discoveries of fullerene and CNT, the emergence of graphene nanosheet (GN) has recently opened up an exciting new field in the science and technology of two-dimensional nanomaterials.[74] It possesses single or a few layers of sp^2 hybridized carbon atoms arragned in six-membered rings. In addition, it is the parent of all graphitic forms including fullerene, carbon nanotubes, and graphite as shown in Figure 1.7.[75, 76]

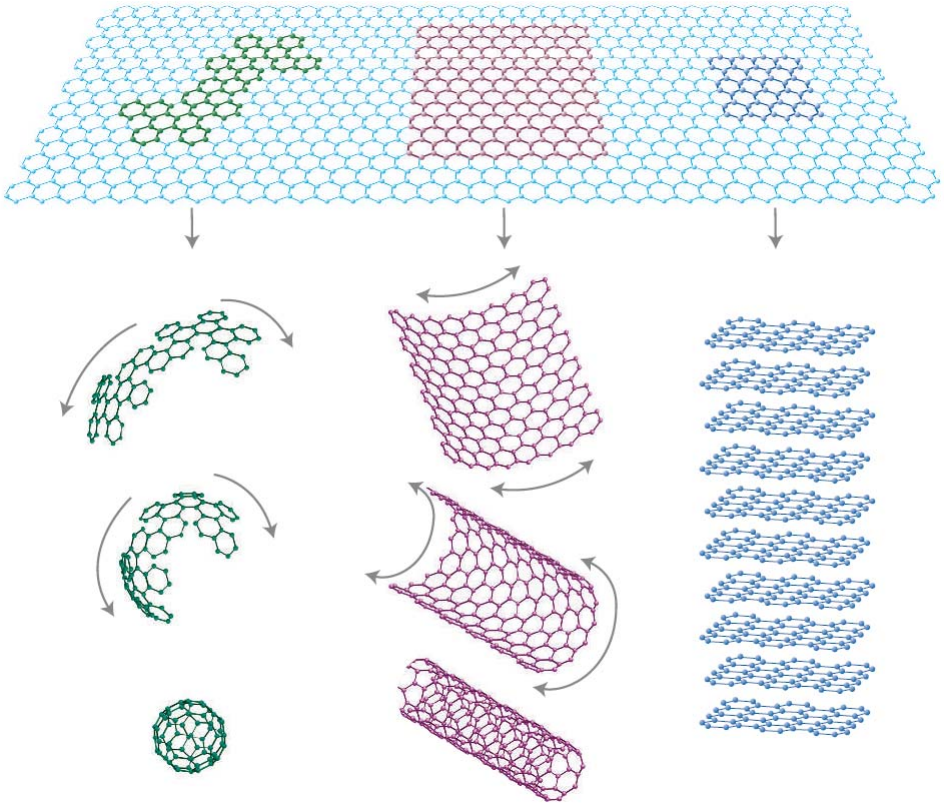

Figure 1.7. Graphene, the parent of all graphitic forms, is a two-dimensional building material for carbon materials of all other dimensionalities. It can be wrapped up into fullerene, rolled up into nanotube, and stacked into graphite.[75, 76]

Although GN is expected to be perfectly flat, ripples occur due to the thermal fluctuations.[74, 75] GN is stable as well as exhibits remarkable optical, electronic, thermal, and mechanical properties, including high values of the Young's modulus of ~1100 GPa,[77] fracture strength of ~125 GPa,[77] thermal conductivity of ~5000 W m^{-1} K^{-1},[78] mobility of charge carriers of 200,000 cm^2 V^{-1} s^{-1},[79] theoretical specific surface area of 2,630 m^2 g^{-1},[75] excellent chemical stability, high optical transmittance, and so on. Significantly, these attractive properties generate enormous interest from different scientific communities such fields as biomedicine, reinforced composites, catalysis, sensors, energy conversion and storage, and electronics for displays and solar cells.

1.4.1 Synthesis of Graphene

1.4.1.1 Chemical Vapor Deposition (CVD) for Graphene

The CVD processes utilize transition metal surfaces for the growth of GN by using hydrocarbon gases as GN presursors at the deposition temperature of ~1000 ^oC. Ruoff et al. reported a CVD method for large area synthesis of high quality and uniform GN films on Cu foils by using a mixture of methane and hydrogen as precursors.[80] The as-obtained films are predominantly single-layer GN as shown in Figure 1.8. The modification of the CVD process, which generally leads to less strict conditions, has been also utilized to produce high quality GN films; for example, achievements from the groups of Dervishi et al.[81] using radio frequency (RF) catalytic CVD route, Kong et al.[82] utilizing ambient pressure CVD on polycrystalline Ni films, and Duesberg et al.[83] applying a low-temperature CVD process. These modified approaches have exhibited the

results such as the prevention of the formation of amorphous carbon or other types of unwanted products and the obtainment of high-quality large-area GN films.

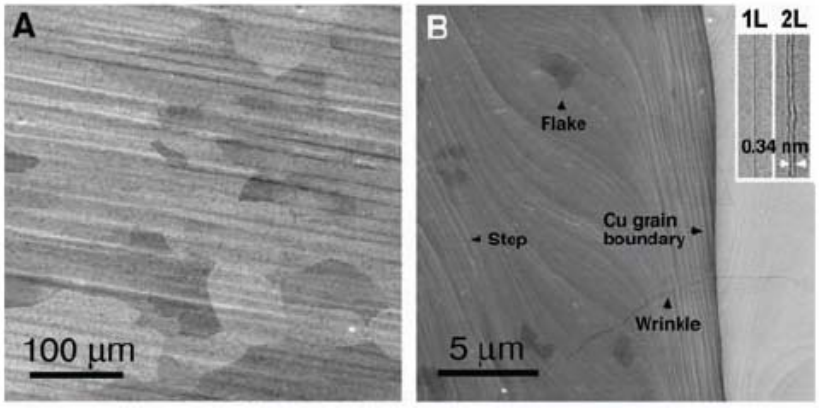

Figure 1.8. (a) SEM image of GN on a cupper foil (growth time: 30 min). (b) HRSEM image representing a cupper grain boundary and steps, two- and three-layer GNs, and graphene wrinkles. Inset shows TEM images of folded graphene edges of one layer (1L) and two layers (2L), respectively.[80]

1.4.1.2 Epitaxial Growth of Graphene on Silicon Carbide

Epitaxial growth on silicon carbide (SiC) is a very promising method for the synthesis of uniform and wafer-size GN layers, where single crystal SiC substrates are heated in vacuum to high temperatures in the range of 1200-1600 ^{o}C. Thus, these research have been conducted in several groups, Shivaraman et al.,[84] Aristov's group,[85] and Seyller et al..[86] However, these strict conditions for GN such as high temperature, ultrahigh vacuum, inert atmosphere, and single crystal substrate in most cases can limit the use of this technique in large scale practical applications.

1.4.1.3 Substrate Free Gas-Phase Synthesis of Graphene

The substrate free gas-phase strategy has become a successful method for the synthesis of high quality GN.[87, 88] This is able to continue GN production at ambient conditions, which include sending an aerosol consisting of liquid ethanol droplets and argon gas directly into atmospheric pressure microwave-generated argon plasma. Dato et al. reported a novel technique to synthesize GN in the gas phase using a substrate free, atmospheric pressure microwave plasma reactor as shown in Figure 1.9.[87] The obtained GN was found to show easy dispersion in methanol by using sonication, resulting in the formation of a homogeneous black suspension. However, its as-prepared GNs' layer number was hard to control and few-layer GN was usually contained in the product, which could affect the properties of electronics.

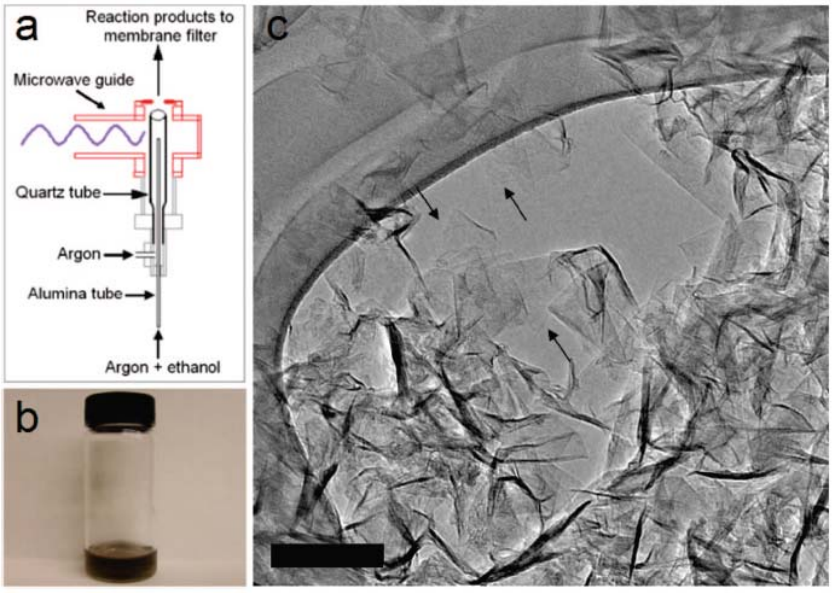

Figure 1.9. (a) Schematic illustration of the atmospheric pressure microwave plasma reactor. (b) A photograph of GNs dispersed in methanol. (c) TEM image of GNs; the arrow bars show homogeneous and featureless regions. (Scale bar: 100 nm).[87]

1.4.1.4 Reduction of Graphene Oxide

Extensive reviews for the preparation of dispersions of graphene oxide platelets and reduced graphene oxide (rGO) platelets made from graphite oxide have been recently appeared.[79, 89] Generally, graphite oxide is synthesized by the Brodie,[90] Staudenmaier,[91] Hummers method,[92] or some modification of these methods. All three methods involve oxidation of graphite to a variety of levels. For example, Brodie and Staudenmaier used a combination of potassium chlorate ($KClO_3$) with nitric acid (HNO_3) in order to oxidize graphite. The Hummers method involves the treatment of graphite with potassium permanganate ($KMnO_4$) and sulfuric acid (H_2SO_4).

Figure 1.10 represents a proposed structure of graphene oxide that is supported by solid-state nuclear magnetic resonance (SSNMR) experiments on ^{13}C-labeled graphite oxide.[93, 94] The polar oxygen functional groups of graphite oxide render it hydrophilic; thus, graphite oxide is able to be exfoliated in many solvents as well as dispersed particularly well in water.[95]

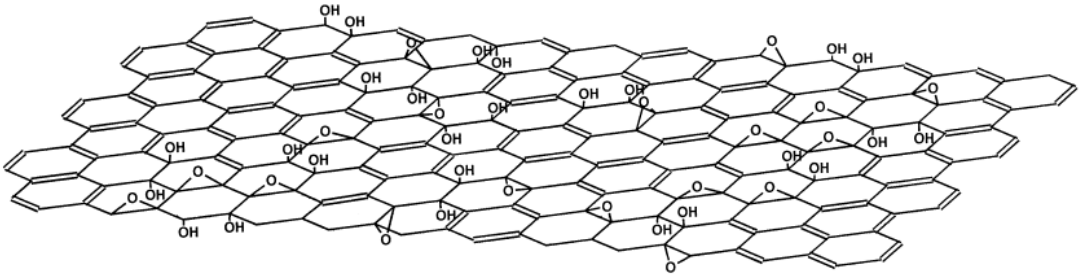

Figure 1.10. A proposed schematic representation of graphene oxide structure.[94]

Oxidative exfoliation of natural graphite by thermal or oxidation method and subsequent reduction has been evaluated as one of the most efficient technique for low

cost, large scale production of GN. In this method, the abundant oxidization of graphite produces graphene oxide, which has disrupted conjugation in the plane, missing carbon atoms in the plane, and heavy functional groups weaken the van der Waals interactions between the layers of graphene oxide and make them hydrophilic.[75, 96] However, due to their strong hydrophobicity, GN obtained from the reduction of graphene oxide generally suffers from limited solubility or even irreversible agglomeration. Thus, it makes further processing and application difficult. Li et al. reported that reduced GN could be prepared by maintaining a high pH value during chemical reduction without the need for polymeric or surfactant stabilizers.[97]

Amphiphilic functional molecules such as DNA, conjugated-polyelectrolyte, lignin and cellulose derivatives, ionic liquid, nonionic polymeric surfactants, and cyclodextrin have been shown to act as agents to enhance the solubility of GN.[98-107] This is because the hydrophobic part of amphiphilic functional molecules could form a strong π-π interaction with the chemically reduced GN whereas the hydrophilic side chains on the surface of GN prevented the GN aggregation via the electrostatic and steric repulsions.

In the chemical reduction techniques, toxic substances such as hydrazine and $NaBH_4$ were usually used to reduce graphene oxide. Thus, it is desirable to explore a non-toxic and stable agent for the reduction of graphene oxide. Guo et al.[108] and Zhang's group[109] have used ascorbic aced and sugars as reducing agents for the green chemistry route.

Novel dehydration or deoxygenation process has also exhibited effective route to obtain GN with high stability. Those stable GN suspensions could be prepared by simply

heating a graphene oxide suspension under strongly alkaline conditions at moderate temperatures (50-90 ^{o}C) as shown in Figure 1.11.[110]

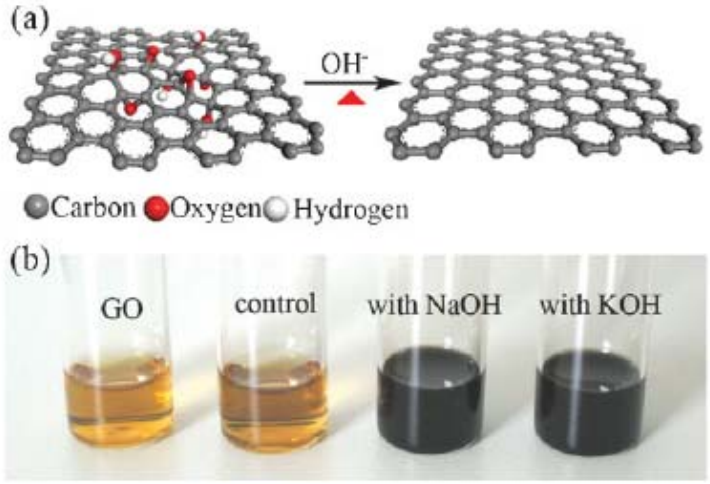

Figure 1.11. (a) The illustration of the deoxygenation of exfoliated graphene oxide under alkaline conditions. (b) The images of the exfoliated graphene oxide suspension before and after reaction. The control experiment was carried out by heating the graphene oxide suspension without NaOH and KOH at 90 ^{o}C for 5 h with the aid of sonication.[110]

To disperse GN in organic solvents is another effective method because some important applications need to be conducted in organic systems such as catalytic reactions, and for the design of GN-polymer nanocomposites. Interesting functional molecules such as ethylenediamine (EDA) and end-functional polymers have been employed for promoting the dispersibility of GN in organic solvent.[111, 112] Mentioned above and not-mentioned techniques for the preparation of GN are summarized in Table 1.2.

Table 1.2. Comparisons on different synthesis methods for graphene nanosheet.

Preperation methods	Precursor	cost	Electronic quality	# of layers	Size of layers	Throughput	Ref.
Mechanical exfoliation	Graphite	Low	High	Single & multiple	10 μm	Low	74
Chemical vapor deposition	Hydrocarb -ons, hexane, acetylene	High	High	Single & multiple	> 100 μm	Low	80-83
Epitaxial growth of graphene on SiC	SiC wafer	High	High	Single & multiple	> 50 μm	Low	84-86
Substrate free gas phase synthesis	Ethanol	Low	High	Single & multiple	Hundreds of nm to several μm	High	87, 88
Chemical reduction of graphene oxide	Graphite	Low	Low	Single & multiple	Tens of nm-100 μm	High	97-112

1.5 Graphene-Based Hybrids

Appropriate combination of different nanoscale materials with different morphologies, shape, or components may lead to the development of multifunctional nano-assembled systems that exhibit simultaneously novel electronic, optical, magnetic, and mechanical properties with enhanced performance. Particularly, the synthesis and design of multi-component hybrid nanostructures including at least one GN component is topical due to both the particular properties of GN and synergistic properties induced by different functional nanoscale objects.

Therefore, this section will address recent achievements on how to develop both effective strategies for synthesizing high-quality graphene/oxide hybrids and graphene-based electrode materials for energy storage applications; specifically, the graphene-iron oxide hybrid composite as an anode material for lithium ion battery.

1.5.1 Graphene/Oxide Hybrids

In the past decades, oxide nanomaterials have received considerable attention due to their promising optical, electronic, magnetic properties, and significant applications in the field of biomedicine, optoelectronics, energy and sensors, and so on.

The development of graphene/oxide composites provides an important milestone in order to improve the application performances of oxide materials in such various fields as energy harvesting, conversion and storage device, nanoelectronics, and nano-optics and conductors, because the hybrid structures could exhibit versatile properties with performances superior to those of the individual oxide nanomaterials.

In order to construct high-quality graphene/oxide hybrids, important points should be addressed:

(a) GN should have high solubility in the solution throughout the experiments, which is important to keep individual graphene sheets to maximize its performance in the hybrids.

(b) The surface of graphene nanosheets should contain some oxygen-containing groups to promote the effective linkage between GN and oxide.

(c) The morphology of the oxide should be controlled to the desirable structure for optimizing its properties.

Driven by these significant key points, many groups have developed novel routes for developing graphene/oxide hybrids including oxide components such as SiO_2,[113, 114] Fe_2O_3,[115] Fe_3O_4,[116, 117] TiO_2,[118-121] SnO_2,[122-124] ZnO,[125, 126] Al_2O_3,[127] Co_3O_4,[128] $Co(OH)_2$,[129] and MnO_2.[130] For example, Park et al.[125] illustrated that ZnO nanorod-GN

hybrid architectures composed of regular arrays of ZnO nanorods could be readily obtained through a ZnO seed mediated growth process, and transferred to transparent and flexible substrates. Yu's group[116] demonstrated a simple in situ method to efficiently decorate GNs with magnetite nanoparticles through high-temperature decomposition of an $Fe(acac)_3$ precursor in polyol, which could be utilized as an enhanced magnetic resonance contrast agent. Kamat et al.[119] succeeded in carrying out UV induced photocatalytic reduction of graphene oxide as well as obtaining well separated GN-TiO_2 composite sheets. Mullen et al.[114] reported a bottom up approach to the large scale production of two-dimensional sandwich-like high-quality graphene/mesoporous silica hybrid structures, where each GN is fully separated by a mesoporous silica shell as shown in Figure 1.12 (a) and (b). In addition, Dong's group[121] developed a novel and facile process of water-phase synthesis for high-quality graphene/TiO_2 composite hybrid structures using $TiCl_3$ as both a reducing agent and a precursor as illustrated in Figure 1.12 (c) and (d).

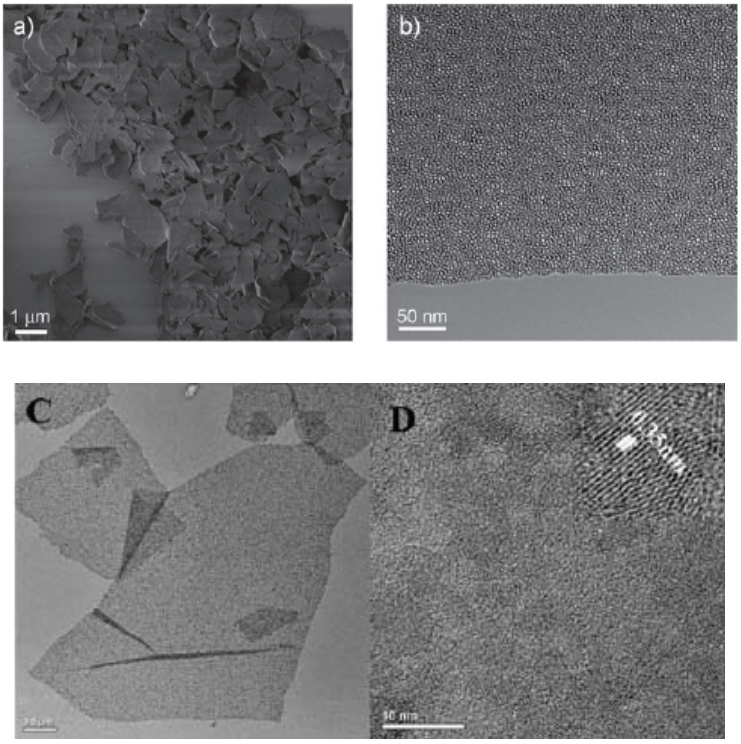

Figure 1.12. Graphene-based mesoporous silica nanosheets after pyrolysis at 800 ^{o}C. (a) SEM and (b) TEM images reveal stable morphology and mesoporous structure of graphene-silica sheets after pyrolysis at high temperature.[114] (c) TEM and (d) HRTEM images of grphene-TiO_2 composite nanosheets.[121]

1.5.2 Graphene-Based Lithium Ion Battery Applications

Developing efficient and clean energy technologies is, at present, a significant task and is crucial to the long-term energy and environmental security of the world. The novel physical and chemical properties of nanostructured materials promise a number of advanced applications in the development of new energy and chemical conversion technologies.[131] In this sense, graphene nanosheets play an important role on maximizing the activity of supported nanomaterials with different size, shapes, and chemical compositions due to high surface area, excellent conductivity, good stability, high electron mobility, excellent optical transparency, and good mechanical performance as

discussed in previous section. These characteristics are very important for the purpose of enhancing the activity, stability, and durability for energy applications.

1.5.2.1 Graphene/Iron Oxide Composites as Anode Materials for Lithium Ion Batteries

Lithium ion batteries (LIBs) have been widely used as power sources for portable electronic devices and attracted a variety of attention due to their high energy density and power density.[132] Anode and cathode materials play important roles in the performance of LIBs. Based on these conceptual approaches, extensive studies have been performed with diverse materials ranging from Si-based anodes with high gravimetric capacity[133-136] to various transition metal oxides offering high volumetric and moderately high gravimetric capacities,[137-147] which is beyond that of commercial graphite anodes (340-365 mAh/g, 500-650 mAh/cm^3). The performance of transition metal oxide anodes has commonly been limited due to the high volume changes during continuous charge-discharge process, resulting in breaking down of electrical connection of anode materials from current collectors.

As discussed in previous sections, graphene is a two-dimensional aromatic monolayer of carbon atoms with sp^2 hybridization. Graphene shows an extraordinary and stable in-plane electrical conductivity, excellent thermal conductivity and mechanical property, flexible porous structure, and high specific surface area.[76] Due to these outstanding properties, it has been proposed that graphene could be utilized as energy storage and conversion devices like an anode material for LIBs. As an electrode material, graphene has shown a large reversible specific capacity.[148-151] However, it also has characteristics such as large irreversible capacity losses, low initial columbic efficiency,

and rapid capacity fading. For the purpose of overcoming these limitations and improving electrode capacity and cycling stability, many groups have been recently studying hybrid structures as anode materials for LIBs such as graphene decorated with such as TiO_2,[152] SnO_2,[122] Co_3O_4,[114] Fe_3O_4,[153-155] and Mn_3O_4[156]. These hybrid materials have demonstrated large reversible capacity, long cycle life, and good rate performance resulting from new electrochemical behaviors within a confined two-dimensional nanostructure interspaces. Even though some studies on hematite (α-Fe_2O_3) were conducted for improving anode materials,[157] researches on another existing abundant form of the iron oxide in nature, maghemite (γ-Fe_2O_3), have never been reported.

Therefore, Chapter 5 will address a facile synthesis of reduced graphene oxide/γ-Fe_2O_3 hybrid structures by applying developed synthesis method, modified sol-gel process (*in situ* process) with an iron salt as a precursor, followed by calcination. The transformation of graphene oxide into graphene is accomplished by thermal activation and no reducing agent is used. The maghemite nanoparticles are homogeneously tethered on the reduced graphene oxide (rGO) sheets, which allow them to maintain electrical connenctivity during large volume changes and assist in avoiding agglomeration during continuous charge-discharge process. Moreover, the tethered maghemite nanoparticles greatly assist in keeping adjacent graphene sheets separated and avoiding re-stacking of graphene sheets into graphite. Furthermore, it is reported that poly(acrylic acid) (PAA) can be utilized as an efficient binder for Si anode.[136] Thus, for this study, PAA is used an effective binder in rGO/γ-Fe_2O_3 composites as well. PAA is soluble in water as well as in a variety of ecologically friendly organic solvents such as ethanol. PAA can interact with copper surface via hydrogen bonding (with Cu oxide) and/or Cu salt formation;

namely, PAA has good adhesion strength between the electrode and the current collector foil for the integrity of the anode. In addition, as-prepared PAA films showed negligible swellability in the carbonate vapors (DEC vapor), resulting in a low level interaction of PAA/electrolyte and retention of mechanical properties, contrary to those of PVDF. The rGO/γ-Fe_2O_3/PAA composite anode shows excellent cycling performance and rate capability even at high current rate of 10 C. Therefore, functionalizing graphene sheets with iron oxide nanoparticles and using an effective binder, PAA, may promise as a future electrode system for superior performance, such as high energy density and power density, for lithium ion batteries.

1.6 Objectives of Thesis

The objectives of the study are as follows:

- To study on the hybrid nanostructures of carbon nanotubes tethered with iron oxide magnetic nanoparticles, γ-Fe_2O_3, by applying a novel synthesis method, modified sol-gel technique (*in situ* process).
- To study on the alignment of as-prepared magnetic carbon nanotubes (m-CNTs) in various polymer matrices even under a low magnetic field strength ($\leq$ 0.3 T).
- To study on the anisotropic physical properties of polymer/m-CNTs composites induced by the aligned features of m-CNTs in polymer matrices.
- To study on the development of graphene/iron oxide hybrid nanostructures, and the electrochemical performance of as-prepared composites as anode materials for Li-ion batteries (LIBs).

CHAPTER 2

MAGNEMTIC CARBON NANOTUBES TETHERED WITH MAGHEMITE MAGNETIC NANOPARTICLES: SYNTHESIS AND CHARACTERISTICS

2.1 Introduction

This Chapter describes and reports a convenient approach for the decoration of MWNTs with near-monodisperse maghemite nanoparticles by employing a simple, modified sol-gel process (*in situ* process) with an iron salt as precursor, followed by calcination, and focus on the detailed characterization of the product, i.e. the resulting nanocomposite materials, in order to create a sound basis for potential future applications. Sites where nanoparticles attach and their controlled particle size on the surface of the MWNTs are determined not only by different calcination temperatures, but also by the mass ratio of iron salt to MWNTs. The resulting nanomaterials are superparamagnetic at room temperature, and hence, are conducive to facile alignment under relatively low magnetic field. This general approach could greatly facilitate the formation of highly anisotropic materials that would benefit from the enhancement of properties mediated by CNT alignment in various matrices.

2.2 Experimental

2.2.1 Materials

This experiment was performed with MWNT (>99%) produced by chemical vapor deposition followed by HCl mineralization. The diameter of the MWNTs is estimated at 12 nm and the length around 10 μm. For the formation of a surface

carboxylate group along the MWNTs, concentrated sulfuric acid (98%) and concentrated nitric acid (70%) were purchased from Fisher Scientific. And for the preparation of magnetic carbon nanotubes, ferric nitrate nonahydrate, $Fe(NO_3)_3 \cdot 9H_2O$ was purchased from Acros Organics. Propylene oxide (>99%), C_3H_6O (1,2 epoxide), and absolute ethanol (anhydrous, 200-proof) were purchased from Aldrich and used as received. Sodium dodecylbenzene sulfonate (NaDDBS, from TCI) was used in the same concentrations and methods as described in the work of Matarredona et al.[158]

2.2.2 Carboxylation

The MWNTs were first dispersed in a solution of concentrated sulfuric acid and concentrated nitric acid (a 3:1 volume ratio). The samples were sonicated in a typical ultrasound bath for 3 h. This acid mixture containing MWNTs was diluted to 25% of its original concentration. Then, the oxidized MWNTs were filtered with a PTFE filter membrane (Alltech, 0.45 μm pore size) with the aid of vacuum pump. The MWNTs were washed several times vigorously during filtration in order to reach neutral pH. Then MWNTs were dried in the vacuum oven at 50 ^oC overnight.

2.2.3 Synthesis of Maghemite-MWNT Nanostructure

This work was done by a modified sol-gel process. For the synthesis with $Fe(NO_3)_3 \cdot 9H_2O$, 0.65 g $Fe(NO_3)_3 \cdot 9H_2O$ was added to 20 ml of absolute ethanol (100% purity) and stirred until $Fe(NO_3)_3 \cdot 9H_2O$ was dissolved completely. This solution was added by oxidized MWNTs, stirred, and sonicated for 3 h. 20 ml of 1.2 mM NaDDBS was added to the solution, stirred; and then 1.2 ml of propylene oxide was added as a gelation agent and stirred. The mixture was then placed in a Fisher Scientific iso-temperature oven for drying for 72 h at 100 ^oC. The resulting powder products were

washed with water and ethanol several times and dried at 50 ^{o}C. The calcinations of these powders were performed at different temperatures in a furnace under nitrogen atmosphere.

2.2.4 Characterization

The dried samples were ground into a fine powder using a ceramic mortar and pestle. Tiny amounts of samples were rarified with KBr powder, ground, and pressed in a KBr pellet with a punch and die. A Nicolet Nexus 870 spectrometer scanned the range from 4000 to 400 cm^{-1} with a resolution of 2 cm^{-1} and data spacing of 0.964 cm^{-1}. XPS scans of powder samples were taken using a Surface Science Laboratories SSX-100 ESCA spectrometer using monochromatic Al Kα radiation (1486.6 eV). XRD measurement was performed with a X'pert Pro Alpha-1 (wavelength of 1.54 Å). XRD peaks were collected from $2\theta = 0^{o}$ to 90^{o} with a step size of 0.02^{o}. Raman spectra were recorded in the range of 200-2000 cm^{-1} at ambient temperature using a WITEC Spectra Pro 2300I spectrometer equipped with an Ar-ion laser, which provided a laser beam of 514 nm wavelength. TEM samples were prepared by placing a droplet of solution onto a TEM grid, and these samples were analyzed using the Hitachi HF2000, 200 kV transmission electron microscope. The alignment of sample was conducted by magnet (GMW-5403) at 0.3 T, and aligned features of samples were characterized using SEM (LEO 1530). The samples for SEM were prepared by dispersing as-prepared nanostructures in water solution with surfactant, sonicating for 30 min, and then depositing the samples onto silicon wafer under an external field. The magnetic properties of MWNTs were measured using a 5.5 T Quantum Design Superconducting

Quantum Interference Device (SQUID) magnetometer at the National High Magnetic Field Laboratory (NHMFL) at the Florida State University.

2.3 Results and Discussion

The most significant and novel result of this report is the synthesis of magnetic carbon nanotubes decorated with both well-defined and well-dispersed maghemite nanoparticles and their resulting alignment. The key step for imparting magnetic properties to the carbon nanotubes consists of a carefully designed synthesis method that involves a modified sol-gel process. Other methods to obtain such iron oxide nanoparticles reported to date require high-pressure and hazardous environments such as the generation of hydrogen gas, which can be difficult and costly to produce in bulk.[159, 160] However, the modified sol-gel process presented here constitutes a simple and economical process for the formation of iron oxide nanoparticles tethered to carbon nanotubes.

As a first step, the MWNTs were carboxylated in order to introduce negative charges on their surface, which in turn will interact with Fe (III) ions present in a strong acid solution. This process was also coupled with sonication to ensure dispersion of the MWNTs in the suspension. The x-ray photoelectron spectroscopy (XPS) wide-survey (Figure 2.1(a)) and high resolution spectra (Figure 2.1 (b)) reveal not only the presence of carbon-carbon bonding of MWNTs at 285 eV binding energy but also the formation of a carbonyl moiety consistent with carboxylated groups at 288 eV binding energy.

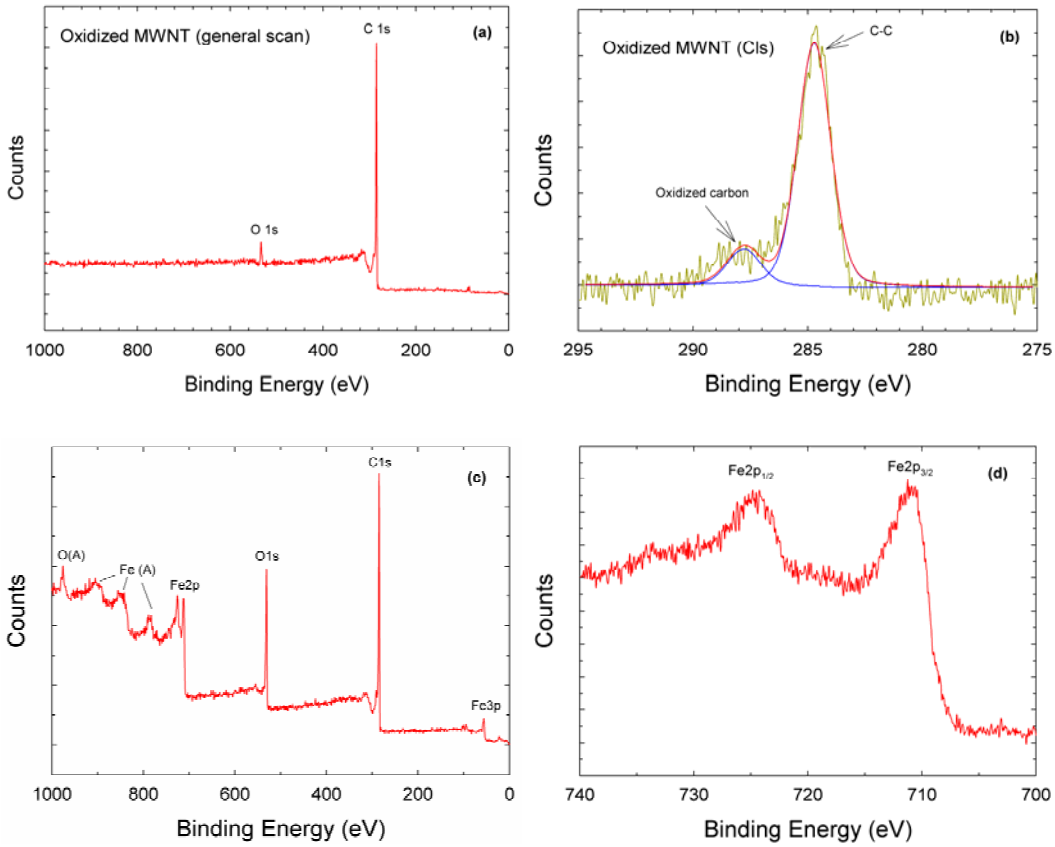

Figure 2.1. (a) The XPS survey spectrum of oxidized and activated MWNT (b) The high resolution XPS spectrum of C1s, which shows oxidized carbon in the form of a carboxylate group at a binding energy of 288 eV. (c) The XPS survey spectrum of MWNT/γ-Fe_2O_3. (d) The high resolution XPS spectrum of Fe 2p bands.

The formation of Fe_2O_3 is dependent upon the presence of propylene oxide, which functions as an oxide promoter. The general mechanism of Fe_2O_3 formation by the addition of an epoxide to a hydrated iron nitrate solution assumes that propylene oxide behaves as a weak base (Figure 2.2) that is known to form iron oxide due to the rapid reaction of the base with the metal ion.[161] Effectively, the propylene oxide acts as a "proton scavenger," since it extracts protons from the water molecules coordinated to the iron salt, resulting in a protonated epoxide. Subsequently, the protonated epoxide undergoes ring-opening by reacting with a nucleophile, such as a nitrate ion or water. As

a result of this ring-opening reaction, deprotonation of the hydrated metal complex occurs, and a diol is formed in conjunction with a net decrease of proton concentration in the solution. After further hydrolysis and condensation of the initial hydrated metal complex, increased heating results in the formation of Fe_2O_3.[162-164]

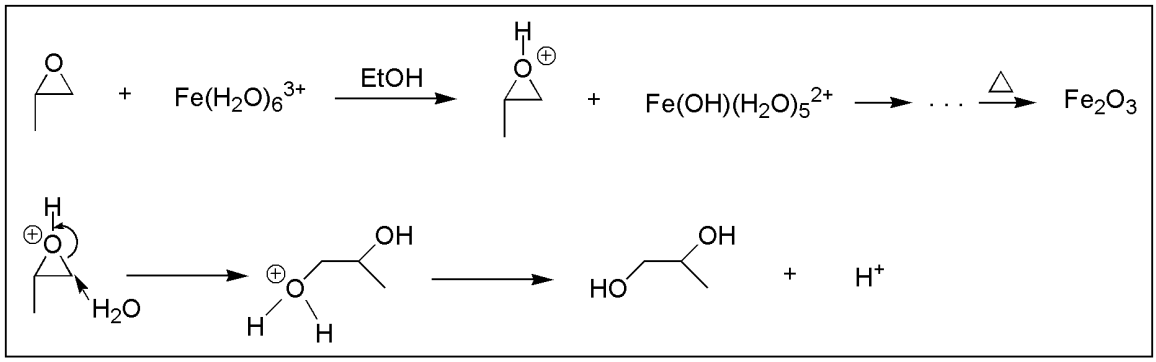

Figure 2.2. The general mechanism of γ-Fe_2O_3 formation by the addition of propylene oxide to a hydrated iron nitrate solution.[162]

The gelation occurs as a result of a drying process when metal oxide particles are in the growth stage. If there is no surfactant, metal oxide particles would eventually grow and coalesce, which could form gels. In our system, the occurrence of gelation was inhibited by the addition of a surface active molecule, NaDDBS, which interferes in the growth stage of the iron oxide nanoparticles (gel phase) and prevents the formation of a gel. This occurs because the NaDDBS molecules would have already coordinated to the iron (III) centers (Figure 2.3) due to the attraction between the negatively-charged hydrophilic head of the surfactant and the positively-charged iron.[165, 166] Hence, while it is appropriate to refer to this method a *modified* sol-gel process, it is important to note that the surfactant inhibits the formation of a gel if introduced into the reaction system at the appropriate stage,[20] i.e. before gelation can occur. In addition to inhibiting gel

formation, the NaDDBS molecules also stabilize the nanoparticles (Figure 2.3). Because the NaDDBS molecules were added before the addition of the propylene oxide and in the presence of excess water, they have formed a self-assembled protective layer around the iron. This coordination has been able to prevent the approach of the propylene oxide molecules within the coordination sphere of the iron centers, which would have resulted in the formation of a gel. Therefore, due to the presence of the NaDDBS molecules, no aggregates of γ-Fe_2O_3 were formed but rather the nanoparticles remained individually isolated.

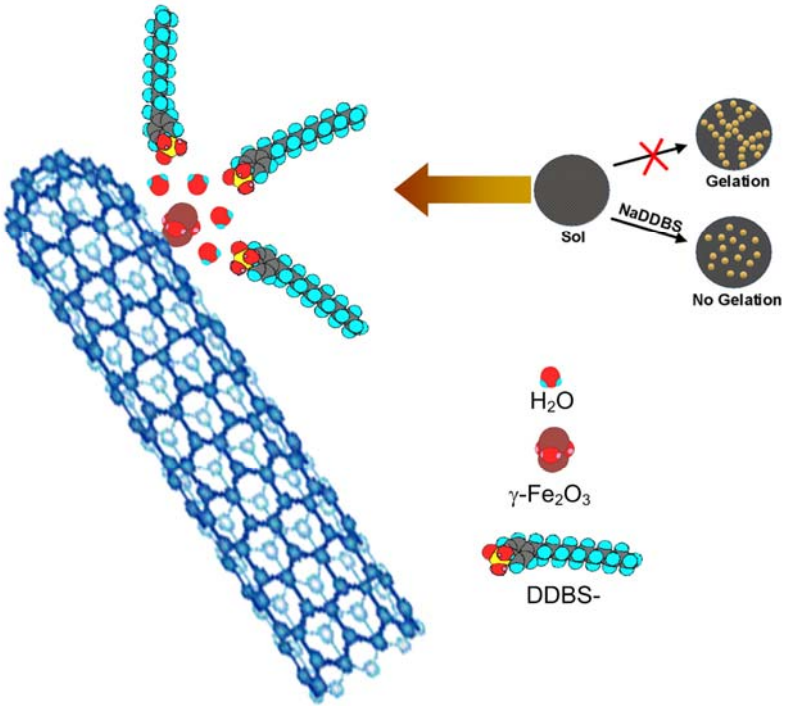

Figure 2.3. Hydration sphere around iron (III) centers coordinated with the NaDDBS surfactant molecules. The presence of NaDDBS molecules may be responsible for the inhibition of the formation of the gel.

The FTIR spectrum of the product of this modified sol-gel process shows the presence of well-crystallized iron oxide nanoparticles after calcination at 600 $^{\circ}$C (Figure

2.4). Maghemite (γ-Fe_2O_3) has an inverse spinel structure and therefore, it can be seen as an iron-deficient form of magnetite. If the powder is not heat-treated, a weak and broad peak from 800 to 400 cm^{-1} is observed (Figure 2.4 (b)). This is the evidence of an amorphous iron oxide phase with minimal long-range order typical of maghemite or magnetite. However, after calcination, IR bands show strong peaks at 576 and 460 cm^{-1}, which correspond to a partial vacancy ordering in the octahedral positions in the maghemite crystal structure (Figure 2.4 (a)).[167-169]

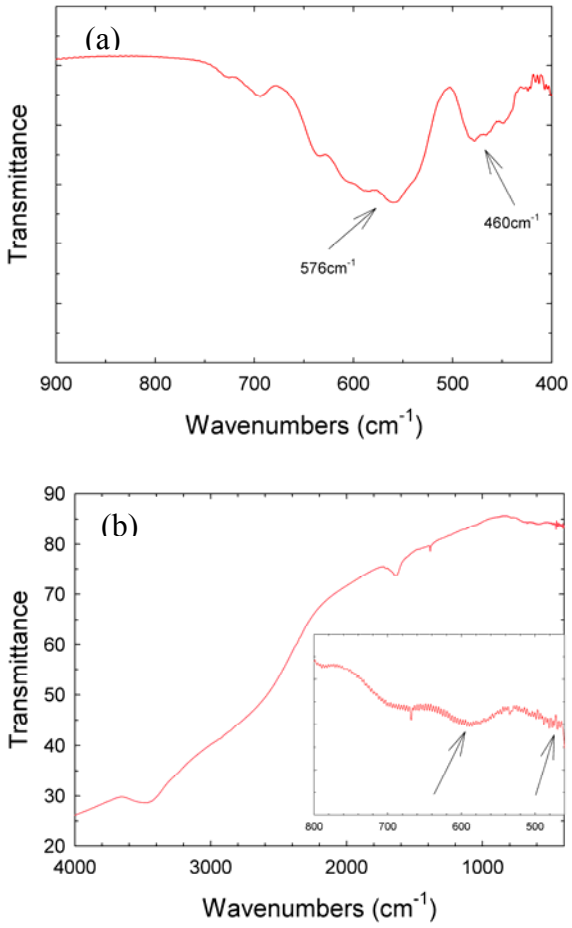

Figure 2.4. FTIR spectrum of MWNT/γ-Fe_2O_3 (a) after calcinations at 600 ^oC and (b) before calcination.

X-ray diffraction patterns of MWNT containing iron oxide nanoparticles calcinated at different temperatures with the initial $Fe(NO_3)_3 \cdot 9H_2O$:MWNTs mass ratio of 4:1 and 2:1 demonstrate the high crystalline nature of the nanoparticles (Figure 2.5). The diffraction peak at $2\theta = 26^{\circ}$ can be confidently indexed as the (002) reflection of the MWNTs, similar to that of pure MWNTs. The other peaks in the range of $20° < 2\theta < 80°$ correspond to the (220), (311), (400), (422), (511), (440), and (533) reflections of maghemite (γ-Fe_2O_3) and/or magnetite (Fe_3O_4). When the mass ratio of $Fe(NO_3)_3 \cdot 9H_2O$ and MWNTs increases from 2:1 to 4:1, the intensity of the carbon (002) reflection decreases. Also, when calcination temperature increases from 500 ^{o}C to 600 ^{o}C, the crystal structure of the product becomes better-defined. Because XRD patterns of maghemite and magnetite are practically identical,[42] x-ray diffraction alone cannot be used to distinguish between the two phases. Therefore, additional experimental techniques were employed to discern between these two phases.

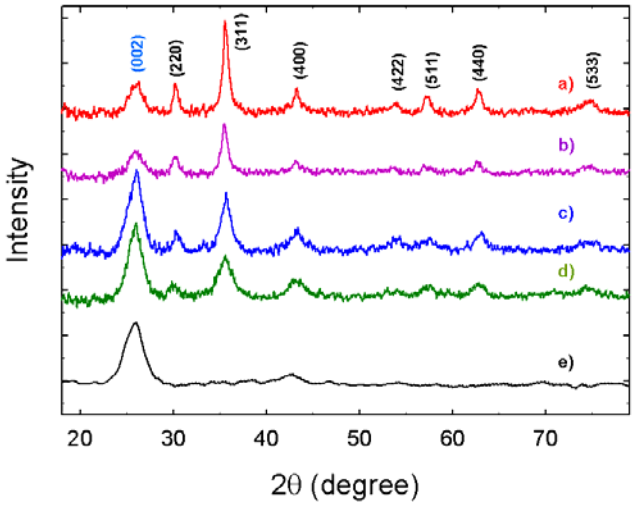

Figure 2.5. The XRD patterns of MWNT/γ-Fe_2O_3 nanostructures fabricated with two different mass ratios of $Fe(NO_3)_3 \cdot 9H_2O$ and MWNTs: (a) 4:1 at 600 ^{o}C; (b) 4:1 at 500 ^{o}C; (c) 2:1 at 600 ^{o}C; (d) 2:1 at 500 ^{o}C; (e) MWNT.

X-ray photoelectron spectroscopy (XPS) as well as Raman spectroscopy confirmed that the iron oxide nanoparticles formed were indeed maghemite and not magnetite. After the formation of oxidized MWNTs decorated with iron oxide nanoparticles followed by calcination at 600 ^{o}C, XPS shows characteristic iron peaks in addition to carbon and oxygen (Figure 2.1(c) and (d)). The position of the Fe (2p3/2) and Fe (2p1/2) peaks were marked at 711.3 and 724.4 eV, respectively, which are in good agreement with the values reported for γ-Fe_2O_3 in the literature.[170, 171] Therefore, this suggests the formation of γ-Fe_2O_3 in our samples.

Raman spectroscopy can also effectively distinguish between maghemite and magnetite nanoparticles. The strong peak at ~1350 cm^{-1} can be assigned to the D band of MWNTs, while another dominant peak at ~1576 cm^{-1} can be ascribed the G band of MWNTs (Figure 2.6(a)).[172] In contrast to magnetite, the maghemite bands are not well-defined, but rather consist of several broad peaks around 350, 500, and 700 cm^{-1} (Figure 2.6(b)),[169] which are unique to these species and are absent in other types of iron oxide nanoparticles. This supports the conclusion that the nanoparticles bound at the walls of the MWNTs are maghemite and not magnetite. When following the same experimental method in the absence of carbon nanotubes, the iron oxide nanoparticles that were formed at 600 ^{o}C consisted of α-Fe_2O_3, as determined by XRD (Appendix A). Clearly, the presence of the carbon nanotubes affected the structure of the maghemite species obtained, supporting the notion that the nucleation and growth of these particles were intimately driven by their attachment to the surface of the MWNT.

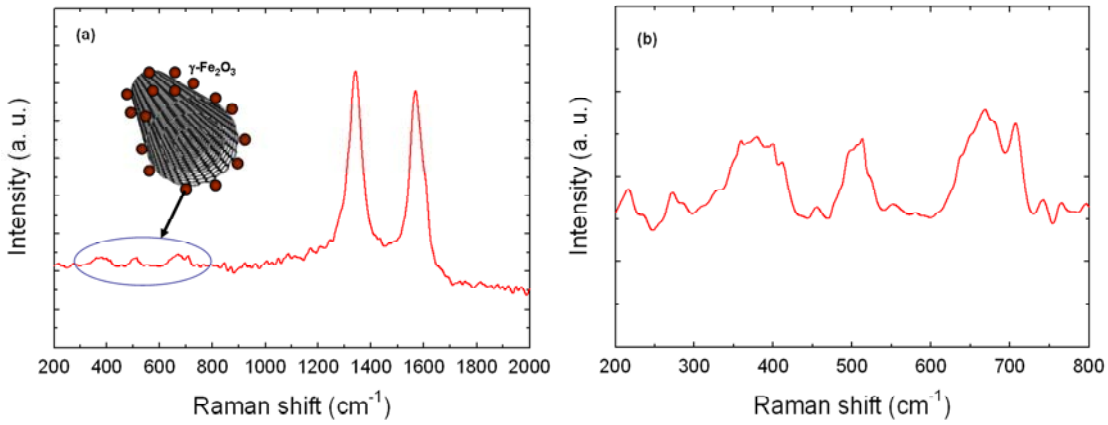

Figure 2.6. (a) The Raman spectrum of MWNT/γ-Fe_2O_3 nanostructure prepared at 600 ^oC with the mass ratio of 4:1 and (b) The detailed Raman spectrum of the same sample in the 200-800 cm^{-1} spectral range.

Transmission electron microscopy (TEM) images of MWNTs/γ-Fe_2O_3 confirmed that γ-Fe_2O_3 was attached to the walls of the MWNTs. At a mass ratio of 4:1 between the $Fe(NO_3)_3 \cdot 9H_2O$ precursor and the MWNTs, the particle size increased with increasing temperature from 500 ^oC to 600 ^oC, and the average sizes were 10.1 nm and 10.8 nm, respectively (Figure 2.7(b) and (c)). Similarly, when the mass ratio of $Fe(NO_3)_3 \cdot 9H_2O$ precursor and MWNT was 2:1, the average particle sizes as a result of the increased temperature were 7.9 nm and 8.4 nm, respectively (Figure 2.7(e) and (f)), which also slightly increased with increasing temperature. This result indicated that both a higher mass ratio between the $Fe(NO_3)_3 \cdot 9H_2O$ precursor and the MWNT and increasing temperature led to larger nanoparticles, and therefore, a conclusion is that particle size could be controlled by the precursor to MWNT mass ratio and temperature. The selected area electron diffraction (SAED) pattern of the sample shows clear diffraction spots (Figure 2.7(a)), which indicate the high crystallinity of maghemite. Chemical analysis using EDS during the TEM analysis showed the presence of Fe, O, and C in the

maghemite-MWNT system (Figure 2.8) and the calculated atomic ratio of Fe and O was close to 2:3, which suggested the formation of γ-Fe_2O_3.

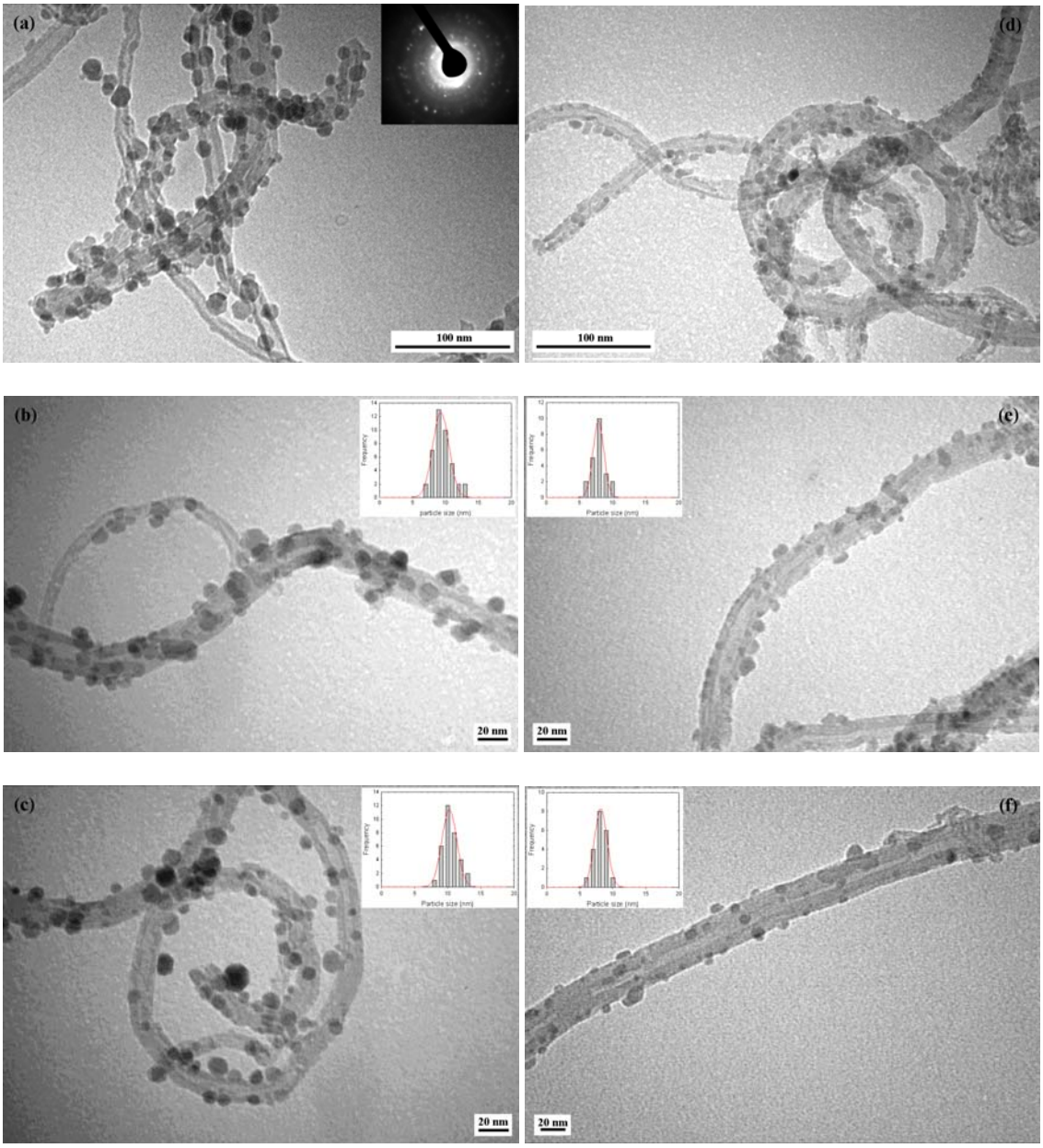

Figure 2.7. TEM images of maghemite-MWNT prepared with 4:1 mass ratio of $Fe(NO_3)_3 \cdot 9H_2O$ and MWNT. (a) Low magnification image calcinated at 600 °C (Inset: the electron diffraction pattern of the iron oxide nanoparticles), (b) High resolution (HRTEM) image calcinated at 500 ^oC, and (c) High magnification image calcinated at 600 ^oC. TEM images of maghemite-MWNT prepared with 2:1 mass ratio of $Fe(NO_3)_3 \cdot 9H_2O$ and MWNT. (d) Low magnification image calcinated at 600 ^oC, (e) High magnification image calcinated at 500 ^oC, and (f) High magnification image calcinated at 600 ^oC.

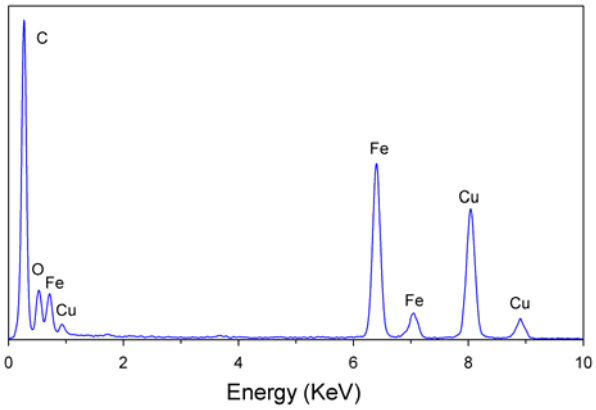

Figure 2.8. EDS of the maghemite-MWNT composite material.

The separation of the nanoparticles on the surface of the MWNT was achieved by electrostatic interactions between the various reactive species in the system. When MWNTs (having negative surface charges as a result of their prior treatment with acid) were added to a $Fe(NO_3)_3 \cdot 9H_2O$ solution and sufficiently sonicated, electrostatic interactions developed between the surface and the Fe centers due to the positive charges of Fe (III) (Figure 2.9). Since the surface sites having negative charges are homogeneously distributed and separated from each other on the surface of the MWNT, the Fe (III) ions also nucleate accordingly to form well-separated nanoparticles.

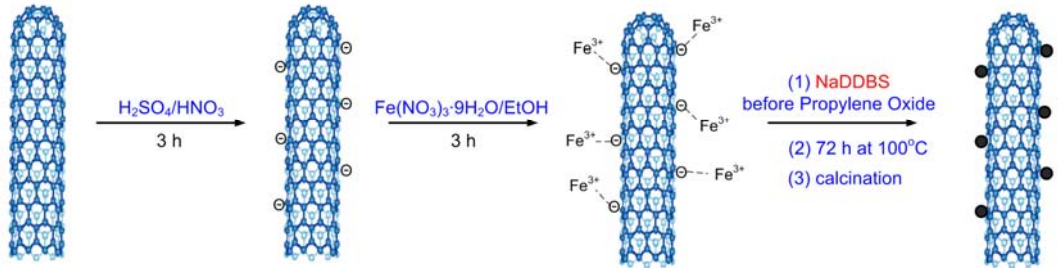

Figure 2.9. Schematic representation of the overall strategy for the preparation of MWNTs/γ-Fe_2O_3 magnetic carbon nanotubes via a modified sol-gel process.

To facilitate the alignment of pure or surface modified CNTs with amine or carboxylic group, it is necessary to generate strong magnetic or electric field.[9,40,41] However, in this system, when a droplet of the reacted dispersion was dried under relatively low magnetic field (≤ 0.3 T), the magnetic carbon nanotubes with mass ratio of 4:1 between the $Fe(NO_3)_3 \cdot 9H_2O$ precursor and the MWNTs were oriented in the plane of a silicon substrate at 300 K (Figure 2.10 (b) and (c)), fact which was made possible due to overcoming thermal motion and rotation. However, surface activated but un-decorated MWNTs did not show aligned features (Figure 2.10 (a)). Therefore, this supports a conclusion that the decoration of the surface of the MWNTs with nanoparticles with good magnetic response, such as γ-Fe_2O_3, can facilitates the alignment of the magnetized carbon nanotubes (i.e., having acquired magnetic properties) even under relatively low magnetic field.

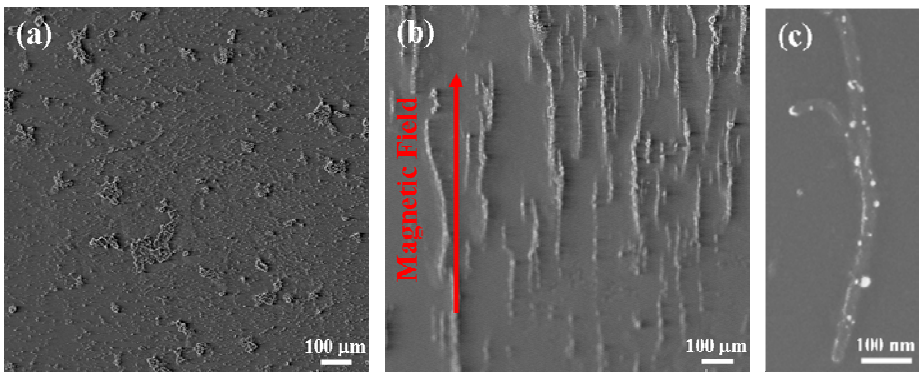

Figure 2.10. SEM images of the composite material in the presence of a magnetic field of 0.3 T. (a) Surface activated but un-decorated MWNTs. (b) Aligned maghemite-MWNT (4:1 mass ratio) calcinated at 600 ^{o}C. (c) A single maghemite-MWNT aligned.

Such nanoparticles (i.e. having an aspect ratio >>1) coming in close to proximity to each other but having parallel magnetization direction at their wall surfaces repel each

other and are offset.[173] However, these magnetic carbon nanotubes have the north and south poles of their dipolar magnet at their top and bottom tips, fact which leads to the alignment (Figure 2.10 (c)).

The magnetic properties of the as-prepared MWNTs/γ-Fe_2O_3 nanocomposites were measured using Superconducting Quantum Interference Device (SQUID) magnetometer. The magnetization hysteresis loops (Figure 2.11) were measured in fields between ±50 kOe at room temperature. The saturation magnetization (M_s) of the samples obtained is below 2 emu g^{-1}, which is considerably smaller than that of bulk iron (M_s = 222 emu g^{-1}) as shown in Table 2.1. Coercivity is below 10 Oe, which is larger than that of bulk iron (H_c = 1 Oe). The conclusion drawn from the measurement of magnetic properties is that both samples, having different ratios between $Fe(NO_3)_3 \cdot 9H_2O$ precursor and MWNT, exhibit superparamagnetic behavior at room temperature. This should be mainly attributed to the small size of γ-Fe_2O_3 nanoparticles that were formed in the presence of MWNTs.[174] This result is in good accordance with the TEM observation of the small sizes of the maghemite nanoparticles mentioned above.

The magnetic attraction of our sample was also tested by placing a magnet near a vial containing the maghemite-MWNT nanostructures suspended in ethanol (Figure 2.11 (c)). The samples can be easily dispersed in solution and form a stable suspension. When a magnet approaches the vial, magnetic carbon nanotubes are attracted toward the magnet. This phenomenon illustrates that the maghemite nanoparticles that are anchored on the surface of the MWNTs impart to the composite material a magnetic response similar to that observed with magnetite.

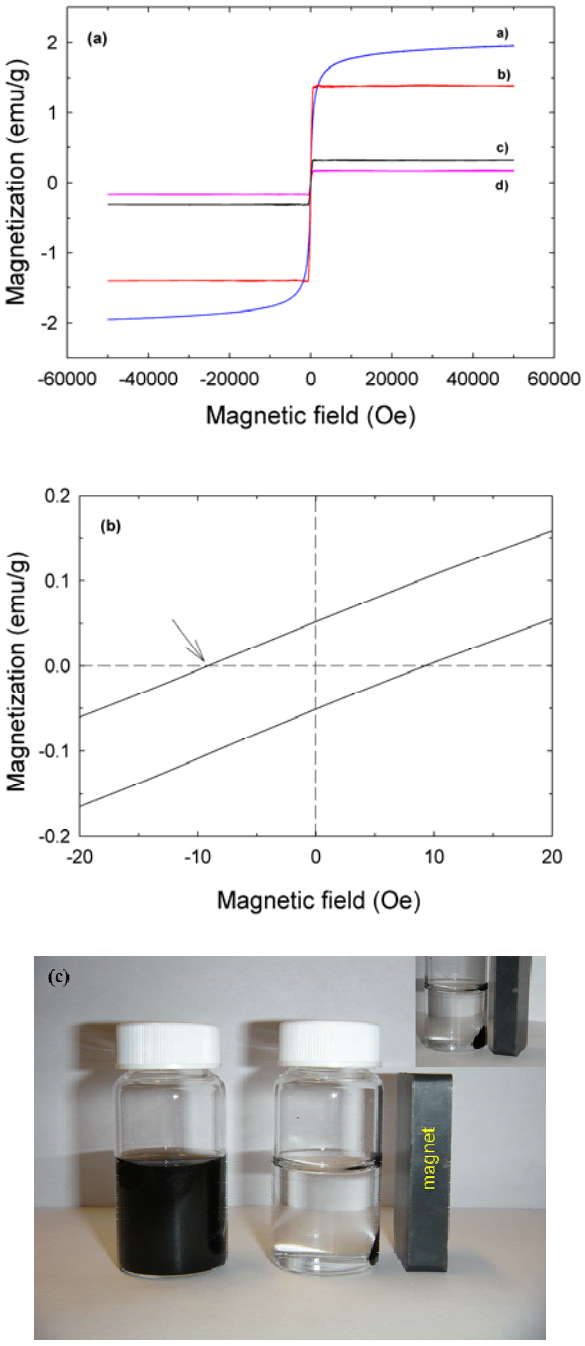

Figure 2.11. (a) Magnetization versus applied magnetic field for the magnetic carbon nanotubes prepared at different mass ratios and temperatures: 4:1 mass ratio of $Fe(NO_3)_3 \cdot 9H_2O$ and MWNT at a) 500 ^oC, b) 600 ^oC, and 2:1 mass ratio of $Fe(NO_3)_3 \cdot 9H_2O$ and MWNT at c) 500 ^oC, d) 600 ^oC. (b) The enlarged hysteresis loop of the maghemite-MWNT structures formed from a 4:1 mass ratio of $Fe(NO_3)_3 \cdot 9H_2O$ and MWNT that was calcinated at 600 ^oC. (c) The photograph of magnetic carbon nanotubes suspended in ethanol in the absence (left image) and in the presence (right image) of an externally-placed magnet. The inset magnifies the attraction of the magnetic carbon nanotubes to the magnet.

Table 2.1. The magnetic properties as a function of both different mass ratio of $Fe(NO_3)_3 \cdot 9H_2O$ and MWNT and different calcinations temperature.

Magnetic properties	Calcination temperature (^oC)	2:1[a]	4:1[a]
M_s (emu g^{-1})[b]	500	0.3	2.0
	600	0.2	1.4
H_c (Oe)[c]	500	4.8	2.8
	600	6.3	9.6

[a] mass ratio of $Fe(NO_3)_3 \cdot 9H_2O$ and MWNT. [b] saturation magnetization. [c] coercivity.

According to the expectations, this novel method for the magnetization of carbon nanotubes through the tethering of magnetic iron oxide nanoparticles with controlled size and site distribution opens up a slew of new opportunities for applications in which the alignment of CNTs is not only desired, but is actually required. While many groups have studied strategies to align MWNT/Fe_3O_4 nanostructures under external magnetic fields due to their strong magnetic properties, very little attention has been devoted to MWNT/γ-Fe_2O_3 conjugate nanomaterials. This latter system also exhibits similar interesting properties and can constitute a facile gateway to MWNT alignment processes under tight morphological control and relatively low magnetic fields. Furthermore, it is noted that in the not-so-distant future this maghemite-CNT hybrid material may be used for biomedical applications such as drug delivery or special medical applications such as cancer diagnosis.[175, 176]

2.4 Conclusions

This study addressed the synthesis of MWNT/γ-Fe_2O_3 nanostructures via an easy and novel modified sol-gel process. It showed that NaDDBS molecules are intimately involved in inhibiting the formation of an iron oxide gel. As a result, well-defined and well-dispersed maghemite nanoparticles could be obtained. In addition, the particle size of these nanoparticles could be precisely modulated by changing the temperature, and the mass ratio of the $Fe(NO_3)_3 \cdot 9H_2O$ precursor and MWNTs. Finally, tethered γ-Fe_2O_3 magnetic nanoparticles on the surface of MWNTs imparted superparamagnetic properties to the composite material. This facilitated the alignment of the decorated MWNTs under externally-applied magnetic field, resulting in the formation of an anisotropic material with enhanced mechanical and electrical characteristics.

CHAPTER 3

ANISOTROPIC CONDUCTIVITY OF MAGNETIC CARBON NANOTUBES EMBEDDED IN EPOXY MATRICES

3.1 Introduction

This Chapter discusses on the anisotropic electrical conductivity of the polymer nanocomposite systems with the as-prepared magnetic carbon nanotubes by applying an external magnetic field. In brief, the tethering of γ-Fe_2O_3 nanoparticles on the surface of MWNT was achieved by a modified sol-gel reaction, where sodium dodecylbenzene sulfonate (NaDDBS) was used in order to inhibit the formation of a 3D iron oxide gel. These hybrid-materials, specifically, magnetized multi-walled carbon nanotubes (m-MWNTs) were readily aligned parallel to the direction of a magnetic field even when using a relatively weak magnetic field. The conductivity of the epoxy composites formed in this manner increased with increasing m-MWNT mass fraction in the polymer matrix. Furthermore, the conductivities parallel to the direction of magnetic field were higher than those in the perpendicular direction, indicating that the alignment of the m-MWNT contributed to the enhancement of the anisotropic electrical properties of the composites in the direction of alignment.

3.2 Experimental

3.2.1 Materials

MWNTs (>99%) produced by chemical vapor deposition followed by HCl mineralization, with 12 nm in diameter and 10 μm in length, were purchased from Aldrich. To activate the surface along the MWNTs, concentrated sulfuric acid (98%) and nitric acid (70%) were purchased from Fisher Scientific. For the preparation of magnetic carbon nanotubes (m-CNTs), ferric nitrate nonahydrate, $Fe(NO_3)_3 \cdot 9H_2O$ was purchased from Acros Organics. Propylene oxide (>99%), absolute ethanol (anhydrous, 200-proof), and sodium dodecylbenzene sulfonate (NaDDBS) were purchased from Aldrich and TCI. In order to make composites with m-CNT, Aeropoxy laminating materials (PR2032 Resin) was used with an appropriate curing agent (PH3660).

3.2.2 Synthesis of Maghemite-MWNT Hybrid Materials

Pure-MWNTs were first dispersed in a solution mixture of concentrated sulfuric acid and nitric acid with the volume ratio of 3:1. The suspension was ultra-sonicated for 3 hrs at room temperature. After that, the concentration of the suspension was diluted up to 50% and filtered with a PTFE membrane (0.45 μm pore size) with the aid of a vacuum pump. Carboxylated MWNT (MWNT-COOH) was washed with de-ionized water several times to reach neutral pH and dried under vacuum at 50 ^{o}C overnight. The synthesis of maghemite-MWNT was performed by first adding 0.65 g $Fe(NO_3)_3 \cdot 9H_2O$ to 20 ml of absolute ethanol (100% purity) and stirring until the $Fe(NO_3)_3 \cdot 9H_2O$ was dissolved completely. Subsequently, this iron salt solution was added to a suspension of oxidized MWNTs with a mass ratio of 4:1 ($Fe(NO_3)_3 \cdot 9H_2O$: MWNTs mass ratio of 4:1), stirred,

and sonicated for 3 hrs. Twenty ml of 1.2 mM of NaDDBS were added to the solution and stirred for 30 min. Then, 1.2 ml of propylene oxide was added as a gelation agent and stirred for 30 min. The mixture was then placed in a Fisher Scientific iso-temperature oven for drying for 3 days at 100 ^{o}C. The resulting powder products were washed with water and ethanol several times and dried at 50 ^{o}C. The calcination of these powders was performed in a furnace under argon atmosphere at 500 ^{o}C for 2 hrs. The overall synthesis strategy is shown in Figure 3.1.

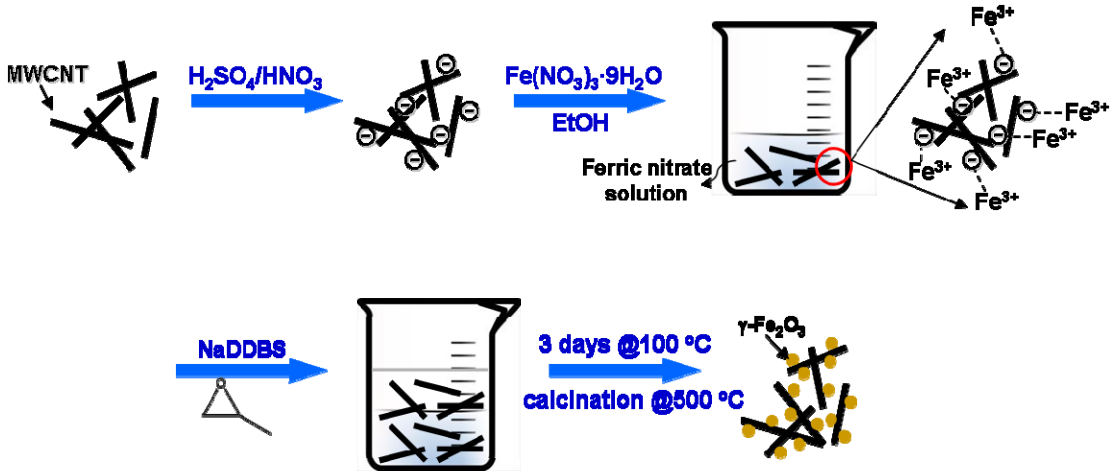

Figure 3.1. Schematic illustration of the overall strategy for the synthesis of maghemite-MWNT hybrid materials via a modified sol-gel process.

3.2.3 Characterization

The dried samples were ground into a fine powder using a ceramic mortar and pestle. XRD measurements were performed using an X'pert Pro Alpha-1 (wavelength of 1.54 Å). XRD peaks were collected from $2\theta = 0^{o}$ to 90^{o} with a step size of 0.02^{o}. XPS scans of powder samples were taken using a Surface Science Laboratories SSX-100 ESCA spectrometer using monochromatic Al Kα radiation (1486.6 eV). The alignment of the sample was conducted by a magnet (GMW-5403) at 0.3 T, and the experimental

apparatus used in this study is depicted schematically in Figure 3.2 (a). The morphology and aligned feature of as-prepared samples were also characterized using SEM (LEO 1530). TEM samples were prepared by placing a droplet of solution onto a TEM grid, and for the observation of aligned features, samples were micro-tomed into 100 nm thick slices using a diamond knife and placed on a TEM grid. These samples were analyzed using a Hitachi HF2000, 200 kV transmission electron microscopy. The electrical conductivity data of as-prepared composites were collected using impedance analyzer (Solartron Instruments SI 1260 with dielectric interface 1296) for the frequency range 0.1 Hz ~ 1 MHz. All the data were collected under an AC voltage of 0.1 V. The setup for electrical measurements of the composites is shown in Figure 3.2 (b). Contact was achieved by silver painting the two ends of the samples, and then using coaxial probers on a probe station attached to the impedance analyzer.

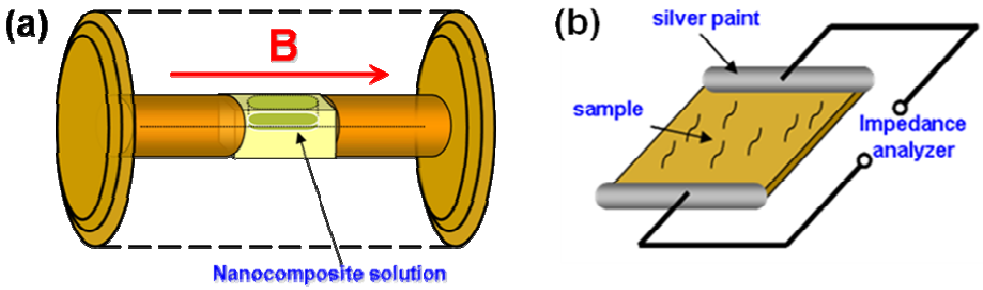

Figure 3.2. The schematic illustration of the alignment of m-MWNT in an epoxy matrix and the measurement of the resulting electrical properties. (a) The application of a magnetic field to the m-MWNT/epoxy nanocomposite solution, and (b) The measurement of electrical conductivity of the resulting nanocomposite material.

3.3 Results and Discussion

3.3.1 Formation of Nearly-Monodisperse and Homogeneously-Distributed Iron Oxide Nanoparticles

The novel key step to impart magnetic properties to the carbon nanotubes is composed of a carefully-designed synthesis method, which involves a modified sol-gel process. The formation of γ-Fe_2O_3 is dependent on the presence of propylene oxide, which acts as an oxide-formation promoter. The general mechanism of γ-Fe_2O_3 formation by the introduction of an epoxide to a hydrated iron nitrate solution has been well established.[164]

In this system, the homogeneous distribution of the iron oxide nanoparticles on the surface of the MWNT was achieved due to the electrostatic interactions between negatively charged surface of the MWNT and the positively charged Fe(III) as shown in Figure 3.1. Given that the negatively-charged surface sites of MWNTs are homogeneously distributed, the Fe(III) ions could nucleate accordingly to form well-separated nanoparticles.

The occurrence of gelation upon the addition of propylene oxide to the solution was inhibited by the addition of surface active molecules, NaDDBS. These molecules coordinate to the Fe(III) centers by electrostatic attractions forming a self-assembled protective layer, resulting in the inhibition of gel formation. Therefore, it is appropriate to refer to this method a *modified* sol-gel process. Finally, due to the presence of the NaDDBS molecules, no aggregates of γ-Fe_2O_3 were formed but rather the nanoparticles remained individually isolated and homogeneously distributed.

3.3.2 Characterization of Magnetic Carbon Nanotubes

Figure 3.3 shows the XRD patterns of the synthesized γ-Fe_2O_3/MWNT, demonstrating the high crystalline nature of the nanoparticles. The diffraction peak at

25.98° could be attributed to the graphite structure (002) of MWNTs. The positions and relative intensities of non-MWNT related new peaks, after surface modification, in the range of 20° < 2θ < 80° correspond to the (220), (311), (400), (422), (511), (440), and (533) reflections of maghemite (γ-Fe_2O_3).

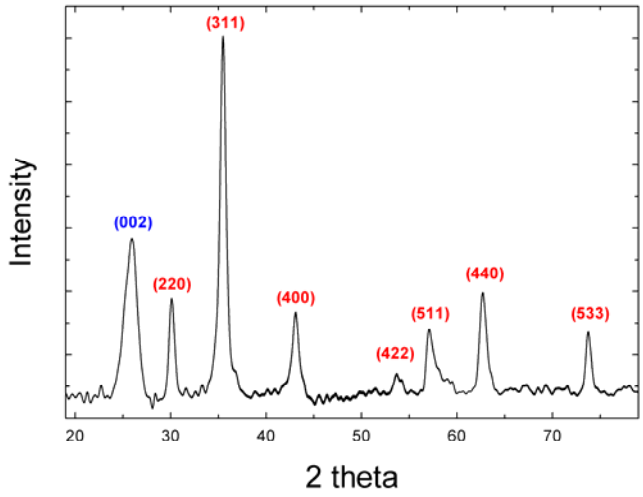

Figure 3.3. The XRD patterns of maghemite/MWNT hybrid structures formed from an initial $Fe(NO_3)_3 \cdot 9H_2O$: MWNTs mass ratio of 4:1, and calcinated at 500 °C.

X-ray photoelectron spectroscopy (XPS) also confirmed that the iron oxide nanoparticles were formed on the surface of MWNT. After the formation of surface treated MWNTs decorated with iron oxide nanoparticles followed by calcination at 500 °C, XPS shows characteristic iron peaks in addition to carbon and oxygen, as shown Figure 3.4 (a). The high-resolution spectrum (Figure 3.4 (b)) indicates that the position of the Fe (2p3/2) and Fe (2p1/2) peaks at 711.3 and 724.4 eV, respectively, are in good agreement with the values reported for γ-Fe_2O_3 in the literature,[171] validating the formation of γ-Fe_2O_3 in our samples.

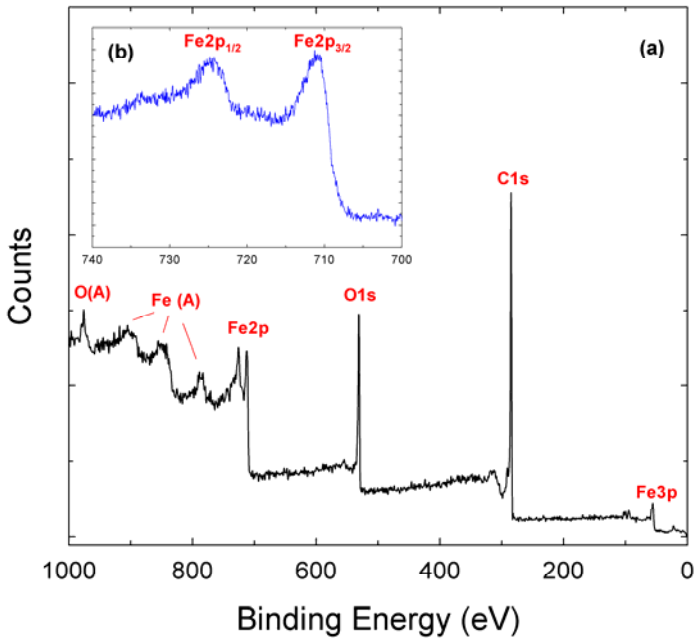

Figure 3.4. (a) The XPS survey spectrum of maghemite/MWNT hybrid structures, and (b) The high resolution XPS spectrum of Fe(2p) bands of the maghemite/MWNT hybrid structures.

3.3.3 Characterization of the Morphology of γ-Fe_2O_3/MWNT

Scanning electron microscopy (SEM) images of m-MWNT confirmed that γ-Fe_2O_3 nanoparticles were attached to the walls of the MWNT as shown in Figure 3.5 (a), and that the size of the attached iron oxide nanoparticles was about 17 nm (Figure 3.5 (c)). The high-resolution transmission electron microscopy (HRTEM) image of a nanoparticle (Figure 3.5 (b)) illustrates the maghemite interlayer spacing of the (311) lattice plane of approximately 0.25 nm.[170] Furthermore, the inset image of Figure 3.5 (b) shows the electron diffraction patterns of maghemite, indicating the high crystallinity of the maghemite nanoparticles. The homogeneous distribution of the nanoparticles on the surface of the MWNT was achieved by the electrostatic interactions between the negatively-charged MWNT and the positively-charged Fe(III) centers (see Figure 3.1), as well as by the introduction of NaDDBS in order to inhibit the formation of 3D iron oxide

networks. The magnetic nature of the as-prepared m-MWNT could also be easily ascertained by placing an external magnet next to the vial containing the m-MWNT, as shown in Figure 3.5 (d).

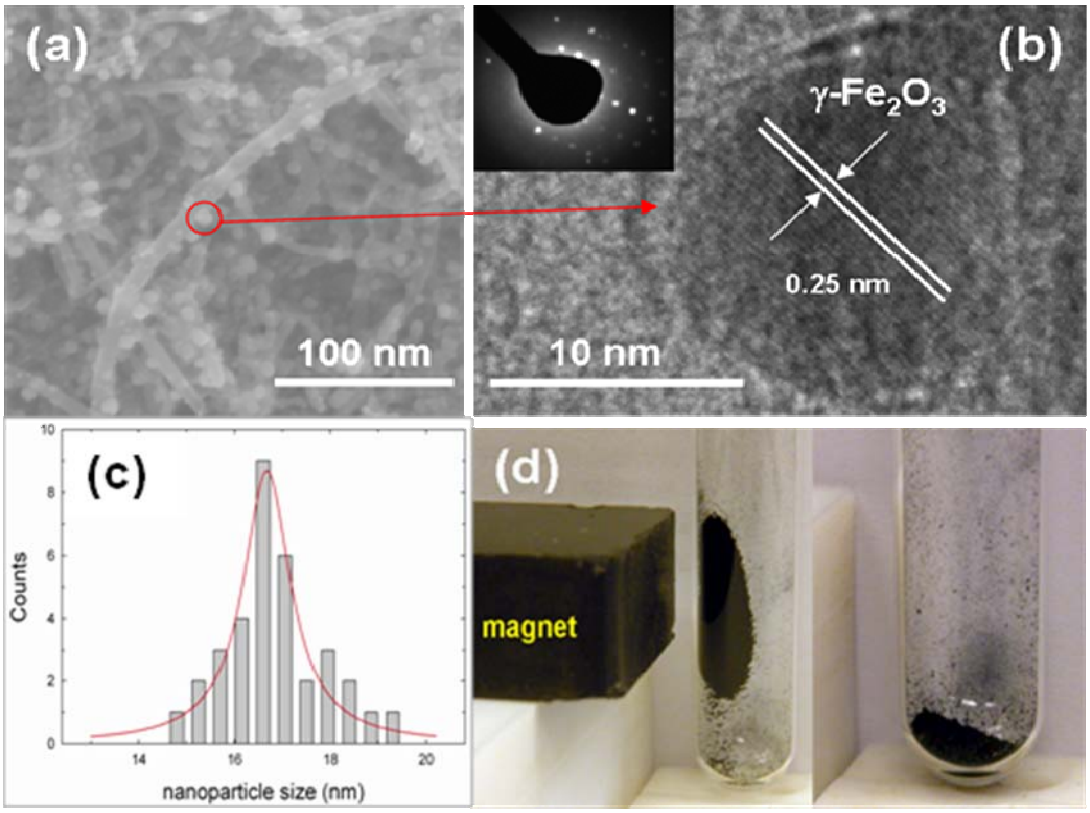

Figure 3.5. (a) SEM image of maghemite/MWNT hybrid structures; (b) High resolution TEM image of maghemite. Inset shows diffractions of a single maghemite nanoparticle; (c) Size distribution of the as-prepared iron oxide nanoparticles in the maghemite/MWNT hybrid structures; (d) The photograph of m-MWNT suspension in the presence (left image) and in the absence (right image) of a magnet.

3.3.4 Alignment of m-MWNTs in Polymer Matrix

The SEM images of m-MWNT hybrid materials are shown in Figure 3.6 (a) and 3.6 (b). When a droplet of dispersed hybrid materials in a water solution was dried under the magnetic field, the surface-modified MWNT were aligned easily (Figure 3.6 (a)). However, when the nanocomposite solution was dried without applying magnetic field,

the surface-modified MWNT did not exhibit alignment features (Figure 3.6 (b)). The TEM images of composites in which surface-modified MWNT (m-MWNT) and unmodified MWNT were embedded in epoxy matrices are shown in Figure 3.6 (c) through 3.6 (f). First, the alignment features of the MWNT/epoxy nanocomposite and the m-MWNT/epoxy nanocomposite systems were compared under the same experimental conditions, i.e. the same strength of the externally-applied magnetic field (0.3 T). Figures 3.6 (c) and 3.6 (d), representing MWNT/epoxy composites with 0.5 wt% MWNT and 1.0 wt% MWNT, respectively, did not reveal any alignment features of filler phase in the polymer matrix under the externally-applied magnetic field. However, in the case of the m-MWNT/epoxy nanocomposite systems also having 0.5 wt% m-MWNT and 1.0 wt% m-MWNT and shown in Figures 3.6 (e) and 3.6 (f), respectively, it is obvious that the m-MWNTs embedded in the epoxy matrix have indeed aligned parallel to the direction of magnetic field (0.3 T). Comparing the alignment features of aligned m-MWNT hybrid materials and aligned m-MWNT/epoxy composites (Figure 3.6 (a), 3.6 (e), and 3.6 (f)), it becomes evident that the m-MWNT hybrid materials in the absence of a polymer matrix show better alignment, fact which could be attributed to the viscosity of the polymer matrix during processing. Therefore, this supports a conclusion that the m-MWNT hybrids can be aligned under a relatively weak magnetic field even when embedded in a polymer matrix.

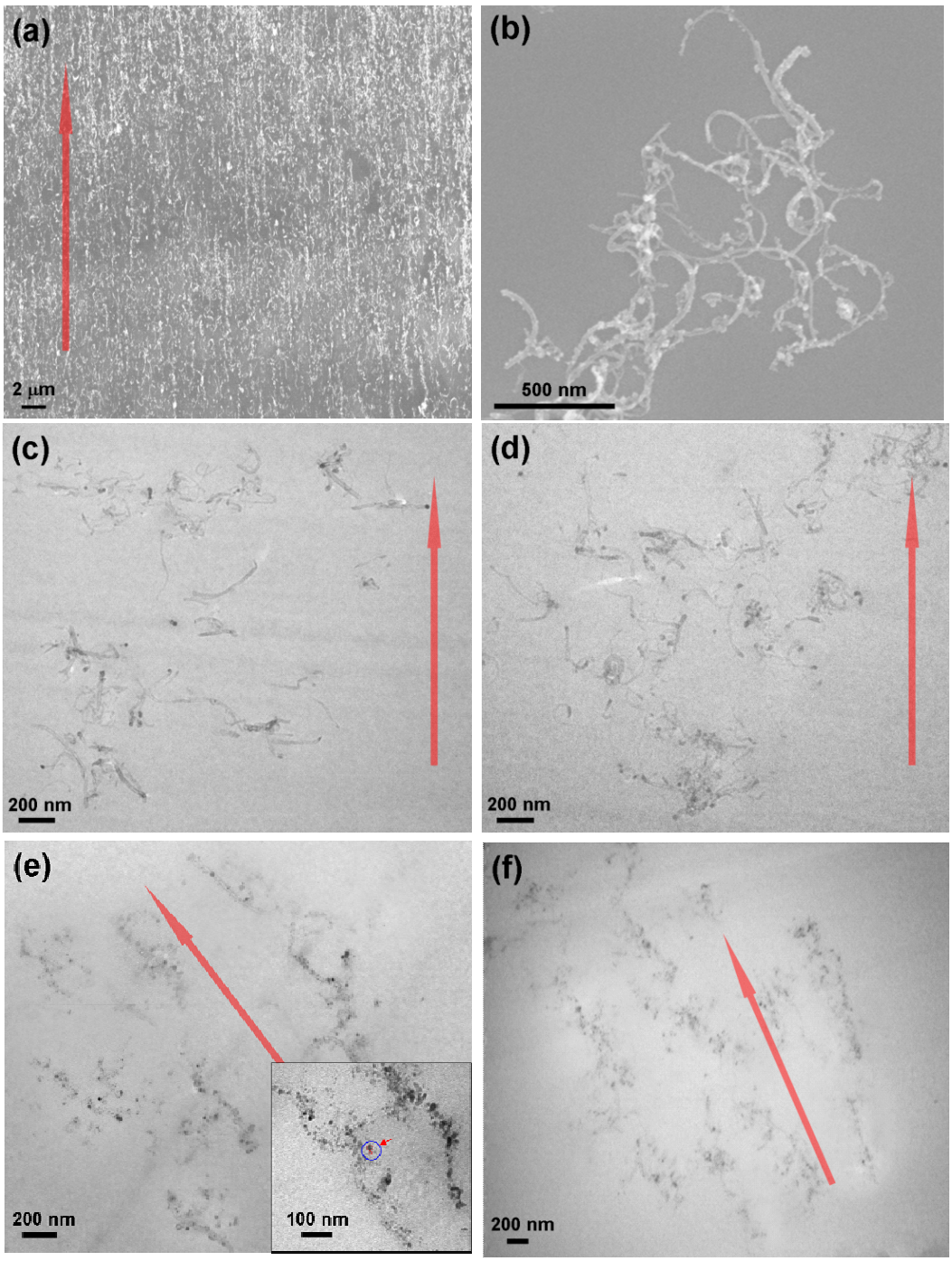

Figure 3.6. (a) SEM image of aligned m-MWNT hybrid materials parallel to the direction of magnetic field; (b) SEM image of m-MWNT hybrid materials that were not subjected to a magnetic field; (c) TEM image of MWNT/epoxy composites with 0.5 wt% filler loading; (d) TEM image of MWNT/epoxy composites with 1.0 wt% filler loading; (e) TEM images of m-MWNT/epoxy composites with 0.5 wt% filler loading. Inset shows the end-to-top connectivity between two m-MWNTs under an external magnetic field; (f) TEM image of m-MWNT/epoxy composites with 1.0 wt% filler loading.

This alignment is expected to directly affect the anisotropic conductivity of the resulting epoxy composites, as will be shown in the subsequent section (Figure 3.7 and 3.8). The bundling of the m-MWNTs in the polymer matrix, as observed in the inset in Figure 3.6 (e), may be attributed to the anisotropic nature of the dipolar interactions of the iron oxide nanoparticles near the ends of the carbon nanotubes, i.e. the near-linear stacking of the north and south poles of the m-MWNT in the polymer matrix, resulting in their observed end-to-top connectivity.[39, 177]

3.3.5 Anisotropic Conductivity of Polymer Composites

The electric conductivities of the m-MWNT/epoxy composites were measured at a series of different frequencies, from 0.1 Hz to 1 MHz. Figure 3.7 shows various conductivities of a series of m-MWNT/epoxy nanocomposite samples containing various degrees of loading (weight percent) of m-MWNT in the polymer matrix. At the same magnetic field (0.3 T), the conductivity increased with increasing m-MWNT mass fraction in the composite. In the case of 0.1 wt% filler content, the nanocomposite exhibited dielectric behavior because the low fraction of m-MWNT made it difficult to form interconnected m-MWNT networks that would have facilitated electron flow. However, for m-MWNT contents of 0.5 w% and higher, the samples exhibited increased conductivity as a function of increased fraction of the m-MWNT moiety.

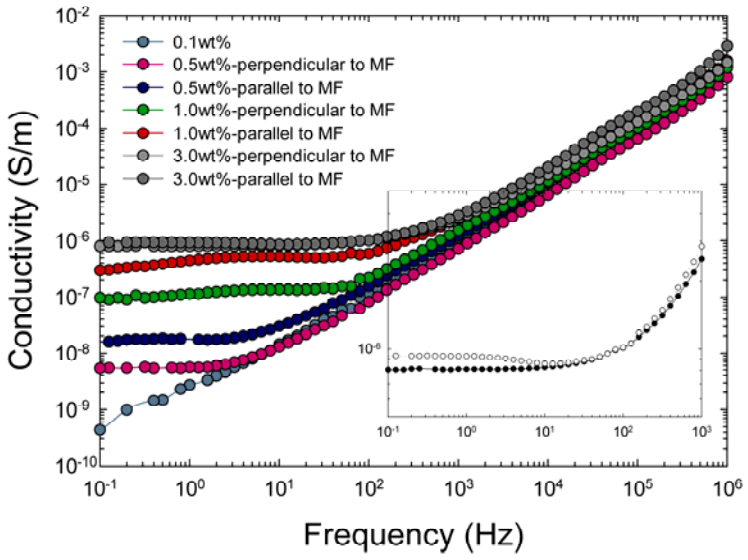

Figure 3.7. The conductivity of m-MWNT/epoxy composites as a function of frequency for different mass fractions of m-MWNT as measured in the direction parallel to the magnetic field and perpendicular to the magnetic field (inset shows magnified region of a nanocomposite with a 3.0 wt% filler loading).

Percolation theory predicts a critical concentration or percolation threshold where the material converts from a capacitor to a conductor.[18, 178] In order to determine the percolation threshold of this aligned system, the volume conductivity data could be fitted to a power law in terms of volume fraction of m-MWNT.

$$\sigma_c \propto (v - v_c)^t$$

Where σ_c is the composite conductivity, v is the m-MWNT volume fraction in the composite, v_c is the critical volume fraction, and t is the critical exponent. It is assumed that the density of m-MWNT is the same as that of unmodified-MWNT (2.1 g/cm^3), since both mass and volume of m-MWNT increase similarly. Figure 3.8 inset shows the plot of σ_c as a function of $v - v_c$ for the parallel measurements. The linear fit to

the data generated a straight line with v_c = 0.2 vol% (corresponding to 0.4 wt%), which gives a good fit.

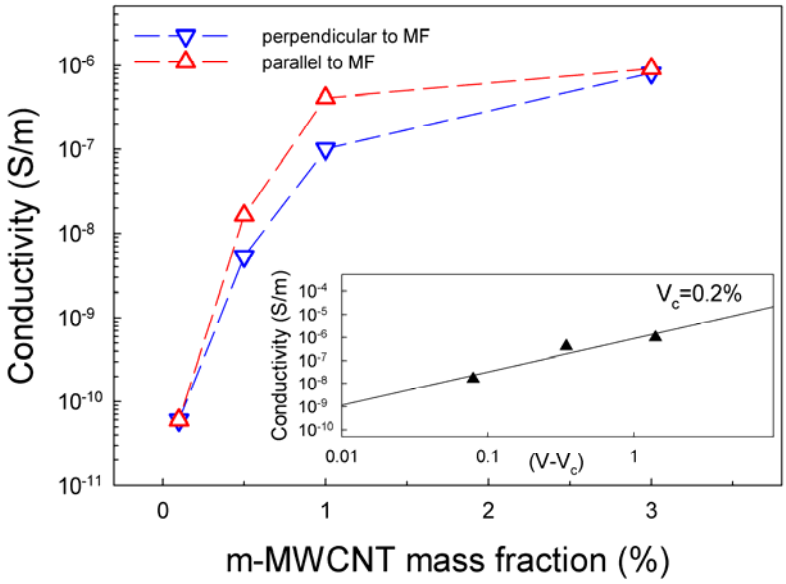

Figure 3.8. The conductivity of m-MWNT/epoxy composites as a function of different mass fractions of m-MWNT measured in the direction parallel to the magnetic field and perpendicular to it. Inset: Percolation equation fit to the experimental conductivity data of obtained parallel to the direction of the magnetic field.

When comparing the results of samples in which conductivity was measured in the direction of the m-MWNT alignment (parallel to the magnetic field) and perpendicular to the m-MWNT alignment (perpendicular direction to the magnetic field) for the same mass fraction of m-MWNT, it is observed that the conductivity measured parallel to the magnetic field was higher than that measured perpendicular to the magnetic field, indicating a cooperative effect due to the alignment of the magnetic carbon nanotubes in the polymer matrix, as was previously shown in Figure 3.6 (e) and 3.6 (f). Figure 3.8 shows the variation of the conductivities measured at a frequency of 0.1 Hz as a function of m-MWNT mass fractions in the epoxy nanocomposite for both

the parallel and perpendicular directions with respect to the magnetic field. The measured conductivities are summarized in Table 3.1.

Table 3.1. The conductivities of m-MWNT/epoxy composites in the directions that were parallel and perpendicular to the externally-applied magnetic field as a function of m-MWNT mass loading.

m-MWNT loading (wt%)	Conductivity (S/m)		Conductivity ratio of // and ⊥
	Parallel (//)	Perpendicular (⊥)	
3.0	1.0×10^{-6}	8.5×10^{-7}	1.2
1.0	4.1×10^{-7}	1.0×10^{-7}	4.1
0.5	1.6×10^{-8}	5.3×10^{-9}	3.0
0.1	6.0×10^{-11}		1.0

It is noted that for 3.0 wt% m-MWNT sample, even though the conductivity in the parallel direction was somewhat larger than that in the perpendicular direction (see Figure 3.7 inset and Figure 3.8), the values obtained nevertheless, quite similar. This is most likely due to the following factors: (a) It is assumed that the viscosity of the composite solution containing 3.0 wt% m-MWNT is higher than for other compositions as evidenced by the superior alignment of m-MWNT without polymer matrix to that of m-MWNT/epoxy composites, as discussed in a previous section. By introducing higher mass loadings of the carbon nanotubes into the polymer solution, the viscosity of the system could be further increased, fact which could then handicap with the alignment process. Therefore, this supports a conclusion that when the magnetic field was applied to the 3.0 wt% m-MWNT sample, the alignment of the decorated carbon nanotubes was not as effective as in the less concentrated samples, and hence, the differences between the conductivities in the parallel and the perpendicular directions were not as pronounced, mainly due to the higher viscosity of the solution. (b) In addition, the conductivity of 3.0

wt% m-MWNT sample (measured in either direction) was not much higher than the conductivity of the 1.0 wt% m-MWNT sample (see Figure 3.8). Tethered iron oxide (maghemite) nanoparticle has high resistivity.[179] Hence, the higher viscosity of the 3.0 wt% m-MWNT sample may lead to the formation of iron oxide rich regions, resulting in a decrease of the conductivity.

3.4 Conclusions

This study addressed the development of a novel method to form magnetic carbon nanotubes using a simple modified sol-gel technique as well as the achievement of m-MWNT/epoxy composites having magnetic field induced anisotropic electrical conductivities. The modified sol-gel technique for the tethering of maghemite nanoparticles to the surface of acid-activated MWNTs generated nearly-monodispersed and homogeneously spaced γ-Fe_2O_3 nanoparticles, which in turn, imparted magnetic properties to the γ-Fe_2O_3/MWNT hybrid materials. Due to the acquired magnetic property of the m-MWNTs, they could be aligned either alone or embedded in a polymer matrix by the application of only a relatively weak magnetic field. Conductivity measurements performed on m-MWNT/epoxy composites showed that the conductivity of the m-MWNT/epoxy composites increased with increasing m-MWNT contents with low percolation threshold (~0.4–0.5 wt% m-MWNT loading). Moreover, the conductivity measured in the direction parallel to the magnetic field was higher than that measured in the direction perpendicular to it. However, the alignment of a nanocomposite sample having a loading of 3.0 wt% m-MWNT was not as effective as samples with lower nanofiller content because of the higher solution viscosity in the more concentrated

samples. This hurdle could, in principle, be overcome by applying a stronger magnetic field. In summary, this facile magnetic functionalization method could be effectively applied for the development of conductive films, composites with conductive polymers, and bio-based composites with aligned features.

CHAPTER 4

CRYSTALLIZATION KINETICS AND ANISOTROPIC PROPERTIES OF POLYETHYLENE OXIDE/MAGNETIC CARBON NANOTUBES COMPOSITE FILMS

4.1 Introduction

This Chapter discusses on the characteristics of the nanocomposite films with semi-crystalline polymer and magnetic carbon nanotubes. Semicrystalline polymer matrices filled with CNTs have been extensively studied, particularly given the fact that CNTs have the potential to nucleate the polymer crystallization.[16, 62-64] One example of semicrystalline polymers is the biodegradable and biocompatible polyethylene oxide (PEO), a polymer that has drawn extensive attention because of its potential use in drug delivery, tissue engineering, packing materials, etc.[65-67]

Thus, this Chpater will address a method of fabricating electrically conductive and flexible PEO composite films with magnetic carbon nanotubes (m-CNTs) that were placed under a weak magnetic field. Two distinct phenomena are explored:

1. Crystallization kinetics of the polymer in the PEO-m-CNTs composite films. The tethered magnetic nanoparticles may act as nucleating agents, resulting in the increase in the crystallization rate of PEO.

2. Application of a weak magnetic field to the composite solution during the consolidation phase of the composite may induce the alignment of the m-CNTs in the direction of the magnetic field. This in turn may affect the the anisotropic electrical and mechanical properties of the composite.

4.2 Experimental

4.2.1 Preparation of Maghemite-MWNT Nanohybrid Materials

The nanohybrid nanoparticles (γ-Fe_2O_3/MWNT) were synthesized as described previously.[180, 181] In brief, the synthesis of γ-Fe_2O_3/MWNT was performed by first adding 0.65 g $Fe(NO_3)_3 \cdot 9H_2O$ to 20 ml of absolute ethanol (100% purity) and stirring until the $Fe(NO_3)_3 \cdot 9H_2O$ was dissolved completely. Subsequently, this iron salt solution was added to a suspension of oxidized MWNTs with a mass ratio of 4:1 ($Fe(NO_3)_3 \cdot 9H_2O$: MWNTs mass ratio of 4:1), stirred, and sonicated for 3 hrs. Twenty ml of 1.2 mM of NaDDBS (sodium dodecyl benzene sulfonate) were added to the solution and stirred for 30 min. Then, 1.2 ml of propylene oxide was added as a gelation agent and stirred for 30 min. The mixture was then placed in a Fisher Scientific iso-temperature oven for drying for 3 days at 100 ^oC. The resulting powder products were washed with ethanol several times and dried at 50 ^oC. The calcination of these powders was performed in a furnace under argon atmosphere at 500 ^oC for 2 hrs.

4.2.2 Fabrication of Polyethylene Oxide (PEO)/Magnetic Carbon Nanotubes (m-CNTs) Composite Films

1.5 g of PEO with a molecular weight of 300,000 g/mol purchased from Aldrich was completely dissolved in 40 ml of deinoized water at 50 ^oC. Various weight percents of m-CNTs were dispersed in 10 ml of ethanol, sonicated for 1 hr, and mixed with PEO solution in a three-neck flask. The mixture was stirred with mechanical stirrer at 50 ^oC for 12 hrs. After that, these polymer solutions were degassed under vacuum, transferred to glass molds, and dried overnight at 50 ^oC in an oven.

For the preparation of samples with aligned m-CNTs in the PEO matrix, a low magnetic field (below 0.3 T) was applied to a polymer solution for 1 hr at 50 ^{o}C and dried post-alignment overnight at 50 ^{o}C in an oven. The overall scheme is shown in Figure 4.1.

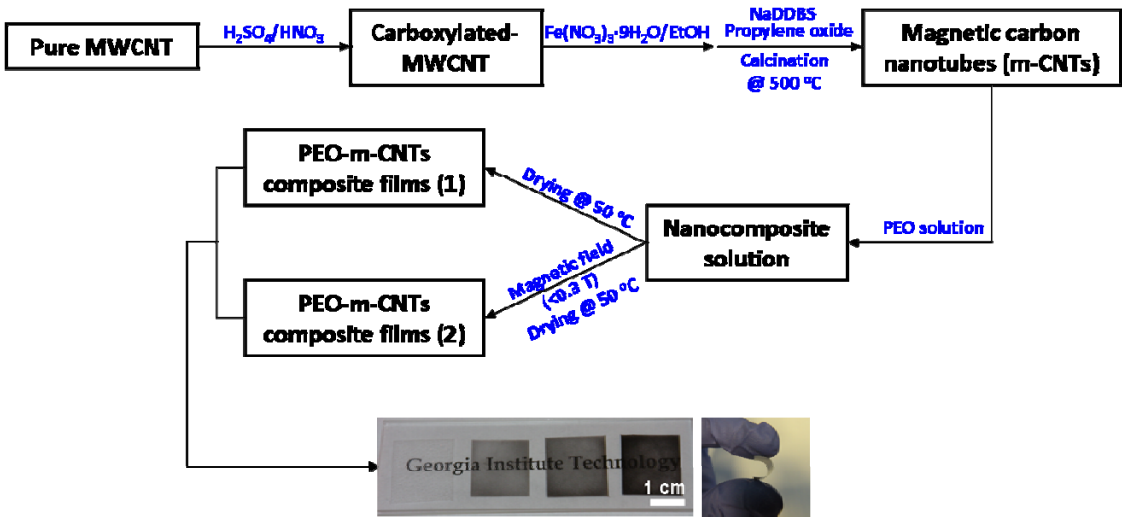

Figure 4.1. Schematic representation of overall strategy for producing PEO-m-CNTs composite films.

4.2.3 Characterization of PEO-m-CNTs Composite Films

Wide Angle X-ray scattering (WAXS) experiments were performed with a Rigaku Micro Max 002 X-ray generator (x-ray wavelength, λ = 0.15418 nm) using Rigaku R-axis IV++ detection system. The morphology of as-prepared samples was characterized using SEM (LEO 1530). TEM samples were prepared by placing a droplet of solution onto a TEM grid. These samples were analyzed using a Hitachi HF2000, 200 kV transmission electron microscope.

The electrical conductivity data of as-prepared composite films were collected using an impedance analyzer (Solartron Instruments SI 1260 with dielectric interface 1296) for the frequency range 0.1 Hz ~ 1 MHz. All the data were collected under an AC

voltage of 0.1 V. Contact was achieved by silver painting the two ends of the samples, and then using coaxial probers on a probe station attached to the impedance analyzer.

The mechanical properties of the nanocomposite specimens were evaluated at room temperature according to the ASTM 638 test method using tensile tester (MTS Insight 2, TestWorks®4 software) with a dog-bone-type dumb-bell specimen. The measurement conditions that were used are as follows: date acquisition rate = 30 Hz; cross-head speed = 10 mm/min; load cell = 100 N.

Crystallization analysis was conducted using a TA Instruments Q100 differential scanning calorimetry (DSC), under both non-isothermal and isothermal conditions. For non-isothermal experiments, heating/cooling rate was 10 ^{o}C/min, where samples were melted at 100 ^{o}C for 5 min. To examine PEO isothermal crystallization rate, samples were heated to 100 ^{o}C, held at that temperature for 5 min, followed by fast cooling (100 ^{o}C/min) to isothermal crystallization temperatures (T_c), holding at each temperature for a required time to finish the crystallization process.

4.3 Results and Discussion

4.3.1 Morphology of Magnetic Carbon Nanotubes and Their Aligned Features in PEO

Scanning electron microscopy (SEM) image of m-CNTs confirmed that γ-Fe_2O_3 nanoparticles were attached to the walls of the CNTs as shown in Figure 4.2. The inset image of Figure 4.2 shows the electron diffraction patterns of maghemite, indicating the high crystallinity of the maghemite nanoparticles.

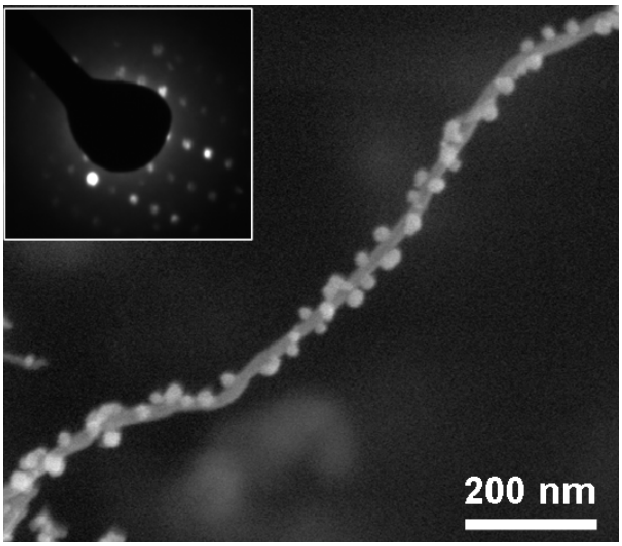

Figure 4.2. The SEM image of as-prepared magnetic carbon nanotubes; inset shows the diffraction pattern of tethered magnetic nanoparticles on the surface of CNTs.

The homogeneous distribution of the nanoparticles on the surface of the MWNT was achieved by the electrostatic interactions between the negatively-charged MWNT and the positively-charged Fe(III) centers as well as by the introduction of NaDDBS in order to inhibit the formation of 3D iron oxide networks.[180]

Figure 4.3 shows optical microscopy images of composite films with different weight fraction of m-CNTs in the PEO matrix. The composite films that were subjected to an externally-applied magnetic field (below 0.3 T) during their preparation show linear dark streaks, which illustrate the long range order of m-CNTs in the PEO matrix. This is due to the anisotropic nature of the dipolar interactions of the iron oxide nanoparticles near the ends of the CNTs, resulting in their observed end-to-top connectivity.[39, 181]

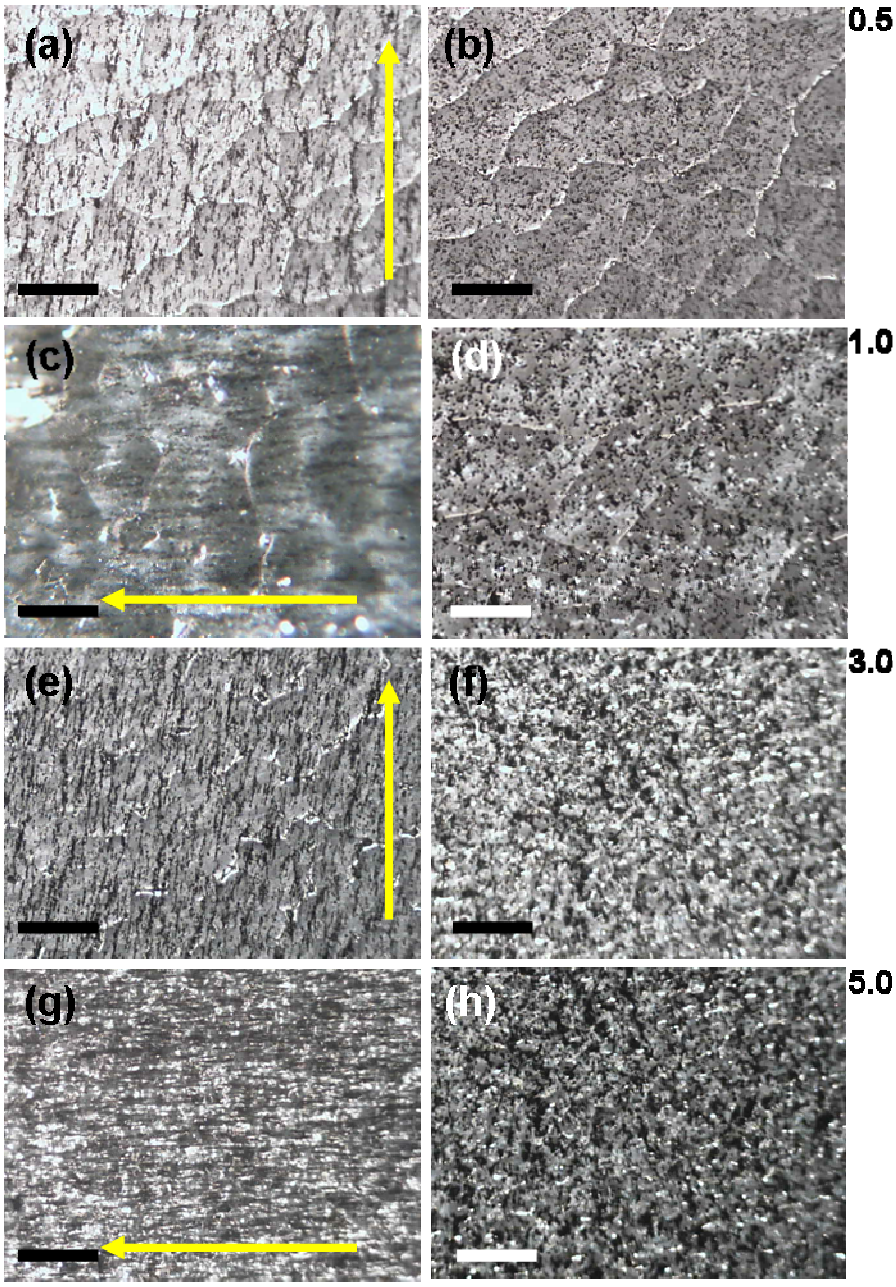

Figure 4.3. Optical microscope images of PEO-m-CNTs at (a) 0.5 wt% applied to magnetic field (MF) and (b) without MF; (c) 1.0 wt% applied to MF and (d) without MF; (e) 3.0 wt% applied to MF and (f) without MF; (g) 5.0 wt% applied to MF and (h) without MF. The scale bar is 100 μm.

4.3.2 Crystallinity and X-ray Diffraction Analysis of the PEO-m-CNTs Composite Films

The melting temperature (T_m) and crystallinity (X_c) of pure-PEO and PEO-m-CNTs composite films were measured using DSC. Chatterjee et al. and Jin et al. have prepared surfactant assisted dispersions of SWNTs and chemically modified MWNTs in PEO, respectively, and found reductions in T_m with increase in CNTs content.[69, 70] Conversely, Goh et al. reported that the thermal properties do not experience any significant variation with respect to the homopolymer for SWNT concentrations up to 7%.[68] During the second heating run in this study, T_m decreased with increasing mass fraction of m-CNTs. However, the extent of decrease of T_m is very small, illustrating the preservation of the thermal properties of composites as shown in Table 4.1.

The degrees of crystallinity of the various samples were calculated by the equation:

$$X_c = \frac{\Delta H_i}{f_i \Delta H_i^m} \times 100$$

where ΔH_i is the enthalpy of fusion of the prepared samples, directly obtained from the DSC measurements, f_i is the mass fraction of polymer in composites, and ΔH_i^m is the enthalpy of fusion of 100% crystalline polymer, which is 205 J/g for PEO. Figure 4.4 shows the crystallinity of as-prepared composite films as a function of m-CNTs content. The crystallinity decreases with increasing weight fraction of m-CNTs. In nanocomposite system with non-covalent interactions, strong attractions between nanofillers and polymer chains could inhibit polymer crystallinity by constraining polymer motion at the interface between the two moieties.[182-184] When examined the first

heating run as shown in Figure 4.4 and Table 4.1, it is observed that the crystallinities of both unaligned and aligned samples at the same m-CNTs content show similar values. To analyze this, wide angle X-ray diffraction (WAXD) measurement was conducted for pure-PEO and PEO-m-CNTs composite films.

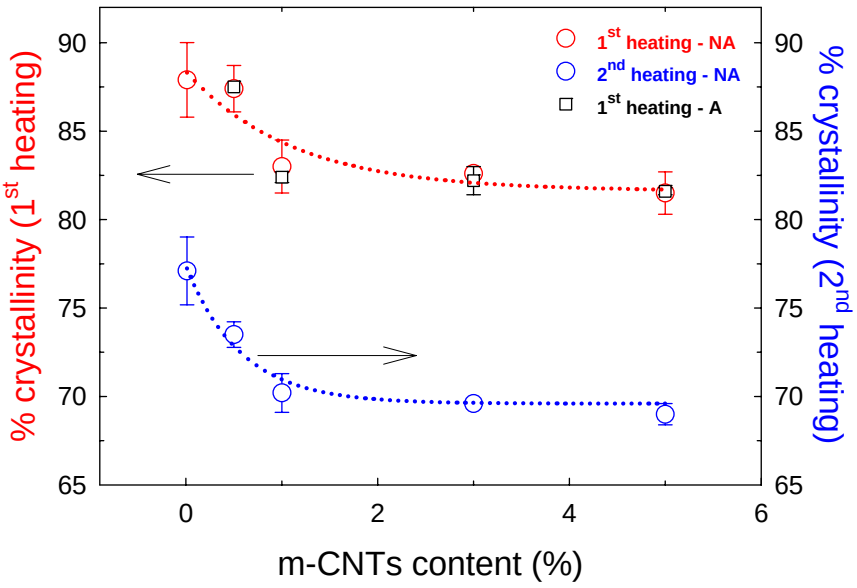

Figure 4.4. The crystallinities as a function of magnetic carbon nanotubes content. (NA: unaligned sample; A: aligned sample)

Tabel 4.1. Melting temperatures and crystallinities of pure PEO and PEO-m-CNTs composite films.

Samples	$T_{m\text{-}1st}$ (℃)	$X_{c\text{-}1st}$[c](%)	$T_{m\text{-}2nd}$ (℃)	$X_{c\text{-}2nd}$ (%)
PEO	67.2 ± 0.6	87.9 ± 2.1	64.8 ± 0.5	77.1 ± 1.9
0.5 wt%-NA[a]	66.4 ± 0.1	87.4 ± 1.3	64.0 ± 0.3	73.5 ± 0.7
0.5 wt%-A[b]	66.9 ± 0.2	87.5 ± 0.5	64.2 ± 0.2	73.5 ± 0.8
1.0 wt%-NA	65.5 ± 0.4	83.0 ± 1.5	63.0 ± 0.1	70.2 ± 1.1
1.0 wt%-A	65.2 ± 0.1	82.4 ± 0.3	62.8 ± 0.1	69.3 ± 0.3
3.0 wt%-NA	66.2 ± 0.2	82.6 ± 0.3	63.3 ± 0.2	69.6 ± 0.2
3.0 wt%-A	65.9 ± 0.3	82.2 ± 0.9	63.4 ± 0.3	68.4 ± 1.6
5.0 wt%-NA	66.0 ± 0.3	81.5 ± 1.3	63.2 ± 0.1	69.0 ± 0.6
5.0 wt%-A	66.0 ± 0.1	81.6 ± 0.8	63.2 ± 0.1	69.1 ± 0.3

[a] isotropic (i.e. unaligned) samples; [b] anisotropic (i.e. aligned) samples; [c] crystallinity

The monoclinic unit cell of PEO crystals is defined by the parameters a = 0.805 nm, b = 1.304 nm, c = 1.948 nm, and the angle β = 125.4°.[185-188] The WAXS pattern of the PEO has a scattering angle at 2θ = 19.2° corresponding to the reflections from the (120) plane and at 2θ = 23.3° containing the overlapping reflections from the (032), $(\bar{1}32)$, (112), $(\bar{2}12)$, $(\bar{1}24)$, $(\bar{2}04)$, and (004) planes, all which have similar d-spacing of ≈ 0.39 nm.[187]

Figure 4.5 shows X-ray diffraction patterns for pure-PEO and 5.0 wt% of PEO-m-CNTs composite film where the m-CNTs phase had alignment features. WAXD measurements with both parallel and perpendicular directions were performed in order to characterize and analyze the induced orientation of the polymer chains due to the alignment of m-CNTs as shown in Figure 4.5 (a). In the case of pure-PEO film, the 2D WAXD patterns of both parallel and perpendicular directions was isotropic, illustrating isotropic orientation of the PEO unit cell. To compare this to aligned and unaligned composite films, XRD measurements for all the samples were also conducted, i.e., 0.5, 1.0, 3.0 and 5.0 wt% with and without alignment of the m-CNTs in the polymer matrix. For example, in the case of 5.0 wt% composite film having an aligned phase of m-CNTs, the 2D patterns for both the parallel and perpendicular directions were similar, indicating that there were no specific preferential orientations of the polymer chains. Other samples (data not shown here) also showed similar isotropic patterns. This result could be explained as follows: (1) PEO has a helical conformation in the unit-cell,[189-191] which causes a distorted helix structure around the nanotubes. Thus, in the case of SWNTs, it has been known that PEO could wrap and coat most of the surface of the SWNTs.[189, 191] Conversely, in the case of MWNTs, given that their diameter is much larger than that of

the SWNTs, the PEO chains could adsorb onto the surface of the MWNTs in an amorphous phase without being subjected to geometric constraints ($D_{MWCNT} \geq Rg_{PEO}$), as shown in Figure 4.5 (d); (2) The carbon nanotubes were tethered with iron oxide nanoparticles. Given the previous experience with polymer – metal oxide interactions,[53] is reasonable to assume that the nanoparticles interact with the polymer chains, resulting in both the decrease of crystallinity as a function of m-CNTs content, and the increase of the mechanical properties due to the reinforcing effect of such interactions (as will be discussed in the section 4.3.5). Thus, this interaction does not contribute to a preferential arrangement of the polymer chains, neither on the surface of the nanotubes, nor in the "bulk" moiety. As a result, even though m-CNTs have unidirectional alignment in the polymer matrix, the PEO chains randomly adsorb on the surface of the MWNTs without any directionality. Therefore, this is in good agreement with the DSC results, in which the crystallinity of both aligned and unaligned samples at the same weight fraction of m-CNTs in polymer has similar values.

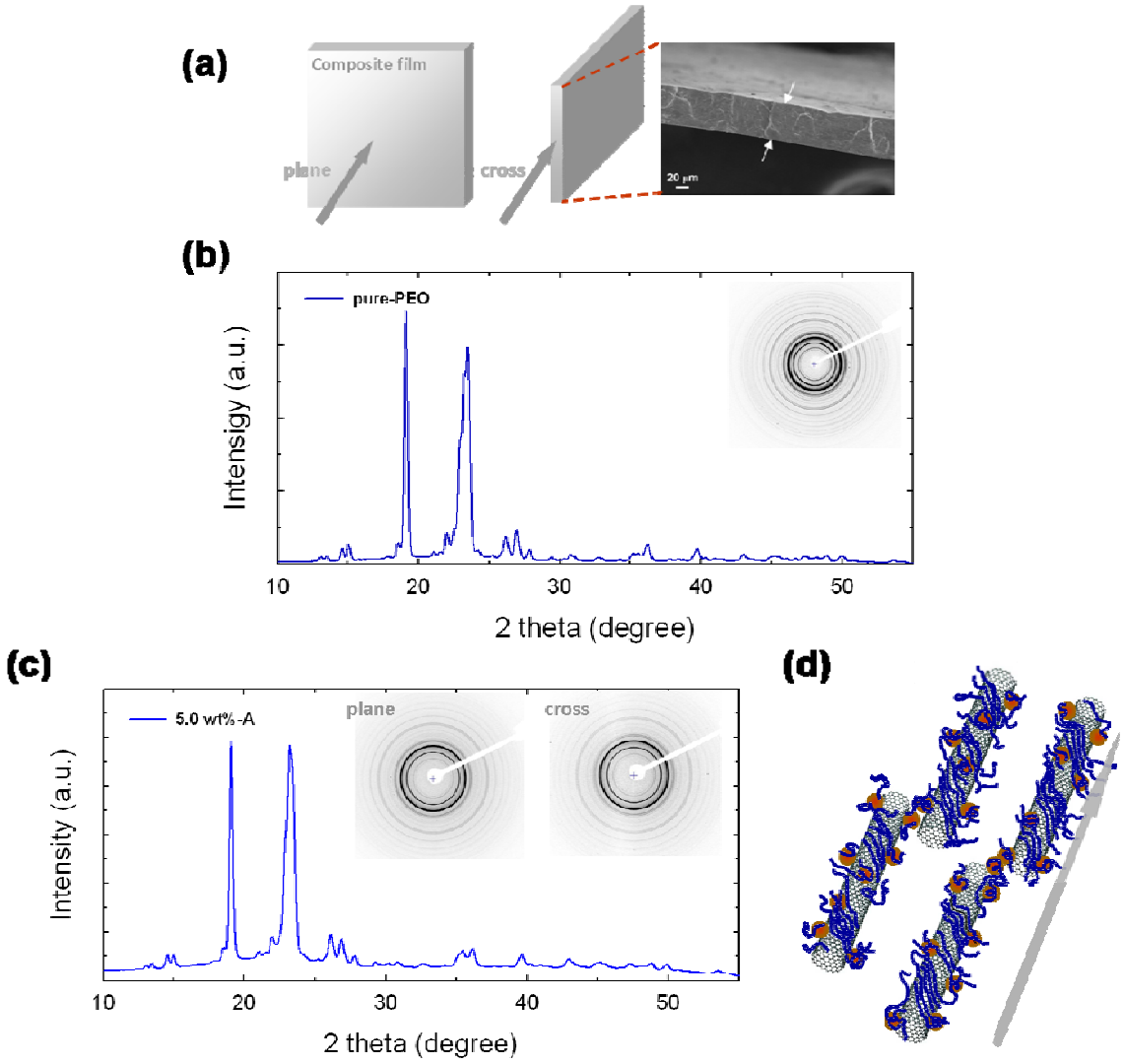

Figure 4.5. (a) Schematic representation of the sample preparation for Wide angle X-ray diffraction (WAXD) measurement. (b) Integrated X-ray diffraction intensity as a function of 2θ of pure-PEO film. Inset: 2D WAXD pattern of pure-PEO film measured to the plane direction. (c) Integrated X-ray diffraction intensity vs. 2θ of PEO-m-CNTs composite film of 5.0 wt% aligned sample. Inset: 2D WAXD patterns measured to both the plane and cross directions. (d) Schematic illustration of the interaction between PEO and m-CNTs.

4.3.3 Crystallization Behavior of the PEO-m-CNTs Composite Films

In order to obtain isothermal crystallization, differential scanning calorimetry (DSC) was used , where the temperature was increased above melting point, held at that temperature, and fast cooled to the target crystallization temperature until the

crystallization kinetics are terminated. Figure 4.6 (a) and (b) show the heat flow as a function of the time. By integrating the heat flow as a function of time using following formula, the plots of the relative crystallinity of the nanocomposite could be obtained as shown in Figure 4.6 (c) and (d).

$$Xt = \frac{\int_0^t (dH / dt)dt}{\int_0^\infty (dH / dt)dt}$$

Where *dH/dt* is the rate of heat flow, the numerator is the heat generated at time t and denominator is the total heat generated up to complete crystallization.

The plots of the relative crystallinity of the nanocomposite by the integration of the heat flow as a function of time are conducted for two sets of experimental conditions: At a crystallization temperature of 50 ^{o}C for three different samples having different m-CNTs concentrations (Figure 4. 6(c)), and at three different crystallization temperatures for a sample containing 5 wt% m-CNTs (Figure 4.6 (d)). It is noted that when the mass loading of m-CNTs in PEO increases at a given crystallization temperature, the crystallization rate increases as well. In addition, for the same mass loading of m-CNTs, the crystallization rate increased with decreasing crystallization temperature, indicating that the crystallization temperature is an important influencing factor determining the crystallization time.

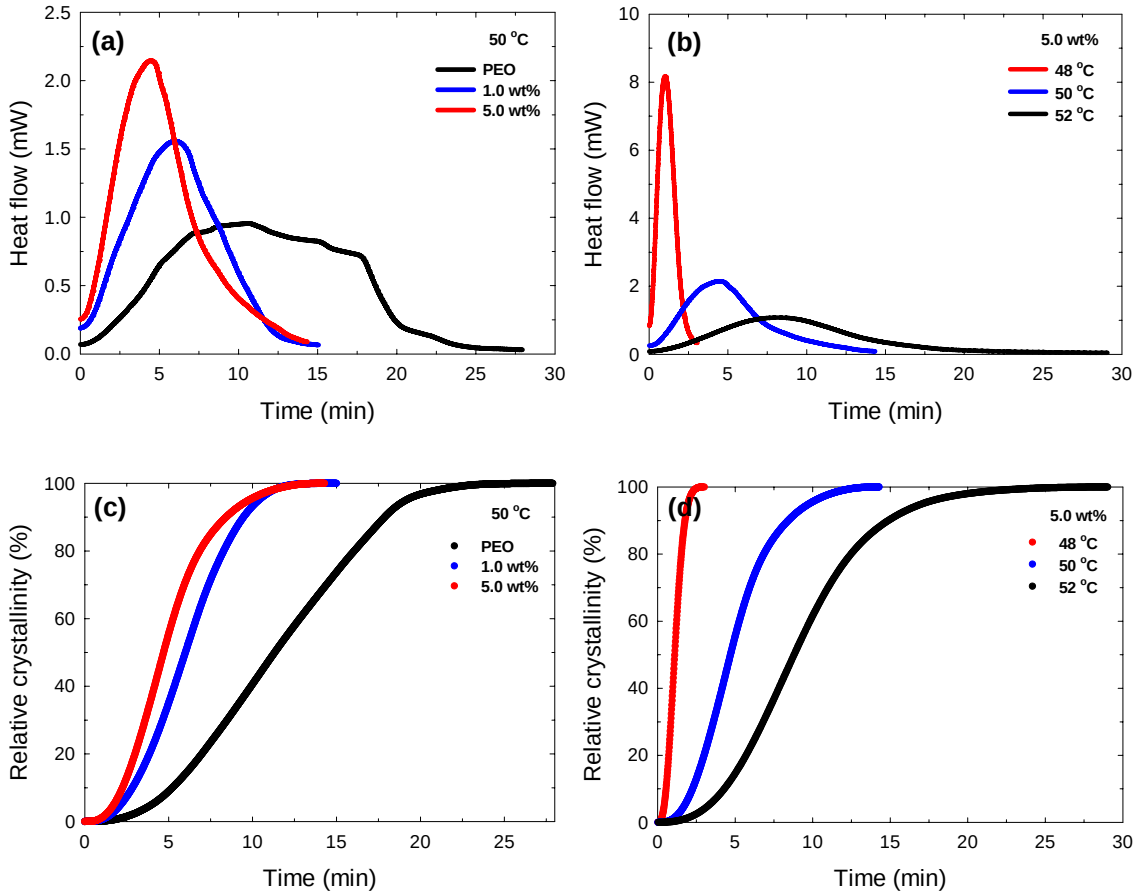

Figure 4.6. Heat flow as a function of time (a) at crystallization temperature, 50 °C and (b) at different crystallization temperatures with 5.0 wt%; Relative crystallinity *vs.* time (c) at crystallization temperature, 50 °C and (d) at different crystallization temperatures with 5.0 wt%.

Crystallization kinetics was modeled with the Avrami equation for isothermal crystallization:

$$X_t = 1 - \exp(-kt^n)$$

Where X_t is the relative crystallinity, n is the Avrami exponent, k is the kinetic rate constant, and t is the crystallization time.[192] By plotting $\ln[-\ln(1 - X_t)]$ vs ln$t$, the n and ln$k$ values could be obtained from the slope and intercept, respectively.

The crystallization half-time, $t_{1/2}$, is defined as the time at which the extent of crystallization is 50%, and is determined from the following relationship:

$$t_{1/2} = \left(\frac{\ln 2}{k}\right)^{1/n}$$

Usually, the rate of crystallization, G, is described as the reciprocal of $t_{1/2}$, that is $G = \tau_{1/2} = 1/t_{1/2}$. The necessary time for maximum crystallization, t_{max}, could be derived from Avrami equation,[193]

$$t_{\max} = \left(\frac{n-1}{nk}\right)^{1/n}$$

The Avrami parameters for the samples that were investigated at different isothermal crystallization temperature (T_c) are listed in Table 4.2.

Table 4.2. Isothermal crystallization kinetic parameters analyzed by Avrami equation for PEO, 1.0 wt%, and 5.0 wt% samples.

Sample	T_c (℃)	n	k (min^{-n})	$t_{1/2}$ (min)	t_{max} (min)
PEO	48	2.39 ± 0.13	0.0151 ± 0.0013	5.67 ± 0.12	5.23 ± 0.29
	50	2.45 ± 0.11	0.0014 ± 0.0001	14.63 ± 1.63	13.74 ± 1.68
	52	2.71 ± 0.11	9.68×10^{-6} ± 1.2 x 10^{-7}	69.29 ± 1.98	66.78 ± 2.47
1.0 wt%	48	2.64 ± 0.21	0.0837 ± 0.0016	2.23 ± 0.02	2.14 ± 0.06
	50	2.66 ± 0.07	0.0056 ± 0.0008	6.15 ± 0.22	5.91 ± 0.25
	52	2.36 ± 0.32	0.0007 ± 0.00005	21.04 ± 0.10	19.30 ± 1.15
5.0 wt%	48	2.69 ± 0.14	0.4699 ± 0.058	1.16 ±0.08	1.12 ± 0.09
	50	2.31 ± 0.16	0.0209 ± 0.0006	4.60 ± 0.17	4.21 ± 0.18
	52	2.53 ± 0.02	0.0026 ± 0.0002	9.16 ± 0.45	8.67 ± 0.41

All the values for the Avrami exponent, n, are between 2.5 and 3, indicating a spherulitic growth.[194, 195] Figure 4.7 (a) shows the rate of crystallization (G), which represents the overall crystallization rate including both nucleation and growth, as a function of the m-CNTs content for three isothermal crystallization temperatures of 48,

50, and 52 ^{o}C. In all cases, the crystallization rate increased with increasing mass loading of m-CNTs. Figure 4.7 (b) shows the dependence of the overall crystallization rate on the isothermal crystallization temperature of the composite films. In all cases, the overall crystallization rate decreased as T_c increased.

These results are quite different than those of Jin et al., who have found that the crystallization rate decreased with increasing extent of incorporation of functionalized MWNT.[70] Conversely, Priftis et al. studied the extent of crystallization of PEO that occurred when ethylene oxide (EO) was covalently attached to the MWNT and subsequently polymerized to form the MWNT-g-PEO system. This system showed increased crystallization rate when compared with pure PEO, possibly due to the fact that the grafted monomeric units acted as nucleating agents during polymerization.[72] Similarly, in this system, the magnetic nanoparticles are tethered to the surface of the CNTs, and hence they could act as nucleation agents as well, fact which would result in faster crystallization rates. Another measure of the overall crystallization rate is the crystallization rate constant, *k*. Figures 4.7 (c) and (d) also show that *k* increased with both the increase of the mass loading of m-CNTs and the decrease of the isothermal crystallization temperature, in a manner analogous to the results obtained for the behavior of the rate of crystallization.

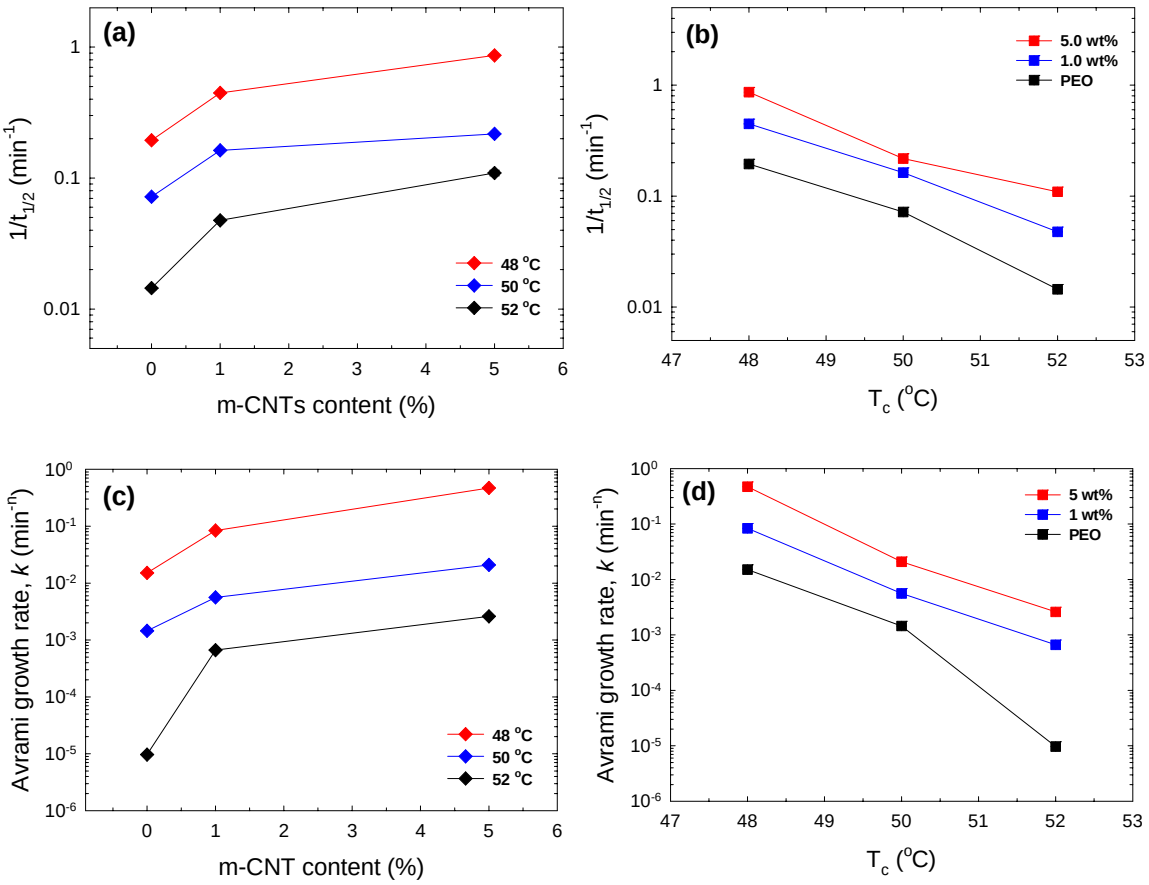

Figure 4.7. The rate of crystallization time as a function of (a) m-CNTs content for different crystallization temperatures and (b) crystallization temperatures for different m-CNTs content; Avrami overall crystallization rate constant, k, as a function of (c) m-CNTs content for different crystallization temperatures and (d) crystallization temperatures for different m-CNTs content.

Finally, the crystallization process of the composite films is assumed to be thermally activated. The crystallization rate parameter, k, can be approximately described by the following Arrhenius equation:

$$k^{1/n} = k_0 \exp(-\Delta E / RT_c)$$

where k_o is the temperature independent pre-exponential factor, R is the gas constant, and ΔE is the crystallization activation energy.[196, 197] By plotting $1/n(\ln k)$ vs. $1/T_c$, a straight line can be generated as shown in Figure 4.8. The values of the

crystallization activation energies are -12.9 kJ/mol, -11.1 kJ/mol, and -10.8 kJ/mol in the case of pure PEO, PEO loaded with 1 wt% m-CNTs, and PEO loaded with 5 wt% CNTs, respectively. The activation energy decreased with the increase of the m-CNTs content, fact which is in good agreement with the dependence of the rate of crystallization on m-CNTs content, i.e. the higher the m-CNTs content, the faster the crystallization rate, and the lower the required crystallization activation energy.

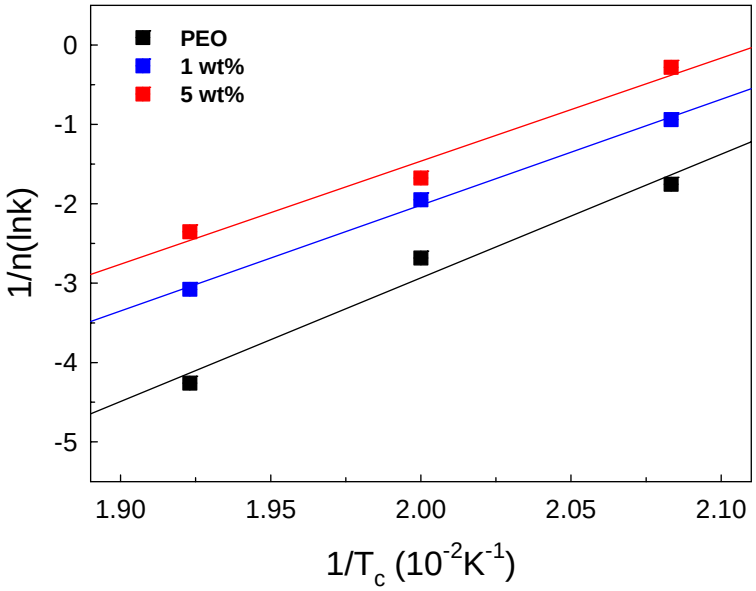

Figure 4.8. Plot of (1/n)lnk vs. $1/T_c$ from the Arrhenius method for isothermal crystallization activation energy of composite films.

4.3.4 Anisotropic Conductivity of the PEO-m-CNTs Composite Films

The electric conductivities of the PEO-m-CNTs composite films were measured at a series of different frequencies, from 0.1 Hz to 1 MHz. Figure 4.9 (a) shows various conductivities of a series of PEO-m-CNTs composite films containing various mass loadings (weight percent) of m-CNTs in the polymer matrix.

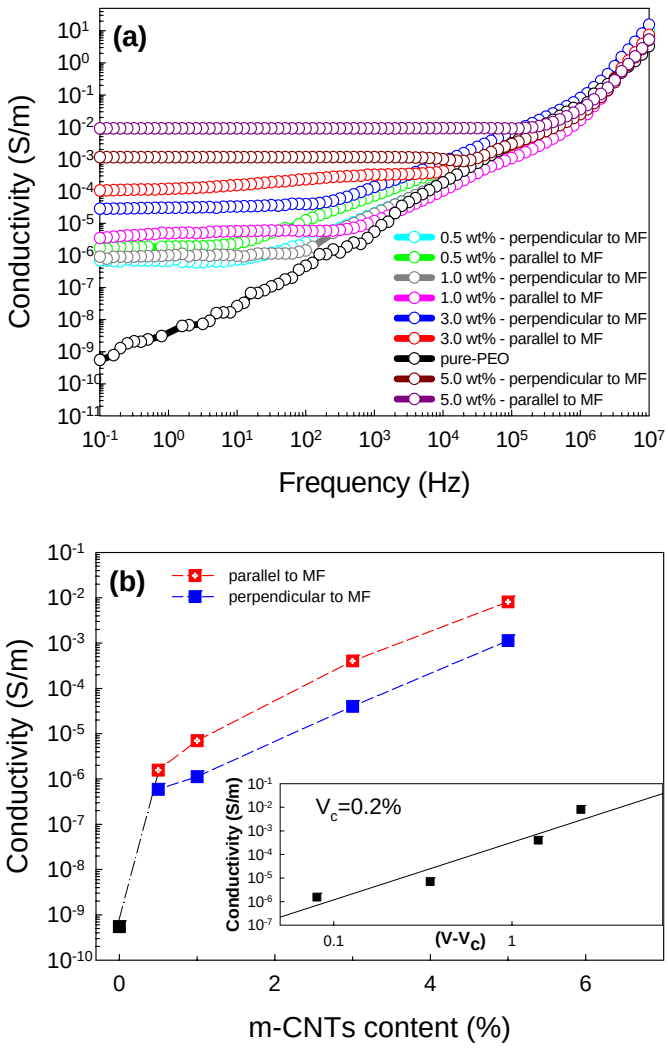

Figure 4.9. (a) The conductivity of PEO-m-CNTs composite films as a function of frequency for different m-CNTs content as measured in the direction parallel to the magnetic field and perpendicular to the magnetic field; (b) The conductivity of PEO-m-CNTs composites as a function of different m-CNTs content measured in the direction parallel to the magnetic field and perpendicular to it. Inset shows the percolation equation fit to the experimental conductivity data obtained parallel to the direction of the magnetic field.

Conductivities increased with increasing mass loading of m-CNTs in PEO when applying a low magnetic field strength (< 0.3 T). The conductivities were measured along the general direction of orientation of the m-CNTs, which corresponds to the direction that is parallel to the original direction of the applied magnetic field (parallel), or

perpendicular to the direction of the m-CNTs orientation, which corresponds to the direction that is perpendicular to the applied magnetic field (perpendicular). The conductivity data are summarized in Table 4.3.

Table 4.3. The conductivities of PEO-m-CNTs composite films in the directions that were parallel and perpendicular to the externally-applied magnetic field as a function of m-CNTs content.

m-CNT loading (wt%)	Conductivity (S/m)		Conductivity ratio of parallel and perpendicular
	Parallel	Perpendicular	
5.0	$8.1 \times 10^{-3} \pm 1.1 \times 10^{-3}$	$1.1 \times 10^{-3} \pm 2.9 \times 10^{-4}$	7.4
3.0	$4.0 \times 10^{-4} \pm 5.0 \times 10^{-5}$	$4.0 \times 10^{-5} \pm 1.5 \times 10^{-6}$	10
1.0	$7.0 \times 10^{-6} \pm 3.1 \times 10^{-7}$	$1.1 \times 10^{-6} \pm 2.3 \times 10^{-7}$	6.4
0.5	$1.6 \times 10^{-6} \pm 2.0 \times 10^{-7}$	$5.9 \times 10^{-7} \pm 1.2 \times 10^{-8}$	2.7

It should be noted that the conductivity of a sample containing 5.0 wt% m-CNTs measured parallel to the magnetic field showed a fourfold increase compared to that of a sample containing 0.5 wt% m-CNTs, measured parallel to the magnetic field as well. Moreover, for the samples having the same mass loading of m-CNTs, the conductivity that was measured in the direction of the m-CNTs alignment (parallel to the magnetic field) was higher in comparison to the conductivity that was measured perpendicular to the m-CNTs alignment (perpendicular to the magnetic field). This was most likely due to the particular features of the aligned m-CNTs in the polymer matrix most notable the formation of an interconnected m-CNTs network, that effectively facilitates electron flow.

Percolation theory has been a very useful tool in understanding certain materials properties, particularly when applied to particulate fillers embedded in polymeric systems. In general, a polymer-based composite undergoes a transition from a behavior as an insulating material to a behavior as a conducting materials when the volume fraction of

its conducting filler phase reaches a critical threshold, v_c. Indeed, for the ordered dispersion of CNTs in a polymer matrix, the electrical conductivity of the composite, σ_c, having a filler volume fraction v, is governed by the percolation law.

$$\sigma_c \propto (v - v_c)^t$$

Where σ_c is the composite conductivity, v is the volume fraction of m-CNTs in the composite, v_c is the critical volume fraction, and t is the critical exponent. It is assumed that the density of m-CNTs is the same as that of unmodified CNTs (2.1 g/cm^3), since the nanoparticles tethered onto the surface of CNTs contribute to both enhanced volume and increased mass while preserving the same ratio of the two. Figure 4.9 (b) shows the variation of the conductivities extracted from the plateau regions in the low frequency range shown in Figure 4.9 (a), in which the inset illustrates the plot of σ_c as a function of v-v_c for the measurements performed parallel to the magnetic field. The linear fit to the data generated a straight line with v_c = 0.2 vol% (corresponding to 0.4 wt%). In the previous Chapter,[181] the alignment of m-CNTs at high mass loading (i.e. 3.0 wt%) in epoxy matrices was not as effective as that of the less concentrated samples, mainly due to higher solution viscosity. Conversely, the alignment of m-CNTs in PEO could be achieved at even higher mass loading (i.e. 5.0 wt%) of m-CNTs, resulting in a more pronounced exhibition of anisotropic electrical properties, as shown in Figure 4.9 and Table 4.3 (see the results of the ratio of the conductivities measured parallel and perpendicular to the magnetic field).

4.3.5 Mechanical Properties of the PEO-m-CNTs Composite Films

The mechanical properties of the PEO-m-CNTs composite films were found to be dependent on the amount of loaded m-CNTs as well as the aligned features of the m-CNTs phase in the PEO matrix. Figures 4.10 (a) and (b) show stress *vs.* strain curves and mechanical properties as a function of m-CNTs mass loading for isotropic (i.e. not aligned) samples. Both tensile modulus and tensile strength increased with increasing mass loading of m-CNTs in PEO. In the previous section regarding crystallinity of composite films, it was discussed the fact that the crystallinity decreased with increasing mass loading of m-CNTs due to the interactions between the m-CNTs and the polymer chains. In nanocomposites with non-covalent interactions, strong attractions could inhibit crystallinity through constraining polymer molecules at the interface.[182-184] Therefore, it can be drawn a conclusion that the magnetic nanoparticles on the surface of CNTs could interact with the PEO chains, resulting in the decrease in the crystallinity of the system. Furthermore, the tensile modulus and tensile strength for the anisotropic (i.e. aligned) samples were compared and analyzed. Figures 4.10 (c) and (d) show the measurements of mechanical properties of all the samples, with the results of measurements summarized in Table 4.4. The tensile moduli measured in the samples in which the alignment of m-CNTs is parallel to the applied stress were higher than those measured in isotropic samples. As shown in Figure 4.3, the alignment of the m-CNTs parallel to the direction of magnetic field is most likely facilitated by the intimate contacts between the magnetic nanoparticles near the ends of the CNTs, resulting in dipolar interactions when subjected to an external magnetic field, thus promoting the formation of aligned features coupled with long range order.[181] Therefore, m-CNTs could generate a higher aspect ratio phase that would enhance the effective load transfer from the matrix to the m-CNTs.[198, 199]

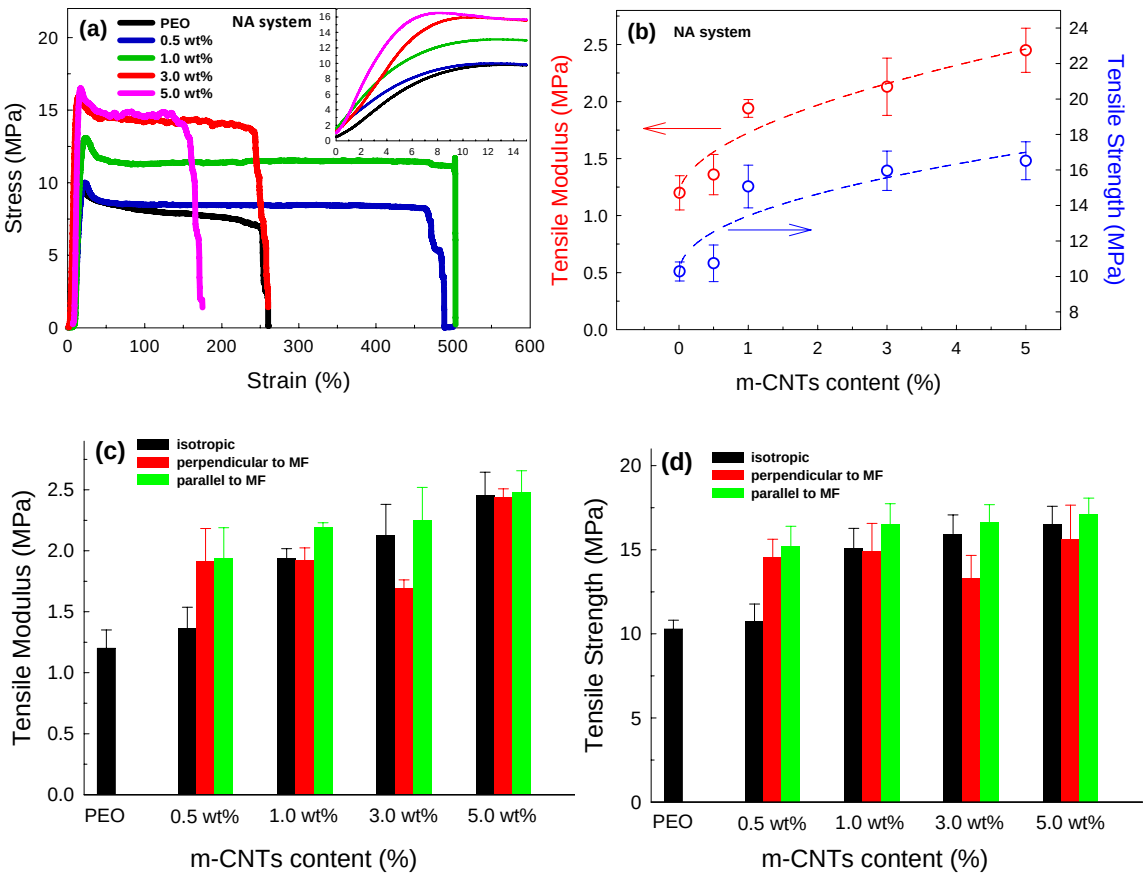

Figure 4.10. (a) The stress vs. strain graph of isotropic (not-aligned) samples; (b) The tensile modulus and tensile strength as a function of m-CNTs content for isotropic samples; (c) The tensile modulus and (d) The tensile strength as a function of m-CNTs for isotropic and anisotropic samples.

When the stress is applied in the direction that is perpendicular to the direction of alignment of the m-CNTs, the tensile modulus increased with m-CNTs loading up to 1.0 wt%, but decreased with higher loadings. This is mainly due to the aggregation of m-CNTs, leading to loss of interfacial area between filler and matrix, resulting in a reduction in the efficiency of the load transfer mechanism. At high mass loadings (i.e. 5.0 wt%) of m-CNTs, the tensile modulus of isotropic and anisotropic samples is similar, fact which demonstrates that at higher mass loadings, the aligned features were not as significant as they were in the less concentrated samples. The results concerning the

tensile strength properties of the composites exhibit similar behavior as those observed regarding the tensile moduli.

Table 4.4. The tensile modulus and tensile strength of isotropic (i.e. not-aligned) and anisotropic (i.e. aligned) samples aligned in the directions that were parallel and perpendicular to the applied stress as a function of m-CNTs content.

		PEO	0.5 wt%	1.0 wt%	3.0 wt%	5.0 wt%
Tensile Modulus (MPa)	NA[a]	1.20 ± 0.2	1.36 ± 0.2	1.94 ± 0.1	2.13 ± 0.3	2.45 ± 0.2
	V[b]	-	1.91 ± 0.3	1.92 ± 0.1	1.69 ± 0.1	2.44 ± 0.1
	A[c]	-	1.94 ± 0.3	2.19 ± 0.1	2.25 ± 0.3	2.48 ± 0.2
Tensile Strength (MPa)	NA	10.3 ±0.5	10.7 ± 1.0	15.1 ± 1.2	16.0 ± 1.1	16.5 ± 1.1
	V	-	14.6 ± 1.0	15.0 ± 1.6	13.3 ± 1.4	15.6 ± 2.0
	A	-	15.2 ± 1.2	16.5 ± 1.2	16.6 ± 1.1	17.1 ± 1.0

[a] Isotropic (i.e. not-aligned) samples; [b] Samples aligned in the direction that was perpendicular to the applied stress; [c] Samples aligned in the direction that was parallel to the applied stress

4.4 Conclusions

The modified sol-gel technique for developing magnetic carbon nanotubes was successfully utilized, where individual and homogeneously-distributed iron oxide magnetic nanoparticles (maghemite; γ-Fe_2O_3) were synthesized and tethered onto the surface of CNTs. When applying a low magnetic field (< 0.3 T), m-CNTs were aligned parallel to the magnetic field even at higher mass loading of m-CNTs in PEO. The crystallinities of both aligned and unaligned samples at the same m-CNTs content in the PEO matrix were similar, since the PEO chains were randomly absorbed on the surface of the nanotubes rather than following the preferential orientation of the m-CNTs. The isothermal crystallization studies indicate that crystallization kinetics is accelerated by the nucleating action of the magnetic nanoparticles tethered to the surface of CNTs, i.e. the rate of crystallization increased with the increase in the m-CNTs content and with the decrease of the crystallization temperature. Furthermore, it was noted that the crystal

structure of PEO in all of the samples was spherulitic-shaped, fact which was confirmed by applying the Avrami equation to the isothermal crystallization process. The conductivity measurements performed on PEO-m-CNTs composite films having a low percolation threshold (~ 0.4 – 0.5 wt% m-CNTs loading) showed that the conductivity of the samples increased with increasing m-CNTs content. Moreover, the conductivity measured in the direction parallel to the magnetic field was higher than that measured in the direction perpendicular to it. The tensile modulus and tensile strength increased with increasing m-CNTs content due to the non-covalent strong interactions between m-CNTs and polymer chains, resulting in the reduction of crystallinity of the PEO in composites. Moreover, both tensile modulus and tensile strength in the samples in which the alignment of the m-CNTs was parallel to the applied stress were higher than those in the samples in which the alignment of the m-CNTs was perpendicular to the applied stress. In summary, anisotropic materials with enhanced physical properties could be achieved by developing PEO-m-CNTs composite systems with an aligned filler phase.

CHAPTER 5

SYNTEHSIS AND ELECTROCHEMICAL PERFORMANCE OF REDUCED GRAPHENE OXIDE/MAGHEMITE COMPOSITE AS AN ANODE MATERIAL FOR LITHIUM ION BATTERIES

5.1 Introduction

This chapter addresses the electrochemical performance of developed anode materials using graphene and iron oxide precursor for lithium ion batteries. Reduced graphene oxide (rGO) tethered with maghemite (γ-Fe_2O_3) was synthesized using a novel modified sol-gel process, where sodium dodecylbenzenesulfonate (NaDDBS) was introduced into the suspension in order to prevent the formation of an iron oxide 3D network, and nearly monodispersed and homogeneously distributed γ-Fe_2O_3 magnetic nanoparticles could be obtained on the surface of graphene sheets. Due to the thermal process, reducing agent for the reduction of the graphene oxide was not needed. Their morphology and structure were investigated using various characterization techniques. These as-prepared rGO/Fe_2O_3 composites were utilized as anodes for half lithium ion cells. The 40 wt%-rGO/Fe_2O_3 composite exhibited high reversible capacity of 670 mA h g^{-1} at current density of 500 mA g^{-1} and good stability for over 100 cycles, in contrast with that of the pure-Fe_2O_3 nanoparticles which demonstrated rapid degradation to 224 mA h g^{-1} after 50 cycles. Furthermore, the composite showed good rate capability of 270 mA h g^{-1} at 10 C (~10,000 mA g^{-1}). These characteristics could be mainly attributed to both the use of an effective binder, poly(acrylic acid) (PAA), and the specific hybrid

structures that prevent agglomeration of nanoparticles as well as provide buffering spaces against volume changes of nanoparticles during continuous intercalation/deintercalation of Li ions.

5.2 Experimental

5.2.1 Preparation of the Reduced Graphene Oxide (rGO)-Fe_2O_3 Hybrid Structure

Graphtie oxide (GO) was synthesized from natural graphite flakes (325 mesh, 99.8% metal basis) purchased from Alfa Aesar by applying a modified Hummers method. In brief, graphite powder (2g) and sodium nitrate ($NaNO_3$, 1g) were mixed in concentrated sulfuric acid (H_2SO_4, 70 mL) under stirring and cooled by using an ice bath. Under vigorous stirring, potassium permanganate ($KMnO_4$, 6g) was added gradually with keeping the temperature of the mixture below 20 °C. Successively, the mixture was intensely stirred at 35 ± 3 °C for 30 min, resulting in the formation of a thick paste. Next, 150 mL of DI water was slowly added, and the solution was stirred for 15 min at 90 ± 3 °C. After dilution with 240 mL of DI water, 5 mL of hydrogen peroxide (H_2O_2, 30%) was added to the mixture and stirred for 2 hrs, turning the color of the solution from the dark brown to brilliant yellow along with bubbling. After that, the mixture was filtered and washed with 250 mL of hydrochloric acid (HCl, 10%), followed by DI water until the pH of the supernatant was neutral. Finally, the resulting solid was dried in a vacuum.

Reduced graphene oxide (rGO)-Fe_2O_3 hybrid materials were synthesized by applying a novel synthesis technique, modified sol-gel process. The synthesis of rGO-Fe_2O_3 was performed by first adding 0.65 g $Fe(NO_3)_3{\cdot}9H_2O$ to 20 ml of DI water and stirring until the $Fe(NO_3)_3{\cdot}9H_2O$ was dissolved completely. Subsequently, GO was added to the solution with a mass ratio of 4:1 ($Fe(NO_3)_3{\cdot}9H_2O$: GO mass ratio of 4:1), stirred,

and ultra-sonicated for 3 hrs. For the preparation of sample with 8:1 mass ratio, 1.3 g of $Fe(NO_3)_3 \cdot 9H_2O$ was added. Twenty ml of 1.2 mM of NaDDBS (sodium dodecyl benzene sulfonate) were added to the solution and stirred for 30 min. Then, 1.2 ml of propylene oxide was added as a gelation agent and stirred for 30 min. The mixture was then placed in a Fisher Scientific iso-temperature oven for drying for 3 days at 100 °C. The resulting powder products were washed with DI water and ethanol several times and dried at 50 °C. The calcination of these powders was performed in a furnace under argon atmosphere at 500 °C for 2 hrs. The schematic illustration is shown in Figure 5.1.

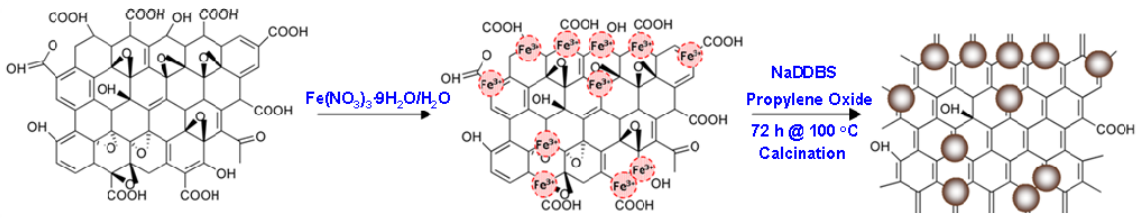

Figure 5.1. Schematic representation of overall strategy for producing rGO-Fe_2O_3 hybrid structures.

For the preparation of pure Fe_2O_3 nanoparticles, the synthesis was the same as previously conducted process except GO. The nanoparticle size of pure Fe_2O_3 was approximately 30 nm as shown in Figure 5.2.

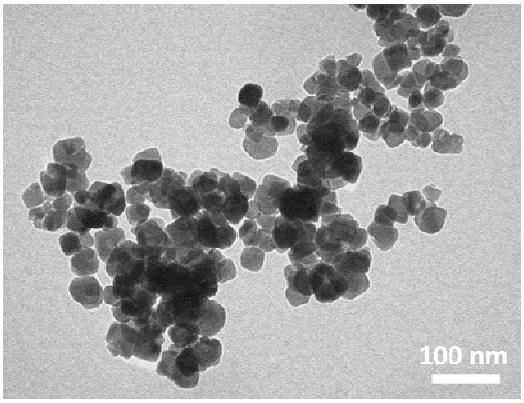

Figure 5.2. Fe_2O_3 magnetic nanoparticles synthesized with same procedure just without graphene oxide.

5.2.2 Materials Characterization

X-ray diffraction (XRD) measurements were performed with an X'pert Pro Alpha-1 (wavelength of 1.54 Å). XRD peaks were collected from $2\theta = 8°$ to 70° with a step size of 0.02°. The morphology of as-prepared samples was characterized using SEM (LEO 1530). TEM samples were prepared by placing a droplet of solution onto a TEM grid. These samples were analyzed using a Hitachi HF2000, 200 kV transmission electron microscopy. XPS scans of powder samples were taken using a Surface Science Laboratories SSX-100 ESCA spectrometer using monochromatic Al Kα radiation (1486.6 eV). Thermal gravimetric analysis (TGA) using a Q50, TA Instrument, was used with a heating rate of 10 °C min^{-1} from room temperature to 800 °C under both nitrogen and air atmosphere. N_2 physisorption (Micromeritics TriStar II 3020) at -196 °C allowed for the determination of the specific surface area of the as-prepared materials. Each sample was degassed in N_2 gas at 100 °C and 300 °C for at least 30 min and 8 hrs, respectively, prior to the measurements. The Brunauer-Emmett-Teller method was used to calculate the surface area.

5.2.3 Electrochemical Measurements

Electrodes were prepared by mixing rGO-Fe_2O_3 nanocomposites, Pure black®, polyacrylic acid (M_w: 450 kDa) with the weight ratio of 85: 5: 10 in water to form a slurry. As-prepared slurry was cast on a 18 μm Cu foil (Fukuda, Japan), dried in air at room temperature first, and then dried in vacuum at 70 °C overnight. The commercial electrolyte consists of 1 M $LiPF_6$ salt in ethylene carbonate-diethyl carbonate-dimethyl carbonate mixture (EC:DEC:DMC = 1:1:1 vol%) (Novolyte Technologies, USA). 2.5 wt% of vinylene carbonate (VC; Alfa Aesar, USA) was added into the electrolyte solution. Lithium metal foil (0.9 mm thick, Alfa Aeasr, USA) was used as a reference electrode. 2016 type coin cells were used for electrochemical characterizations and assembled in an argon-filled glove box (<1 ppm H_2O, O_2). The Cu current collector of the working electrode was spot-welded to the coin cell for enhancing electrical contact. A polyethylene-polypropylene-polyethylene (PP/PE/PP) membrane (Celgard 2325) was used as a separator. Galvanostatic charge-discharge cycling was performed on an Arbin SB2000 (Arbin Instrument, USA) in the range of 0.01-3.0 V. Cyclic voltammetry in the potential window of 0.01 to 3.0 V at a scan rate of 0.014 mV s^{-1} was performed on a Solartron 1480 (Solartron Analytical, USA) multichannel potentiostat.

5.3 Results and Discussion

5.3.1 Characterization of Reduced Graphene Oxide (rGO)-Fe_2O_3 Nanocomposites

Figure 5.3 shows the X-ray diffraction patterns of graphite, graphite oxide (GO), and rGO-Fe_2O_3 hybrid structures. Compared with the pristine graphite, the diffraction peak of GO appears at 10.9° (002) since the AB stacking order is still observed in

graphite oxide with the d-spacing of 0.813 nm.[200] This shows larger value than the d-spacing (0.335nm) of pristine graphite (2θ = 26.6°) due to the intercalated water molecules between layers.[201-203] After being tethered with Fe_2O_3 through a calcination process, graphene oxide was reduced without using additional reduction agents as shown in Figure 5.3 (c).

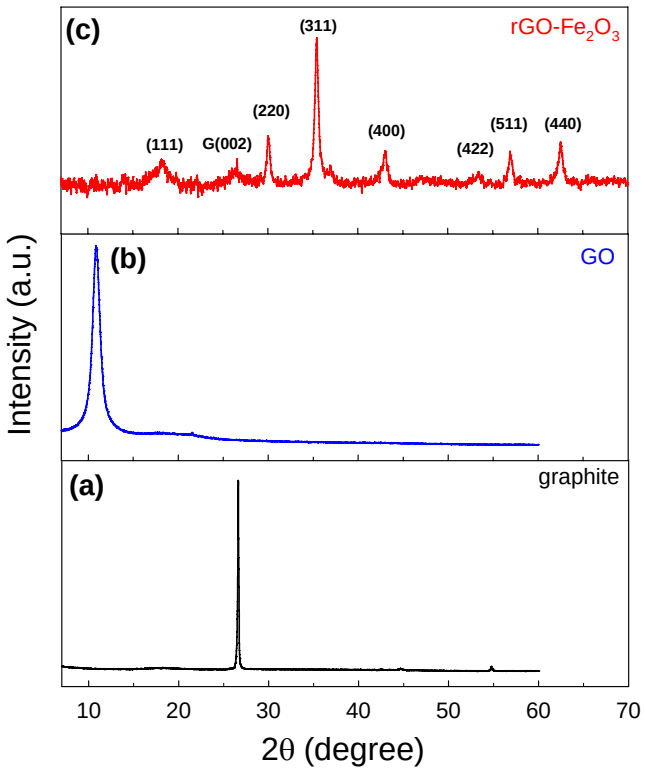

Figure 5.3. X-ray diffraction patterns of (a) Graphite, (b) GO, and (c) rGO-Fe_2O_3 nanocomposites.

The scanning electron microscope (SEM) and high-resolution transmission electron spectroscope (HRTEM) images of GO and rGO-Fe_2O_3 nanocomposites are shown in Figure 5.4. Figure 5.4 (a) shows the TEM image of GO with a curled morphology. Figure 5.4 (b) and (c) show the synthesized rGO-Fe_2O_3 with the mass ratio of 4:1 ($Fe(NO_3)_3 \cdot 9H_2O$: GO mass ratio of 4:1).

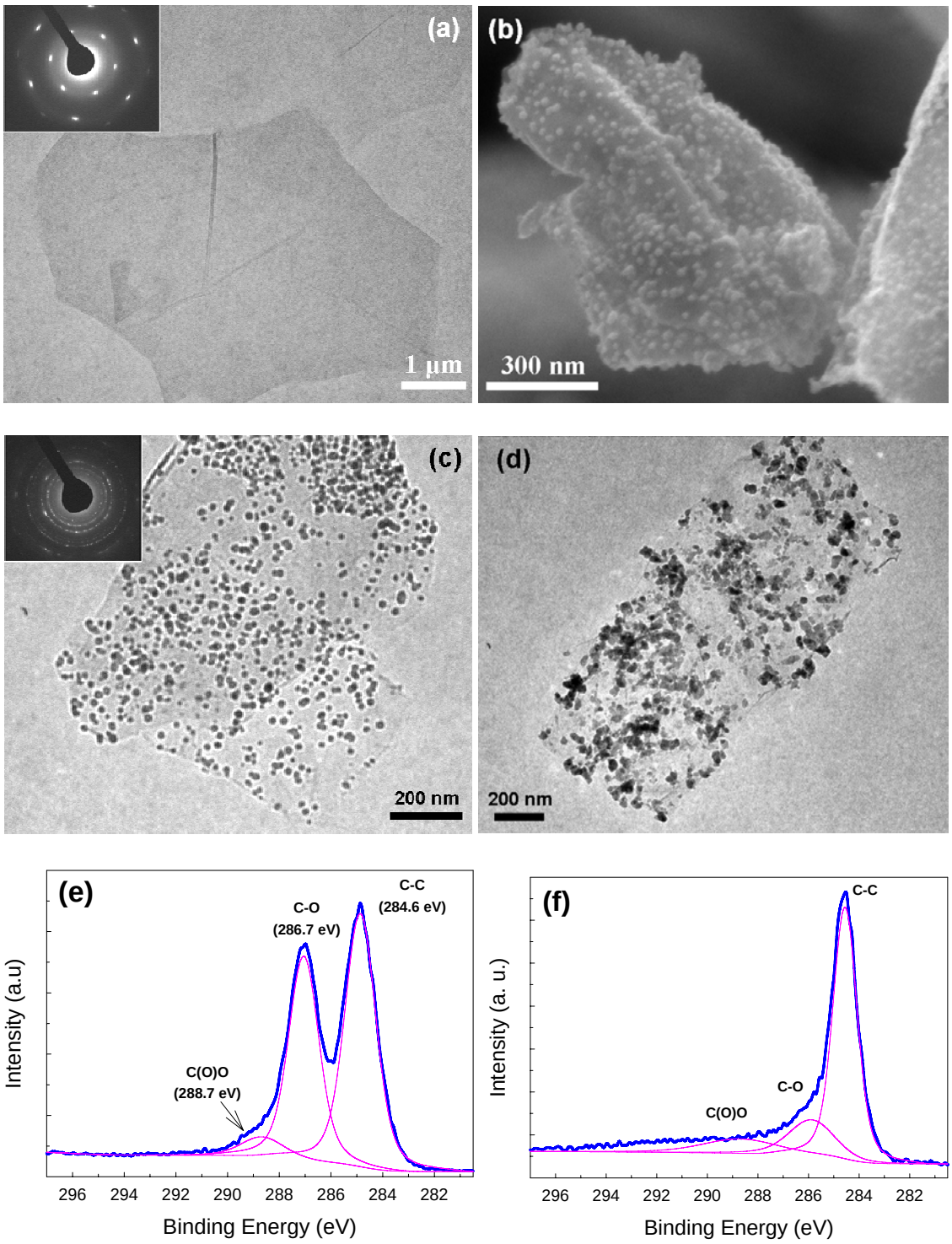

Figure 5.4. (a) TEM image of GO; inset shows the diffraction pattern. (b) SEM image and (c) TEM image of 40 wt%-rGO-Fe_2O_3 hybrid structure. (d) TEM image of 27.5 wt%-rGO-Fe_2O_3 hybrid structure. XPS spectra of C1s of (e) GO and (f) rGO-Fe_2O_3 hybrid materials.

From the TGA result as shown in Figure 5.5, the weight fraction of rGO was 40 wt%. In addition, Figure 5.4 (d) shows the TEM image of rGO-Fe_2O_3 nanocomposite with the mass ratio of 8:1 where the weight fraction of rGO from the TGA result was 27.5%. The surfaces of the rGO sheets were homogeneously tethered with Fe_2O_3 nanoparticles and the nanoparticle sizes of 40 wt% and 27.5 wt%-rGOs were approximately 15 nm and 28 nm, respectively.

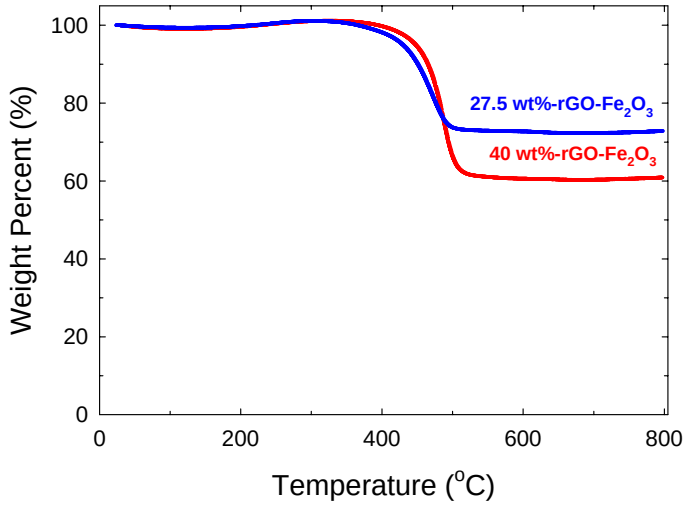

Figure 5.5. TGA curves of rGO-Fe_2O_3 at a heating rate of 10 ^{o}C min^{-1} under an air flow of 20 ml min^{-1}.

By increasing the concentration of iron salts, the size and density of nanoparticles on the graphene sheets increased as well. The insets in Figure 5.4 (a) and (c) show the diffraction patterns, illustrating well-defined crystal structures of graphene and tethered nanoparticles. These as-prepared hybrid composite materials exhibit uneven and rough surface characteristics with large amount of void spaces, which would affect the electrochemical performance when these are used as anode materials for lithium ion batteries. Figure 5.4 (e) and (f) show X-ray photoelectron spectroscopy (XPS) spectra of

GO and rGO-Fe_2O_3 composite materials. The C1s spectrum of GO shows two main peaks centered at 284.6 and 286.7 eV, which correspond to the binding energy of sp^2 C-C bonds and C-O bonds in the epoxy/hydroxyl/carbonyl groups. In comparison to the C1s spectrum of GO, the spectrum of rGO-Fe_2O_3 shows a strong peak corresponding to sp^2 C-C bonds, demonstrating the reduction of functionalized groups containing oxygen during the thermal process.[157, 204]

The porous structure features and Brunauer-Emmett-Teller (BET) specific surface area of 40 wt%-rGO-Fe_2O_3 and 27.5 wt%-rGO-Fe_2O_3 composite materials were investigated by N_2 adsorption/desorption isotherms as shown in Figure 5.6.

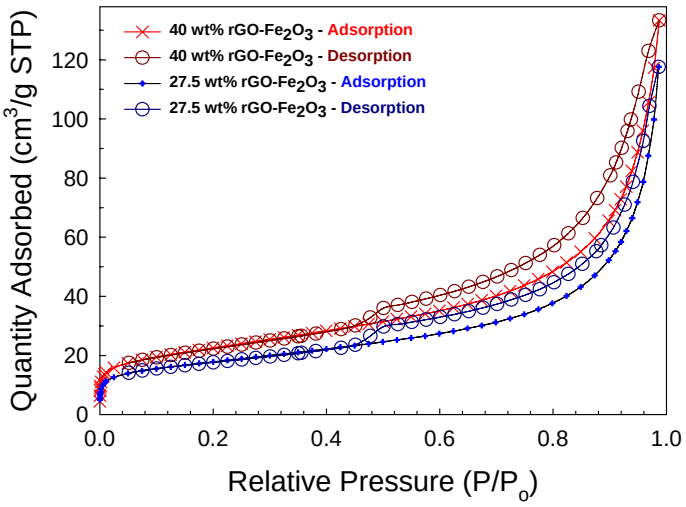

Figure 5.6. N_2 adsorption/desorption isotherms of 40 wt%-rGO-Fe_2O_3 and 27.5 wt%-rGO-Fe_2O_3 hybrid materials.

When comparing BET specific surface area for composite materials, the value of 40 wt%-rGO-Fe_2O_3 is 81 m^2 g^{-1}, which is larger than that (64 m^2 g^{-1}) of 27.5 wt%-rGO-Fe_2O_3 composite material. This is in good agreement with the TEM images. In the case of 40 wt%-rGO-Fe_2O_3, the tethered nanoparticle size was smaller than that of 27.5 wt%-

rGO-Fe_2O_3; thus, the latter exhibits the lower specific surface area. The relatively large specific surface area is beneficial for the electrolyte access, but, unfortunately, increase irreversible capacity losses at the first cycle due to the electrolyte decomposition and solid electrolyte interphase (SEI) formation. The total pore volumes of 40 wt%-rGO-Fe_2O_3 and 27.5 wt%-rGO-Fe_2O_3 composite materials are 0.21 $cm^3\ g^{-1}$ and 0.18 $cm^3\ g^{-1}$, respectively. The nanopores in composite materials could tolerate the volume changes of Fe_2O_3 nanoparticles during intercalation/deintercalation process of lithium ions and may affect the large reversible capacity, good rate performance, and cycling stability.[155, 205, 206]

5.3.2 Electrochemical Performance of rGO-Fe_2O_3 Nanocomposites and Pure-Fe_2O_3 Nanoparticles

The electrochemical properties of the rGO-Fe_2O_3 nanocomposites and the pure-Fe_2O_3 nanoparticles were compared and investigated. Intercalation/deintercalation cycling of Li ions was carried out in the voltage range of 0.01 – 3.0 V. The intercalation/deintercalation curves for as-prepared 40 wt%-rGO-Fe_2O_3 nanocomposite and pure-Fe_2O_3 are shown in Figure 5.7 (a) and (b). The first two intercalation/deintercalation cycles were tested at a current density of 45 mA g^{-1}, and next up to 100^{th} cycle after first two cycles was conducted at a current density of 500 mA g^{-1}. In the first cycle, the intercalation/deintercalation capacities of as-prepared pure-Fe_2O_3 were 1032 mA h g^{-1} and 755 mA h g^{-1}, respectively. However, it fades quickly as shown in Figure 5.7 (b) due to the severe aggragation and high volume changes of Fe_2O_3 nanoparticles during Li^+ insertion/extraction process.[207, 208] Such aggregations combined

with large volume changes may destroy the SEI layer, which, in turn, consumes Li ions and leads to poor cyclic performances.

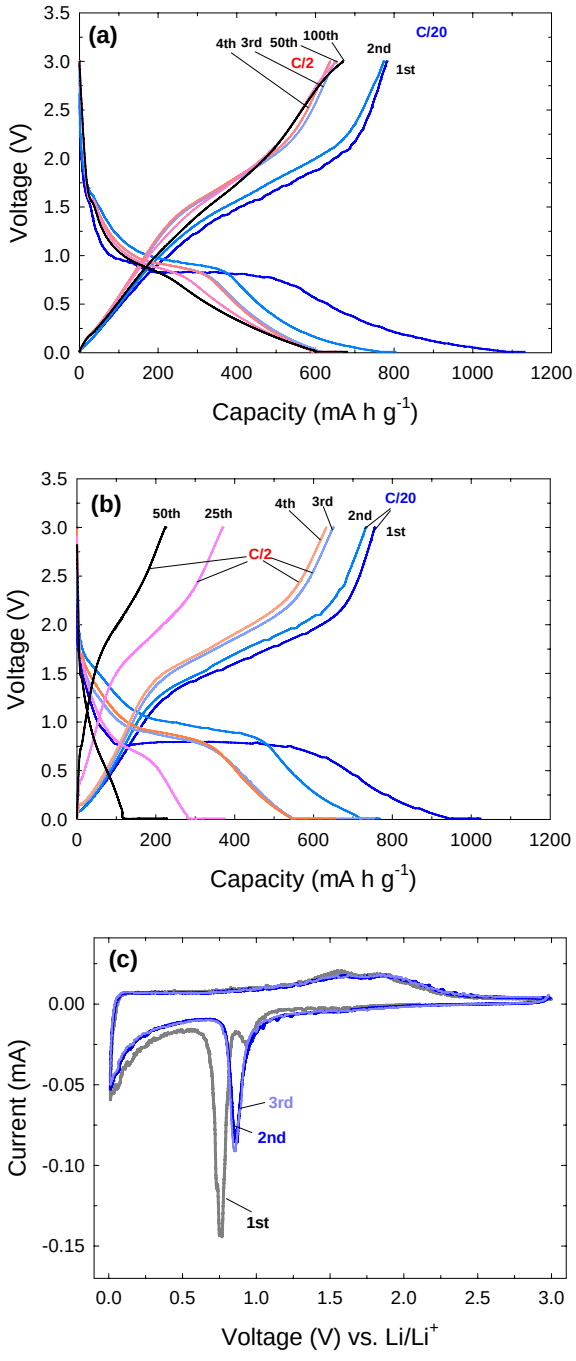

Figure 5.7. Intercalation/deintercalation curves of (a) 40 wt%-rGO-Fe_2O_3 and (b) pure-Fe_2O_3 nanoparticles at current density of 45 mA g^{-1} (0.05 C) and 500 mA g^{-1} (0.5 C). (c) Cyclic voltammogram of 40 wt%-rGO-Fe_2O_3 composite at a scan rate of 0.014 mV s^{-1}.

On the contrary, the first intercalation voltage profile of the rGO-Fe_2O_3 nanocomposite is very similar to that of rGO-Fe_3O_4 nanocomposites reported.[156, 209, 210] The maghemite, γ-Fe_2O_3, is the allotropic form of magnetite, Fe_3O_4. These two iron oxides are crystallographically isomorphous. Thus, it can be expected that this new composite system may show similar tendency. In the first intercalation curve as shown in Figure 5.7 (a), two voltage plateaus at ~0.95 V and ~0.8 V were observed. The voltage plateau at ~0.95 V can be attributed to the irreversible reaction. On the other hand, the plateau at ~0.8 V reflects the reduction of Fe(III) to Fe(0). The deintercalation curve showed a sloping plateau at ~1.6 V due to the reverse reaction. The 40 wt%-rGO-Fe_2O_3 electrode showed an initial discharge capacity of 1133 mA h g^{-1} and charge capacity of 782 mA h g^{-1} in the first cycle; thus, Coulombic efficiency was about 70%. This irreversible capacity observed in the first cycle may be caused by the formation of solid electrolyte interphase (SEI) film, the decomposition of electrolyte, and the conversion of Fe_2O_3 to Fe nanoparticles along with the formation of amorphous Li_2O [140, 148, 153, 155, 211, 212]. It may be also caused by the interaction of Li ions with the vacant spaces in octahedral position of the crystal structure of maghemite[167-169]. During the second cycle, the intercalation capacity decreased to 804 mA h g^{-1}, leading to a much higher Coulombic efficiency of 96.3%. Furthermore, when the current density in the 3rd cycle is increased from 45 mA g^{-1} to 500 mA g^{-1}, the intercalation and deintercalation capacities of the hybrid material were 663 mA h g^{-1} and 649 mA h g^{-1} in 3rd cycle, 649 mA h g^{-1} and 637 mA h g^{-1} in 4th cycle, respectively. The Coulombic efficiencies of those cycles were close to 100%.

To identify all of the electrochemical reactions, cyclic voltammetry (CV) was conducted on the cell with 40 wt%-rGO-Fe_2O_3 at room temperature in the 0.01-3.0 V range and a scan rate of 0.014 mV/s as shown in Figure 5.7 (c). In the first cycle, the peak is observed at ~0.95 V, which can be attributed to the reduction of the irreversible reaction with the electrolyte. The peak observed at ~0.75 V can be ascribed to the lithiation reaction of Fe_2O_3 with Li ions as following:[157, 213]

$$Fe_2O_3 + 6Li^+ + 6e \Leftrightarrow 2Fe + 3Li_2O$$

Meanwhile, two peaks were recorded at about 1.56 and 1.85 V in the anodic process, which correspond to the oxidation of Fe^0 to Fe^{2+} and Fe^{3+} during the anodic process. During the subsequent cycles, the cathodic and anodic peaks are positively shifted, which is attributed to the polarization of the electrode in the first cycle. Moreover, a decrease of the redox peak intensity from the 1st cycle to 2nd cycle implies that the capacity is decreased. However, after first cycling, both the peak current and the integrated area of their anodic peaks are changeless, indicating no capacity loss during the delithiation process.

The intercalation/deintercalation cycling performance of the as-prepared 40 wt%-rGO-Fe_2O_3, 27.5 wt%-rGO/Fe_2O_3, and pure-Fe_2O_3 were evaluated between 0.01 and 3.0 V at 0.05 C (first two cycles) and 0.5 C as shown in Figure 5.8 (a). In the first cycle, the intercalation capacity of the pure-Fe_2O_3 nanoparticle electrode is about 1032 mA h g^{-1}. However, the capacity continuously decreases and reaches 224 mA h g^{-1} after 50 cycles, which is only about 22% of the initial capacity, illustrating poor capacity retention. In the case of hybrid materials, rGO-Fe_2O_3 nanocomposites, the first cycle capacities of both 40 wt%-rGO-Fe_2O_3 and 27.5 wt%-rGO-Fe_2O_3 at current density of 45 mA g^{-1}, were 1132

mA h g^{-1} and 1059 mA h g^{-1}, respectively. After 50^{th} cycle, the capacities at current density of 500 mA g^{-1} were 666 mA h g^{-1} and 575 mA h g^{-1}, respectively, and they still marked 59% and 54% of the initial capacity. Importantly, the 40 wt%-rGO-Fe_2O_3 composite electrode tested at a high current density of 500 mA g^{-1} exhibited excellent cyclic performance, retained 677 mA h g^{-1} capacity, and showed Coulombic efficiency of above 99% as shown in Figure 5.8 (b).

To further investigate the electrochemical performance of the hybrid composite materials and pure-Fe_2O_3 nanoparticles, the rate capability of the samples were conducted as shown in Figure 5.8 (c). In the case of pure-Fe_2O_3 electrode, it showed reasonable capacities from current density, 0.1 C, to 1C. However, at high current density, for example, 2C, 5C, or 10C, its values are very low. When observing the results of as-prepared samples, 40 wt%-rGO-Fe_2O_3 and 27.5 wt%-rGO-Fe_2O_3 composite electrodes, they showed higher capacity than that of pure-Fe_2O_3 nanoparticle electrode. Specifically, in the case of 40 wt%-rGO-Fe_2O_3 composite electrode, it showed better capacity retention about 400 mA h g^{-1}, even at high current density of 5C. These results clearly show that the well-organized flexible intercalated structure plays an important role in improving the electrochemical performance. Fe_2O_3 nanoparticles tethered homogeneously on the graphene sheets result in the dimensional confinement of the Fe_2O_3 nanoparticles, limiting the effect of volume expansion during lithiation due to the enough void spaces between graphene sheets. Furthermore, graphene sheets serve not only as an efficient conducting matrix for maintaining the structural integrity of the electrode during insertion/extraction process of Li ions, but also as an enough enduring agent preventing nanoparticles tethered on graphene sheets from aggregating and

resulting in the release of the stress that arises during the process of Li^+ insertion/extraction.

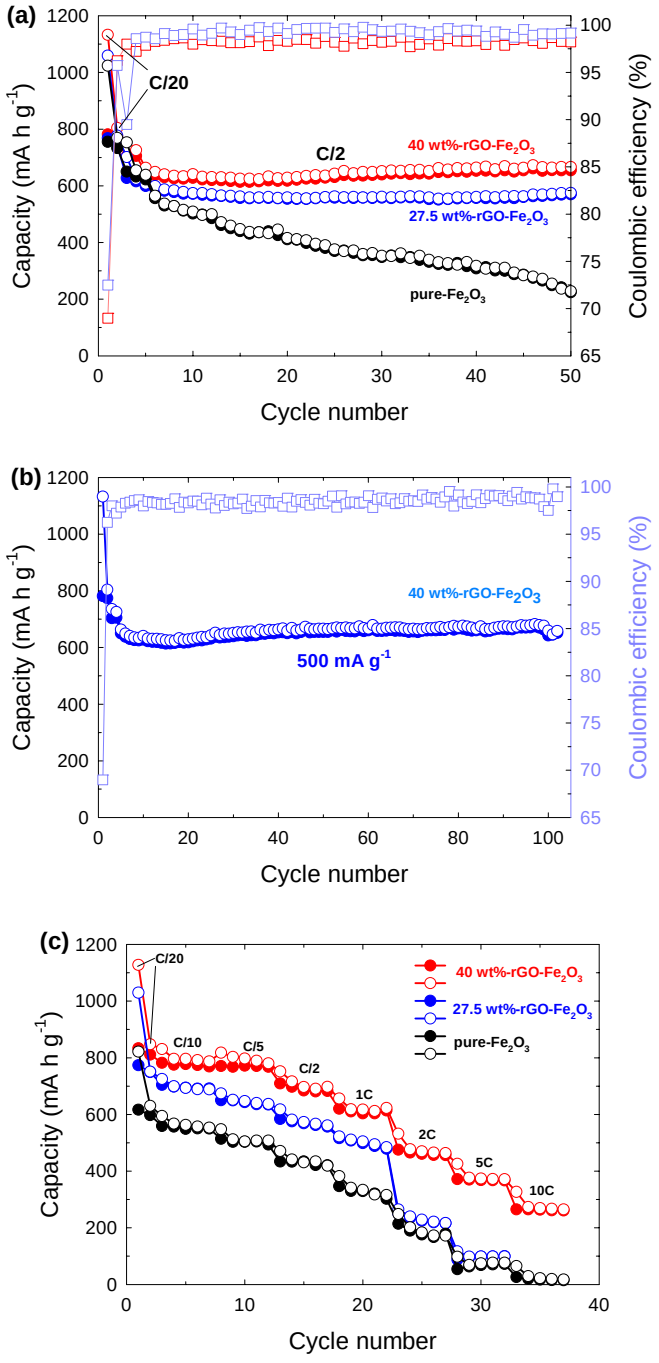

Figure 5.8. (a) Cycle performance of the 40 wt%-rGO-Fe_2O_3, 27.5 wt%-rGO-Fe_2O_3, and pure-Fe_2O_3 electrodes at current rates of 0.05 C (first two cycles) and 0.5 C. (b) Cycle performance of the 40 wt%-rGO-Fe_2O_3 composite at a current density of 500 mA g^{-1} for 100 cycles. (c) The rate performance of the 40 wt%-rGO-Fe_2O_3, 27.5 wt%-rGO-Fe_2O_3, and pure-Fe_2O_3 electrodes at different current densities.

5.4 Conclusions

In summary, modified sol-gel technique for developing reduced graphene oxide/iron oxide hybrid structures was successfully utilized, where individual and homogeneously-distributed maghemite, γ-Fe_2O_3, were synthesized and tethered onto the surface of graphene sheets. The reduced graphene oxide/Fe_2O_3 nanocomposite electrodes exhibited improved reversible capacity, cycle life, and good rate capability. These enhancements can be ascribed to specific hybrid structures, which have significant roles such as the formation of the efficient electrically conductive networks, the inhibition of aggregation of adjacent Fe_2O_3 nanoparticles, and the offer of the buffering spaces against extreme volume changes of Fe_2O_3 nanoparticles during continuous intercalation /deintercalation process of Li ions. In addition, it is supposed that PAA acts as an efficient binder for the battery performance. Reduced graphene oxide/Fe_2O_3 composite electrode maintains a high reversible capacity of 670 mA h g^{-1} up to the 100^{th} cycle even at high current density of 500 mA g^{-1}, showing highly enhanced cycle performance compared to that of pure-Fe_2O_3 nanoparticles. Therefore, graphene sheets tethered with transition metal oxide enhance the overall electrochemical properties as anode materials for lithium ion batteries.

CHAPTER 6

CONCLUSIONS AND RECOMMENDATIONS

6.1 Conclusions

Synthesized hybrid nanomaterials, CNT-maghemite and graphene-maghemite, were utilized to achieve improved physical properties of polymer nanocomposite as well as enhaced electrochemical performance for Li-ion batteries, respectively.

For the preration of functionalized carbon nanotubes and graphene, a simple and novel synthesis method, modified sol-gel process, were successfully applied to both nanomaterials, in which an anionic surfactant, sodium dodecylbenezensulfonate (NaDDBS), was introduced during the synthesis process for the purpose of preventing three-dimensional networks of nanoparticles, which results in gel formation. They formed a self-assembled protective layer around the iron. This coordination has been able to prevent the approach of the propylene oxide molecules within the coordination sphere of the iron centers. Therefore, due to the presence of the NaDDBS molecules, no aggregates of γ-Fe_2O_3 were formed but rather the nanoparticles remained individually isolated both on the surface of carbon nanotubes and on the graphene sheets. Therefore, It can be drawn a conclusion that the modified sol-gel technique could be effectively extended from carbon nanotube system to graphene one.

As-prepared magnetic carbon nanotubes (m-CNTs) could be readily aligned parallel to the direction of magnetic field, even under a low magnetic field, and generated anisotropic features afftected the anisotropic electrical and mechanical properties of the composites. The conductivity measured in the direction parallel to the magnetic field was

higher than that measured in the direction perpendicular to it. In addition, tensile modulus and tensile strength in the samples in which the alignment of the m-CNTs was parallel to the applied stress were higher than those in the samples in which the alignment of the m-CNTs was perpendicular to the applied stress. Therefore, anisotropic materials with enhanced physical properties could be achieved by developing epoxy-m-CNTs and PEO-m-CNTs composite systems with an aligned filler phase.

In the study on graphene/γ-Fe_2O_3 composites, as-prepared composites were used as anode materials for Li-ion batteries. γ-Fe_2O_3 nanoparticles combined with porous graphene sheets exhibit several advantages. (1) The ultrathin graphene sheets can act as a barrier to prevent the aggregation of γ-Fe_2O_3 nanoparticles and enhances the cycle performance. (2) The porous graphene sheets can provide a void space against the volume changes of the γ-Fe_2O_3 nanoparticles during Li-ion insertion/extraction process, which can improve the cycling performance. (3) The graphene sheets itself is an active material for additional Li^+ storage, which is of great benefit to the reversible specific capacity. (4) The γ-Fe_2O_3 nanoparticles are anchored on the surface of the graphene sheets, which could lead to a high rate performance due to the high electronic conductivity of graphene sheets and short path length for Li^+ transport of γ-Fe_2O_3 nanoparticles. Therefore, due to these significant advantages, graphene/γ-Fe_2O_3 composite electrodes showed large reversible specific capacity, long cycling life and good rate capability.

6.2 Recommendations

1. The hybrid nanostructures, carbon nanotubes (CNTs)/iron oxide and reduced graphene oxide (rGO)/iron oxide, have become more and more significant since they play important roles for enhanced polymer nanocomposite systems and improved electrochemical performance of rechargeable battery systems. Therefore, the detailed study on the effect on sizes and shapes of tethered nanoparticles should be investigated.

2. The alignment of carbon nanotubes in polymer matrix is very significant to achieve enhanced anisotropic physical properties. For the purpose of obtaining facile alignment of magnetic carbon nanotubes in epoxy matrix even at high mass loading, as discussed in the Chapter 3, optimaized conditions should be investigated.

3. In the study on PEO-m-CNTs composite films, crystallization kinetics of PEO were investigated. It was drawn a conclusion that there are interactions between polymer chains and nanoparticles tethered on the surface of carbon nanotubes. Regarding this, detailed study on the interactions between PEO and nanoparticles has to be performed because it affects the crystallinity and orientation of PEO in composites as well as physical properties of the composites.

4. Reduced graphene oxide (rGO)/maghemite (γ-Fe_2O_3) nanostructrues were utilized as anode materials for enhancing electrochemical performance for Li-ion batteries. If thin carbon film on iron oxide nanoparticles tethered on the graphene sheets could be coated by carbon deposition process, it could show better rate performance. Therefore, carefully designed experimental steps should be considered for this study.

APPENDIX A

X-RAY DIFFRACTION PATTERN OF HEMATITE

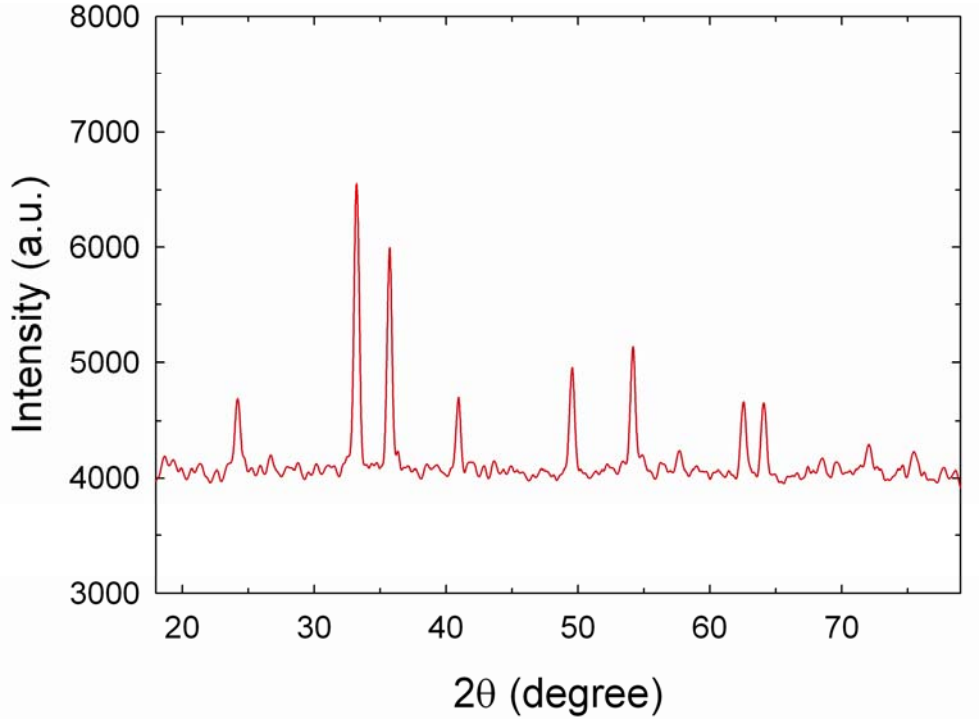

Figure A.1. The XRD spectra of α-Fe_2O_3. When applied the same synthesis method of iron oxide nanoparticles in the absence of carbon nanotube, the structure of iron oxide was that of hematite, i.e. α-Fe_2O_3. Therefore, it can be assumed that the carbon nanotubes affect the nanostructure of iron oxide tethered on their surface.

APPENDIX B

POLYETHYLENE OXIDE-MAGNETIC CARBON NANOTUBES COMPOSITE FILMS

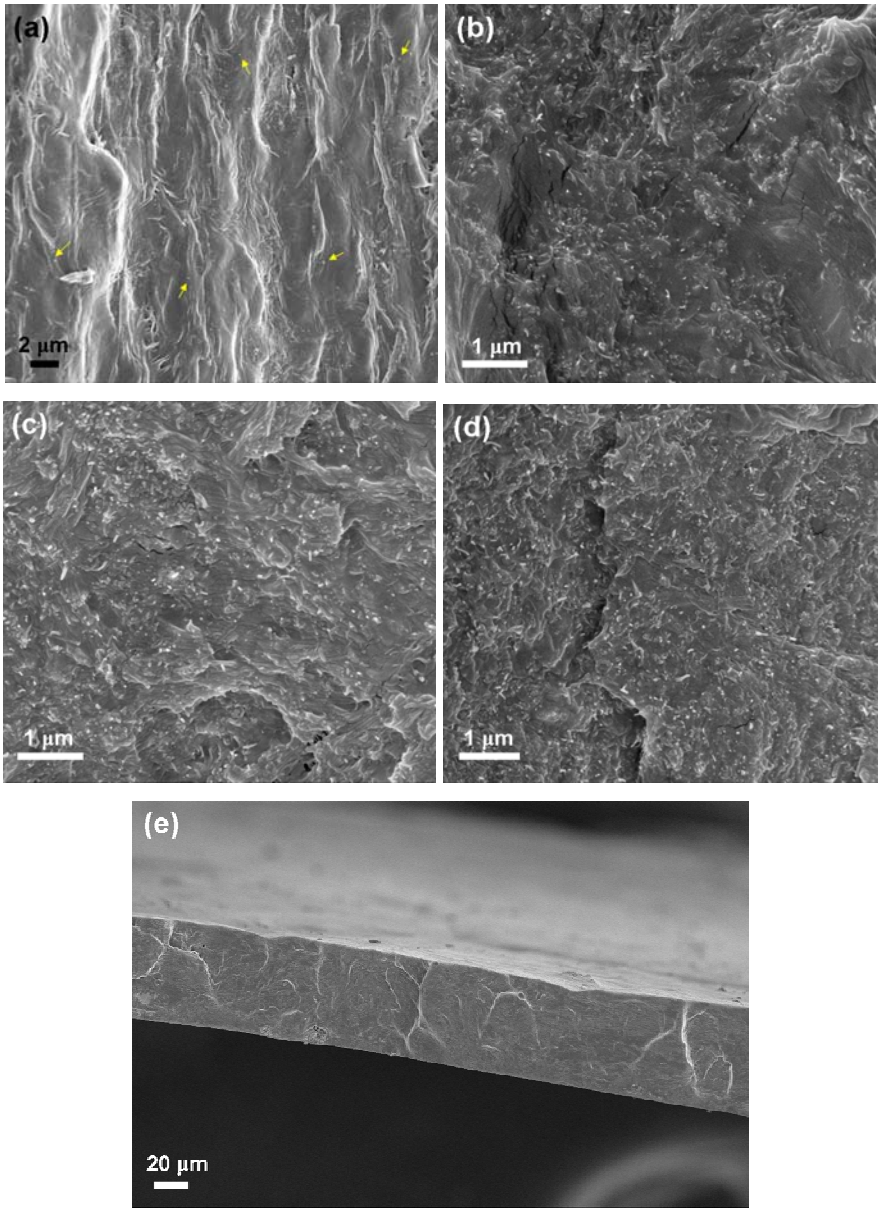

Figure B.1. SEM images of the fracture surfaces of the composite films. (a) 0.5 wt%; (b) 1.0 wt%; (c) 3.0 wt%; (d) 5.0 wt%; (e) low magnification image of cross section of composite films. Yellow arrows in Figure (a) indicate magnetic carbon nanotubes embedded in PEO matrix.

REFERENCES

1. Iijima, S., HELICAL MICROTUBULES OF GRAPHITIC CARBON. *Nature* **1991,** *354* (6348), 56-58.

2. Bernholc, J.; Brabec, C.; Nardelli, M. B.; Maiti, A.; Roland, C.; Yakobson, B. I., Theory of growth and mechanical properties of nanotubes. *Applied Physics a-Materials Science & Processing* **1998,** *67* (1), 39-46.

3. Deheer, W. A.; Bacsa, W. S.; Chatelain, A.; Gerfin, T.; Humphreybaker, R.; Forro, L.; Ugarte, D., ALIGNED CARBON NANOTUBE FILMS - PRODUCTION AND OPTICAL AND ELECTRONIC-PROPERTIES. *Science* **1995,** *268* (5212), 845-847.

4. Huczko, A., Synthesis of aligned carbon nanotubes. *Applied Physics a-Materials Science & Processing* **2002,** *74* (5), 617-638.

5. Wildoer, J. W. G.; Venema, L. C.; Rinzler, A. G.; Smalley, R. E.; Dekker, C., Electronic structure of atomically resolved carbon nanotubes. *Nature* **1998,** *391* (6662), 59-62.

6. Tjong, S. C., Structural and mechanical properties of polymer nanocomposites. *Mater. Sci. Eng. R-Rep.* **2006,** *53* (3-4), 73-197.

7. Robertson, D. H.; Brenner, D. W.; Mintmire, J. W., ENERGETICS OF NANOSCALE GRAPHITIC TUBULES. *Physical Review B* **1992,** *45* (21), 12592-12595.

8. Yu, M. F.; Files, B. S.; Arepalli, S.; Ruoff, R. S., Tensile loading of ropes of single wall carbon nanotubes and their mechanical properties. *Physical Review Letters* **2000,** *84* (24), 5552-5555.

9. Xie, X. L.; Mai, Y. W.; Zhou, X. P., Dispersion and alignment of carbon nanotubes in polymer matrix: A review. *Mater. Sci. Eng. R-Rep.* **2005,** *49* (4), 89-112.

10. Berber, S.; Kwon, Y. K.; Tomanek, D., Unusually high thermal conductivity of carbon nanotubes. *Phys. Rev. Lett.* **2000,** *84* (20), 4613-4616.

11. Hone, J.; Batlogg, B.; Benes, Z.; Johnson, A. T.; Fischer, J. E., Quantized phonon spectrum of single-wall carbon nanotubes. *Science* **2000,** *289* (5485), 1730-1733.

12. Wei, B. Q.; Vajtai, R.; Ajayan, P. M., Reliability and current carrying capacity of carbon nanotubes. *Appl. Phys. Lett.* **2001,** *79* (8), 1172-1174.

13. Thostenson, E. T.; Ren, Z. F.; Chou, T. W., Advances in the science and technology of carbon nanotubes and their composites: a review. *Compos. Sci. Technol.* **2001,** *61* (13), 1899-1912.

14. Sreekumar, T. V.; Liu, T.; Min, B. G.; Guo, H.; Kumar, S.; Hauge, R. H.; Smalley, R. E., Polyacrylonitrile single-walled carbon nanotube composite fibers. *Adv. Mater.* **2004,** *16* (1), 58-+.

15. Anglaret, E.; Righi, A.; Sauvajol, J. L.; Bernier, P.; Vigolo, B.; Poulin, P., Raman resonance and orientational order in fibers of single-wall carbon nanotubes. *Physical Review B* **2002,** *65* (16).

16. Bhattacharyya, A. R.; Sreekumar, T. V.; Liu, T.; Kumar, S.; Ericson, L. M.; Hauge, R. H.; Smalley, R. E., Crystallization and orientation studies in polypropylene/single wall carbon nanotube composite. *Polymer* **2003,** *44* (8), 2373-2377.

17. Liu, T.; Kumar, S., Quantitative characterization of SWNT orientation by polarized Raman spectroscopy. *Chemical Physics Letters* **2003,** *378*, 257-262.

18. Ounaies, Z.; Park, C.; Wise, K. E.; Siochi, E. J.; Harrison, J. S., Electrical properties of single wall carbon nanotube reinforced polyimide composites. *Compos. Sci. Technol.* **2003,** *63* (11), 1637-1646.

19. Dresselhaus, M. S., Dresselhaus, G., Charlier, J. C., Hernandez, E., Philos. Trans. R. Soc. London, A: 2004; Vol. 362, p 2065.

20. Kuang, Q.; Li, S. F.; Xie, Z. X.; Lin, S. C.; Zhang, X. H.; Xie, S. Y.; Huang, R. B.; Zheng, L. S., Controllable fabrication of SnO2-coated nanotubes by chemical vapor multiwalled carbon deposition. *Carbon* **2006,** *44* (7), 1166-1172.

21. Korneva, G.; Ye, H. H.; Gogotsi, Y.; Halverson, D.; Friedman, G.; Bradley, J. C.; Kornev, K. G., Carbon nanotubes loaded with magnetic particles. *Nano Letters* **2005,** *5* (5), 879-884.

22. Qu, L. T.; Dai, L. M.; Osawa, E., Shape/size-control led syntheses of metal nanoparticles for site-selective modification of carbon nanotubes. *Journal of the American Chemical Society* **2006,** *128* (16), 5523-5532.

23. Han, L.; Wu, W.; Kirk, F. L.; Luo, J.; Maye, M. M.; Kariuki, N. N.; Lin, Y. H.; Wang, C. M.; Zhong, C. J., A direct route toward assembly of nanoparticle-carbon nanotube composite materials. *Langmuir* **2004,** *20* (14), 6019-6025.

24. Fu, Q.; Lu, C. G.; Liu, J., Selective coating of single wall carbon nanotubes with thin SiO2 layer. *Nano Lett.* **2002,** *2* (4), 329-332.

25. Wen, Z. H.; Wang, Q.; Zhang, Q.; Li, J. H., In situ growth of mesoporous SnO2 on multiwalled carbon nanotubes: A novel composite with porous-tube structure as anode for lithium batteries. *Advanced Functional Materials* **2007,** *17* (15), 2772-2778.

26. Zhang, R. X.; Fan, L. Z.; Fang, Y. P.; Yang, S. H., Electrochemical route to the preparation of highly dispersed composites of ZnO/carbon nanotubes with significantly enhanced electrochemiluminescence from ZnO. *Journal of Materials Chemistry* **2008,** *18* (41), 4964-4970.

27. Pan, L.; Konishi, Y.; Tanaka, H.; Chakrabarti, S.; Hokushin, S.; Akita, S.; Nakayama, Y., Effect of MgO coating on field emission of a stand-alone carbon nanotube. *Journal of Vacuum Science & Technology B* **2007,** *25* (5), 1581-1583.

28. Sun, Z. Y.; Liu, Z. M.; Han, B. X.; Miao, S. D.; Du, J. M.; Miao, Z. J., Microstructural and electrochemical characterization of RuO2/CNT composites synthesized in supercritical diethyl amine. *Carbon* **2006,** *44* (5), 888-893.

29. Sun, Z. Y.; Zhang, X. R.; Han, B. X.; Wu, Y. Y.; An, G. M.; Liu, Z. M.; Miao, S. D.; Miao, Z. J., Coating carbon nanotubes with metal oxides in a supercritical carbon dioxide-ethanol solution. *Carbon* **2007,** *45* (13), 2589-2596.

30. Wu, R. J.; Wu, J. G.; Yu, M. R.; Tsai, T. K.; Yeh, C. T., Promotive effect of CNT on Co3O4-SnO2 in a semiconductor-type CO sensor working at room temperature. *Sensors and Actuators B-Chemical* **2008,** *131* (1), 306-312.

31. Huang, B. C.; Huang, R.; Jin, D. J.; Ye, D. Q., Low temperature SCR of NO with NH(3) over carbon nanotubes supported vanadium oxides. *Catalysis Today* **2007,** *126* (3-4), 279-283.

32. Huang, X. P.; Pan, C. X.; Huang, X. T., Preparation and characterization of gamma-MnO2/CNTs nanocomposite. *Materials Letters* **2007,** *61* (4-5), 934-936.

33. Sainsbury, T.; Fitzmaurice, D., Templated assembly of semiconductor and insulator nanoparticles at the surface of covalently modified multiwalled carbon nanotubes. *Chem. Mat.* **2004,** *16* (19), 3780-3790.

34. Li, J.; Zeng, H.; Sun, S. H.; Liu, J. P.; Wang, Z. L., Analyzing the structure of CoFe-Fe3O4 core-shell nanoparticles by electron imaging and diffraction. *Journal of Physical Chemistry B* **2004,** *108* (37), 14005-14008.

35. Hai, H. T.; Kura, H.; Takahashi, M.; Ogawa, T., Facile synthesis of Fe(3)O(4) nanoparticles by reduction phase transformation from gamma-Fe(2)O(3) nanoparticles in organic solvent. *Journal of Colloid and Interface Science* **2010,** *341* (1), 194-199.

36. Pu, H. T.; Jiang, F. J., Towards high sedimentation stability: magnetorheological fluids based on CNT/Fe3O4 nanocomposites. *Nanotechnology* **2005,** *16* (9), 1486-1489.

37. Sun, S. H.; Murray, C. B.; Weller, D.; Folks, L.; Moser, A., Monodisperse FePt nanoparticles and ferromagnetic FePt nanocrystal superlattices. *Science* **2000,** *287* (5460), 1989-1992.

38. Yi, D. K.; Lee, S. S.; Ying, J. Y., Synthesis and applications of magnetic nanocomposite catalysts. *Chemistry of Materials* **2006,** *18* (10), 2459-2461.

39. Correa-Duarte, M. A.; Grzelczak, M.; Salgueirino-Maceira, V.; Giersig, M.; Liz-Marzan, L. M.; Farle, M.; Sierazdki, K.; Diaz, R., Alignment of carbon nanotubes under low magnetic fields through attachment of magnetic nanoparticles. *J. Phys. Chem. B* **2005,** *109* (41), 19060-19063.

40. Wan, J. Q.; Cai, W.; Feng, J. T.; Meng, X. X.; Liu, E. Z., In situ decoration of carbon nanotubes with nearly monodisperse magnetite nanoparticles in liquid polyols. *Journal of Materials Chemistry* **2007,** *17* (12), 1188-1192.

41. Jia, B. P.; Gao, L.; Sun, J., Self-assembly of magnetite beads along multiwalled carbon nanotubes via a simple hydrothermal process. *Carbon* **2007,** *45* (7), 1476-1481.

42. Sun, Z. Y.; Liu, Z. M.; Wang, Y.; Han, B. X.; Du, J. M.; Zhang, J. L., Fabrication and characterization of magnetic carbon nanotube composites. *Journal of Materials Chemistry* **2005,** *15* (42), 4497-4501.

43. Youn, S. C.; Jung, D. H.; Ko, Y. K.; Jin, Y. W.; Kinri, J. M.; Jung, H. T., Vertical Alignment of Carbon Nanotubes Using the Magneto-Evaporation Method. *Journal of the American Chemical Society* **2009,** *131* (2), 742-748.

44. Mark, J. E., *Physical Properties of Polymers Handbook*. 2007.

45. Bahr, J. L.; Yang, J. P.; Kosynkin, D. V.; Bronikowski, M. J.; Smalley, R. E.; Tour, J. M., Functionalization of carbon nanotubes by electrochemical reduction of aryl diazonium salts: A bucky paper electrode. *Journal of the American Chemical Society* **2001,** *123* (27), 6536-6542.

46. Bahr, J. L.; Tour, J. M., Highly functionalized carbon nanotubes using in situ generated diazonium compounds. *Chemistry of Materials* **2001,** *13* (11), 3823-+.

47. Chen, J.; Hamon, M. A.; Hu, H.; Chen, Y. S.; Rao, A. M.; Eklund, P. C.; Haddon, R. C., Solution properties of single-walled carbon nanotubes. *Science* **1998,** *282* (5386), 95-98.

48. Chen, J.; Rao, A. M.; Lyuksyutov, S.; Itkis, M. E.; Hamon, M. A.; Hu, H.; Cohn, R. W.; Eklund, P. C.; Colbert, D. T.; Smalley, R. E.; Haddon, R. C., Dissolution of full-length single-walled carbon nanotubes. *Journal of Physical Chemistry B* **2001,** *105* (13), 2525-2528.

49. Kumar, S.; Dang, T. D.; Arnold, F. E.; Bhattacharyya, A. R.; Min, B. G.; Zhang, X. F.; Vaia, R. A.; Park, C.; Adams, W. W.; Hauge, R. H.; Smalley, R. E.; Ramesh, S.; Willis, P. A., Synthesis, structure, and properties of PBO/SWNT composites. *Macromolecules* **2002,** *35* (24), 9039-9043.

50. Niyogi, S.; Hamon, M. A.; Hu, H.; Zhao, B.; Bhowmik, P.; Sen, R.; Itkis, M. E.; Haddon, R. C., Chemistry of single-walled carbon nanotubes. *Accounts of Chemical Research* **2002,** *35* (12), 1105-1113.

51. Satake, A.; Miyajima, Y.; Kobuke, Y., Porphyrin - Carbon nanotube composites formed by noncovalent polymer wrapping. *Chem. Mat.* **2005,** *17* (4), 716-724.

52. Coleman, J. N.; Khan, U.; Gun'ko, Y. K., Mechanical reinforcement of polymers using carbon nanotubes. *Advanced Materials* **2006,** *18* (6), 689-706.

53. Ciprari, D.; Jacob, K.; Tannenbaum, R., Characterization of polymer nanocomposite interphase and its impact on mechanical properties. *Macromolecules* **2006,** *39* (19), 6565-6573.

54. Chen, X. Q.; Saito, T.; Yamada, H.; Matsushige, K., Aligning single-wall carbon nanotubes with an alternating-current electric field. *Applied Physics Letters* **2001,** *78* (23), 3714-3716.

55. Nagahara, L. A.; Amlani, I.; Lewenstein, J.; Tsui, R. K., Directed placement of suspended carbon nanotubes for nanometer-scale assembly. *Applied Physics Letters* **2002,** *80* (20), 3826-3828.

56. Martin, C. A.; Sandler, J. K. W.; Windle, A. H.; Schwarz, M. K.; Bauhofer, W.; Schulte, K.; Shaffer, M. S. P., Electric field-induced aligned multi-wall carbon nanotube networks in epoxy composites. *Polymer* **2005,** *46* (3), 877-886.

57. Zhu, Y.-F.; Ma, C.; Zhang, W.; Zhang, R.-P.; Koratkar, N.; Liang, J., Alignment of multiwalled carbon nanotubes in bulk epoxy composites via electric field. *Journal of Applied Physics* **2009,** *105* (5).

58. Camponeschi, E.; Florkowski, B.; Vance, R.; Garrett, G.; Garmestani, H.; Tannenbaum, R., Uniform directional alignment of single-walled carbon nanotubes in. viscous polymer flow. *Langmuir* **2006,** *22* (4), 1858-1862.

59. Fujiwara, M.; Oki, E.; Hamada, M.; Tanimoto, Y.; Mukouda, I.; Shimomura, Y., Magnetic orientation and magnetic properties of a single carbon nanotube. *Journal of Physical Chemistry A* **2001,** *105* (18), 4383-4386.

60. Steinert, B. W.; Dean, D. R., Magnetic field alignment and electrical properties of solution cast PET-carbon nanotube composite films. *Polymer* **2009,** *50* (3), 898-904.

61. Camponeschi, E.; Vance, R.; Al-Haik, M.; Garmestani, H.; Tannenbaum, R., Properties of carbon nanotube-polymer composites aligned in a magnetic field. *Carbon* **2007,** *45* (10), 2037-2046.

62. Grady, B. P.; Pompeo, F.; Shambaugh, R. L.; Resasco, D. E., Nucleation of polypropylene crystallization by single-walled carbon nanotubes. *J. Phys. Chem. B* **2002,** *106* (23), 5852-5858.

63. Probst, O.; Moore, E. M.; Resasco, D. E.; Grady, B. P., Nucleation of polyvinyl alcohol crystallization by single-walled carbon nanotubes. *Polymer* **2004,** *45* (13), 4437-4443.

64. Valentini, L.; Biagiotti, J.; Kenny, J. M.; Santucci, S., Effects of single-walled carbon nanotubes on the crystallization behavior of polypropylene. *J. Appl. Polym. Sci.* **2003,** *87* (4), 708-713.

65. Albertsson, A. C.; Varma, I. K., Recent developments in ring opening polymerization of lactones for biomedical applications. *Biomacromolecules* **2003,** *4* (6), 1466-1486.

66. Mecerreyes, D.; Jerome, R.; Dubois, P., Novel macromolecular architectures based on aliphatic polyesters: Relevance of the "coordination-insertion" ring-opening polymerization. *Macromolecular Architectures* **1999,** *147*, 1-59.

67. Trollsas, M.; Hedrick, J. L., Dendrimer-like star polymers. *J. Am. Chem. Soc.* **1998,** *120* (19), 4644-4651.

68. Goh, H. W.; Goh, S. H.; Xu, G. Q.; Pramoda, K. P.; Zhang, W. D., Crystallization and dynamic mechanical behavior of double-C-60-end-capped poly(ethylene oxide)/multi-walled carbon nanotube composites. *Chemical Physics Letters* **2003,** *379* (3-4), 236-241.

69. Chatterjee, T.; Yurekli, K.; Hadjiev, V. G.; Krishnamoorti, R., Single-walled carbon nanotube dispersions in poly(ethylene oxide). *Advanced Functional Materials* **2005,** *15* (11), 1832-1838.

70. Jin, J.; Song, M.; Pan, F., A DSC study of effect of carbon nanotubes on crystallisation behaviour of poly(ethylene oxide). *Thermochim. Acta* **2007,** *456* (1), 25-31.

71. Shieh, Y. T.; Liu, G. L.; Hwang, K. C.; Chen, C. C., Crystallization, melting and morphology of PEO in PEO/MWNT-g-PMMA blends. *Polymer* **2005,** *46* (24), 10945-10951.

72. Priftis, D.; Sakellariou, G.; Hadjichristidis, N.; Penott, E. K.; Lorenzo, A. T.; Muller, A. J., Surface Modification of Multiwalled Carbon Nanotubes with Biocompatible Polymers via Ring Opening and Living Anionic Surface Initiated Polymerization. Kinetics and Crystallization Behavior. *J. Polym. Sci. Pol. Chem.* **2009,** *47* (17), 4379-4390.

73. Garmestani, H.; Al-Haik, M. S.; Dahmen, K.; Tannenbaum, R.; Li, D. S.; Sablin, S. S.; Hussaini, M. Y., Polymer-mediated alignment of carbon nanotubes under high magnetic fields. *Adv. Mater.* **2003,** *15* (22), 1918-+.

74. Novoselov, K. S.; Geim, A. K.; Morozov, S. V.; Jiang, D.; Zhang, Y.; Dubonos, S. V.; Grigorieva, I. V.; Firsov, A. A., Electric field effect in atomically thin carbon films. *Science* **2004,** *306* (5696), 666-669.

75. Rao, C. N. R. R. C. N. R.; Sood, A. K.; Subrahmanyam, K. S.; Govindaraj, A., Graphene: The New Two-Dimensional Nanomaterial. *Angew. Chem.-Int. Edit.* **2009,** *48* (42), 7752-7777.

76. Geim, A. K.; Novoselov, K. S., The rise of graphene. *Nat. Mater.* **2007,** *6* (3), 183-191.

77. Lee, C.; Wei, X. D.; Kysar, J. W.; Hone, J., Measurement of the elastic properties and intrinsic strength of monolayer graphene. *Science* **2008,** *321* (5887), 385-388.

78. Balandin, A. A.; Ghosh, S.; Bao, W. Z.; Calizo, I.; Teweldebrhan, D.; Miao, F.; Lau, C. N., Superior thermal conductivity of single-layer graphene. *Nano Lett.* **2008,** *8* (3), 902-907.

79. Park, S.; Ruoff, R. S., Chemical methods for the production of graphenes. *Nature Nanotechnology* **2009,** *4* (4), 217-224.

80. Li, X. S.; Cai, W. W.; An, J. H.; Kim, S.; Nah, J.; Yang, D. X.; Piner, R.; Velamakanni, A.; Jung, I.; Tutuc, E.; Banerjee, S. K.; Colombo, L.; Ruoff, R. S., Large-Area Synthesis of High-Quality and Uniform Graphene Films on Copper Foils. *Science* **2009,** *324* (5932), 1312-1314.

81. Dervishi, E.; Li, Z. R.; Watanabe, F.; Biswas, A.; Xu, Y.; Biris, A. R.; Saini, V.; Biris, A. S., Large-scale graphene production by RF-cCVD method. *Chem. Commun.* **2009,** (27), 4061-4063.

82. Reina, A.; Jia, X. T.; Ho, J.; Nezich, D.; Son, H. B.; Bulovic, V.; Dresselhaus, M. S.; Kong, J., Large Area, Few-Layer Graphene Films on Arbitrary Substrates by Chemical Vapor Deposition. *Nano Lett.* **2009,** *9* (1), 30-35.

83. Nandamuri, G.; Roumimov, S.; Solanki, R., Chemical vapor deposition of graphene films. *Nanotechnology* **2010,** *21* (14), 4.

84. Shivaraman, S.; Barton, R. A.; Yu, X.; Alden, J.; Herman, L.; Chandrashekhar, M. V. S.; Park, J.; McEuen, P. L.; Parpia, J. M.; Craighead, H. G.; Spencer, M. G., Free-Standing Epitaxial Graphene. *Nano Lett.* **2009,** *9* (9), 3100-3105.

85. Aristov, V. Y.; Urbanik, G.; Kummer, K.; Vyalikh, D. V.; Molodtsova, O. V.; Preobrajenski, A. B.; Zakharov, A. A.; Hess, C.; Hanke, T.; Buchner, B.; Vobornik, I.; Fujii, J.; Panaccione, G.; Ossipyan, Y. A.; Knupfer, M., Graphene Synthesis on Cubic SiC/Si Wafers. Perspectives for Mass Production of Graphene-Based Electronic Devices. *Nano Letters* **2010,** *10* (3), 992-995.

86. Emtsev, K. V.; Bostwick, A.; Horn, K.; Jobst, J.; Kellogg, G. L.; Ley, L.; McChesney, J. L.; Ohta, T.; Reshanov, S. A.; Rohrl, J.; Rotenberg, E.; Schmid, A. K.; Waldmann, D.; Weber, H. B.; Seyller, T., Towards wafer-size graphene layers by atmospheric pressure graphitization of silicon carbide. *Nat. Mater.* **2009,** *8* (3), 203-207.

87. Dato, A.; Radmilovic, V.; Lee, Z.; Phillips, J.; Frenklach, M., Substrate-free gas-phase synthesis of graphene sheets. *Nano Lett.* **2008,** *8* (7), 2012-2016.

88. Dato, A.; Lee, Z.; Jeon, K. J.; Erni, R.; Radmilovic, V.; Richardson, T. J.; Frenklach, M., Clean and highly ordered graphene synthesized in the gas phase. *Chem. Commun.* **2009,** (40), 6095-6097.

89. Dreyer, D. R.; Park, S.; Bielawski, C. W.; Ruoff, R. S., The chemistry of graphene oxide. *Chemical Society Reviews* **2010,** *39* (1), 228-240.

90. Brodie, B. C., Ann. Chim. Phys., 1860; Vol. 59, p 466.

91. Staudenmaier, L., Ber. Deut. Chem. Ges., 1898; Vol. 31, p 1481.

92. Hummers, W. S.; Offeman, R. E., PREPARATION OF GRAPHITIC OXIDE. *J. Am. Chem. Soc.* **1958,** *80* (6), 1339-1339.

93. Cai, W. W.; Piner, R. D.; Stadermann, F. J.; Park, S.; Shaibat, M. A.; Ishii, Y.; Yang, D. X.; Velamakanni, A.; An, S. J.; Stoller, M.; An, J. H.; Chen, D. M.; Ruoff, R. S., Synthesis and solid-state NMR structural characterization of C-13-labeled graphite oxide. *Science* **2008,** *321* (5897), 1815-1817.

94. He, H. Y.; Klinowski, J.; Forster, M.; Lerf, A., A new structural model for graphite oxide. *Chemical Physics Letters* **1998,** *287* (1-2), 53-56.

95. Paredes, J. I.; Villar-Rodil, S.; Martinez-Alonso, A.; Tascon, J. M. D., Graphene oxide dispersions in organic solvents. *Langmuir* **2008,** *24* (19), 10560-10564.

96. Compton, O. C.; Nguyen, S. T., Graphene Oxide, Highly Reduced Graphene Oxide, and Graphene: Versatile Building Blocks for Carbon-Based Materials. *Small* **2010,** *6* (6), 711-723.

97. Li, D.; Muller, M. B.; Gilje, S.; Kaner, R. B.; Wallace, G. G., Processable aqueous dispersions of graphene nanosheets. *Nature Nanotechnology* **2008,** *3* (2), 101-105.

98. Dong, X. C.; Su, C. Y.; Zhang, W. J.; Zhao, J. W.; Ling, Q. D.; Huang, W.; Chen, P.; Li, L. J., Ultra-large single-layer graphene obtained from solution chemical reduction and its electrical properties. *Physical Chemistry Chemical Physics* **2010,** *12* (9), 2164-2169.

99. Patil, A. J.; Vickery, J. L.; Scott, T. B.; Mann, S., Aqueous Stabilization and Self-Assembly of Graphene Sheets into Layered Bio-Nanocomposites using DNA. *Adv. Mater.* **2009,** *21* (31), 3159-+.

100. Qi, X. Y.; Pu, K. Y.; Zhou, X. Z.; Li, H.; Liu, B.; Boey, F.; Huang, W.; Zhang, H., Conjugated-Polyelectrolyte-Functionalized Reduced Graphene Oxide with Excellent Solubility and Stability in Polar Solvents. *Small* **2010,** *6* (5), 663-669.

101. Xu, Y. X.; Bai, H.; Lu, G. W.; Li, C.; Shi, G. Q., Flexible graphene films via the filtration of water-soluble noncovalent functionalized graphene sheets. *J. Am. Chem. Soc.* **2008,** *130* (18), 5856-+.

102. Geng, J.; Jung, H., Porphyrin Functionalized Graphene Sheets in Aqueous Suspensions: From the Preparation of Graphene Sheets to Highly Conductive Graphene Films. *Journal of Physical Chemistry C* **2010,** *114* (18), 8227-8234.

103. Yang, Q.; Pan, X. J.; Huang, F.; Li, K. C., Fabrication of High-Concentration and Stable Aqueous Suspensions of Graphene Nanosheets by Noncovalent Functionalization with Lignin and Cellulose Derivatives. *Journal of Physical Chemistry C* **2010,** *114* (9), 3811-3816.

104. Ghosh, A.; Rao, K. V.; George, S. J.; Rao, C. N. R., Noncovalent Functionalization, Exfoliation, and Solubilization of Graphene in Water by Employing a Fluorescent Coronene Carboxylate. *Chemistry-a European Journal* **2010,** *16* (9), 2700-2704.

105. Zhou, X. F.; Liu, Z. P., A scalable, solution-phase processing route to graphene oxide and graphene ultralarge sheets. *Chemical Communications* **2010,** *46* (15), 2611-2613.

106. Zhou, X. S.; Wu, T. B.; Ding, K. L.; Hu, B. J.; Hou, M. Q.; Han, B. X., Dispersion of graphene sheets in ionic liquid bmim PF(6) stabilized by an ionic liquid polymer. *Chemical Communications* **2010,** *46* (3), 386-388.

107. Guo, Y. J.; Guo, S. J.; Ren, J. T.; Zhai, Y. M.; Dong, S. J.; Wang, E. K., Cyclodextrin Functionalized Graphene Nanosheets with High Supramolecular Recognition Capability: Synthesis and Host-Guest Inclusion for Enhanced Electrochemical Performance. *Acs Nano* **2010,** *4* (7), 4001-4010.

108. Zhang, J. L.; Yang, H. J.; Shen, G. X.; Cheng, P.; Zhang, J. Y.; Guo, S. W., Reduction of graphene oxide via L-ascorbic acid. *Chemical Communications* **2010,** *46* (7), 1112-1114.

109. Gao, J.; Liu, F.; Liu, Y. L.; Ma, N.; Wang, Z. Q.; Zhang, X., Environment-Friendly Method To Produce Graphene That Employs Vitamin C and Amino Acid. *Chemistry of Materials* **2010,** *22* (7), 2213-2218.

110. Fan, X. B.; Peng, W. C.; Li, Y.; Li, X. Y.; Wang, S. L.; Zhang, G. L.; Zhang, F. B., Deoxygenation of Exfoliated Graphite Oxide under Alkaline Conditions: A Green Route to Graphene Preparation. *Advanced Materials* **2008,** *20* (23), 4490-4493.

111. Che, J. F.; Shen, L. Y.; Xiao, Y. H., A new approach to fabricate graphene nanosheets in organic medium: combination of reduction and dispersion. *Journal of Materials Chemistry* **2010,** *20* (9), 1722-1727.

112. Choi, E. Y.; Han, T. H.; Hong, J. H.; Kim, J. E.; Lee, S. H.; Kim, H. W.; Kim, S. O., Noncovalent functionalization of graphene with end-functional polymers. *Journal of Materials Chemistry* **2010,** *20* (10), 1907-1912.

113. Watcharotone, S.; Dikin, D. A.; Stankovich, S.; Piner, R.; Jung, I.; Dommett, G. H. B.; Evmenenko, G.; Wu, S. E.; Chen, S. F.; Liu, C. P.; Nguyen, S. T.; Ruoff, R. S., Graphene-silica composite thin films as transparent conductors. *Nano Lett.* **2007,** *7* (7), 1888-1892.

114. Yang, S. B.; Feng, X. L.; Wang, L.; Tang, K.; Maier, J.; Mullen, K., Graphene-Based Nanosheets with a Sandwich Structure. *Angewandte Chemie-International Edition* **2010,** *49* (28), 4795-4799.

115. Wang, H. L.; Robinson, J. T.; Diankov, G.; Dai, H. J., Nanocrystal Growth on Graphene with Various Degrees of Oxidation. *Journal of the American Chemical Society* **2010,** *132* (10), 3270-+.

116. Cong, H. P.; He, J. J.; Lu, Y.; Yu, S. H., Water-Soluble Magnetic-Functionalized Reduced Graphene Oxide Sheets: In situ Synthesis and Magnetic Resonance Imaging Applications. *Small* **2010,** *6* (2), 169-173.

117. Yang, X. Y.; Zhang, X. Y.; Ma, Y. F.; Huang, Y.; Wang, Y. S.; Chen, Y. S., Superparamagnetic graphene oxide-Fe(3)O(4) nanoparticles hybrid for controlled targeted drug carriers. *Journal of Materials Chemistry* **2009,** *19* (18), 2710-2714.

118. Yao, H. B.; Wu, L. H.; Cui, C. H.; Fang, H. Y.; Yu, S. H., Direct fabrication of photoconductive patterns on LBL assembled graphene oxide/PDDA/titania hybrid films by photothermal and photocatalytic reduction. *Journal of Materials Chemistry* **2010,** *20* (25), 5190-5195.

119. Williams, G.; Seger, B.; Kamat, P. V., TiO(2)-graphene nanocomposites. UV-assisted photocatalytic reduction of graphene oxide. *ACS Nano* **2008,** *2* (7), 1487-1491.

120. Zhang, H.; Lv, X. J.; Li, Y. M.; Wang, Y.; Li, J. H., P25-Graphene Composite as a High Performance Photocatalyst. *Acs Nano* **2010,** *4* (1), 380-386.

121. Zhu, C. Z.; Guo, S. J.; Wang, P.; Xing, L.; Fang, Y. X.; Zhai, Y. M.; Dong, S. J., One-pot, water-phase approach to high-quality graphene/TiO(2) composite nanosheets. *Chemical Communications* **2010,** *46* (38), 7148-7150.

122. Paek, S. M.; Yoo, E.; Honma, I., Enhanced Cyclic Performance and Lithium Storage Capacity of SnO2/Graphene Nanoporous Electrodes with Three-Dimensionally Delaminated Flexible Structure. *Nano Lett.* **2009,** *9* (1), 72-75.

123. Li, F. H.; Song, J. F.; Yang, H. F.; Gan, S. Y.; Zhang, Q. X.; Han, D. X.; Ivaska, A.; Niu, L., One-step synthesis of graphene/SnO(2) nanocomposites and its application in electrochemical supercapacitors. *Nanotechnology* **2009,** *20* (45), 6.

124. Zhang, L. S.; Jiang, L. Y.; Yan, H. J.; Wang, W. D.; Wang, W.; Song, W. G.; Guo, Y. G.; Wan, L. J., Mono dispersed SnO(2) nanoparticles on both sides of single layer graphene sheets as anode materials in Li-ion batteries. *Journal of Materials Chemistry* **2010,** *20* (26), 5462-5467.

125. Lee, J. M.; Pyun, Y. B.; Yi, J.; Choung, J. W.; Park, W. I., ZnO Nanorod-Graphene Hybrid Architectures for Multifunctional Conductors. *Journal of Physical Chemistry C* **2009,** *113* (44), 19134-19138.

126. Williams, G.; Kamat, P. V., Graphene-Semiconductor Nanocomposites: Excited-State Interactions between ZnO Nanoparticles and Graphene Oxide. *Langmuir* **2009,** *25* (24), 13869-13873.

127. Fan, Y. C.; Wang, L. J.; Li, J. L.; Li, J. Q.; Sun, S. K.; Chen, F.; Chen, L. D.; Jiang, W., Preparation and electrical properties of graphene nanosheet/Al(2)O(3) composites. *Carbon* **2010,** *48* (6), 1743-1749.

128. Wu, Z. S.; Ren, W. C.; Wen, L.; Gao, L. B.; Zhao, J. P.; Chen, Z. P.; Zhou, G. M.; Li, F.; Cheng, H. M., Graphene Anchored with Co(3)O(4) Nanoparticles as Anode of Lithium Ion Batteries with Enhanced Reversible Capacity and Cyclic Performance. *Acs Nano* **2010,** *4* (6), 3187-3194.

129. Chen, S.; Zhu, J. W.; Wang, X., One-Step Synthesis of Graphene-Cobalt Hydroxide Nanocomposites and Their Electrochemical Properties. *Journal of Physical Chemistry C* **2010,** *114* (27), 11829-11834.

130. Chen, S.; Zhu, J. W.; Wu, X. D.; Han, Q. F.; Wang, X., Graphene Oxide-MnO(2) Nanocomposites for Supercapacitors. *Acs Nano* **2010,** *4* (5), 2822-2830.

131. Li, Y. M.; Somorjai, G. A., Nanoscale Advances in Catalysis and Energy Applications. *Nano Letters* **2010,** *10* (7), 2289-2295.

132. Tarascon, J. M.; Armand, M., Issues and challenges facing rechargeable lithium batteries. *Nature* **2001,** *414* (6861), 359-367.

133. Evanoff, K.; Magasinski, A.; Yang, J.; Yushin, G., Nanosilicon-Coated Graphene Granules as Anodes for Li-Ion Batteries. *Advanced Energy Materials* **2011,** *1* (4), 495-498.

134. Hertzberg, B.; Alexeev, A.; Yushin, G., Deformations in Si-Li Anodes Upon Electrochemical Alloying in Nano-Confined Space. *Journal of the American Chemical Society* **2010,** *132* (25), 8548-+.

135. Magasinski, A.; Dixon, P.; Hertzberg, B.; Kvit, A.; Ayala, J.; Yushin, G., High-performance lithium-ion anodes using a hierarchical bottom-up approach. *Nature Materials* **2010,** *9* (4), 353-358.

136. Magasinski, A.; Zdyrko, B.; Kovalenko, I.; Hertzberg, B.; Burtovyy, R.; Huebner, C. F.; Fuller, T. F.; Luzinov, I.; Yushin, G., Toward Efficient Binders for Li-Ion Battery Si-Based Anodes: Polyacrylic Acid. *Acs Applied Materials & Interfaces* **2010,** *2* (11), 3004-3010.

137. Li, Y. G.; Tan, B.; Wu, Y. Y., Mesoporous CO3O4 nanowire arrays for lithium ion batteries with high capacity and rate capability. *Nano Lett.* **2008,** *8* (1), 265-270.

138. Lou, X. W.; Wang, Y.; Yuan, C. L.; Lee, J. Y.; Archer, L. A., Template-free synthesis of SnO2 hollow nanostructures with high lithium storage capacity. *Adv. Mater.* **2006,** *18* (17), 2325-+.

139. Poizot, P.; Laruelle, S.; Grugeon, S.; Dupont, L.; Tarascon, J. M., Nano-sized transition-metaloxides as negative-electrode materials for lithium-ion batteries. *Nature* **2000,** *407* (6803), 496-499.

140. Reddy, M. V.; Yu, T.; Sow, C. H.; Shen, Z. X.; Lim, C. T.; Rao, G. V. S.; Chowdari, B. V. R., alpha-Fe2O3 nanoflakes as an anode material for Li-ion batteries. *Advanced Functional Materials* **2007,** *17* (15), 2792-2799.

141. Zhi, L. J.; Hu, Y. S.; El Hamaoui, B.; Wang, X.; Lieberwirth, I.; Kolb, U.; Maier, J.; Mullen, K., Precursor-controlled formation of novel carbon/metal and carbon/metal oxide nanocomposites. *Adv. Mater.* **2008,** *20* (9), 1727-+.

142. Qiao, H.; Xiao, L. F.; Zheng, Z.; Liu, H. W.; Jia, F. L.; Zhang, L. Z., One-pot synthesis of CoO/C hybrid microspheres as anode materials for lithium-ion batteries. *Journal of Power Sources* **2008,** *185* (1), 486-491.

143. Wu, X. L.; Guo, Y. G.; Wan, L. J.; Hu, C. W., alpha-Fe2O3 Nanostructures: Inorganic Salt-Controlled Synthesis and Their Electrochemical Performance toward Lithium Storage. *J. Phys. Chem. C* **2008,** *112* (43), 16824-16829.

144. Xiang, J. Y.; Tu, J. P.; Zhang, L.; Zhou, Y.; Wang, X. L.; Shi, S. J., Simple synthesis of surface-modified hierarchical copper oxide spheres with needle-like morphology as anode for lithium ion batteries. *Electrochimica Acta* **2010,** *55* (5), 1820-1824.

145. Yuan, L.; Guo, Z. P.; Konstantinov, K.; Munroe, P.; Liu, H. K., Spherical clusters of NiO nanoshafts for lithium-ion battery anodes. *Electrochem. Solid State Lett.* **2006,** *9* (11), A524-A528.

146. Chen, L. B.; Lu, N.; Xu, C. M.; Yu, H. C.; Wang, T. H., Electrochemical performance of polycrystalline CuO nanowires as anode material for Li ion batteries. *Electrochimica Acta* **2009,** *54* (17), 4198-4201.

147. Cui, Z. M.; Hang, L. Y.; Song, W. G.; Guo, Y. G., High-Yield Gas-Liquid Interfacial Synthesis of Highly Dispersed Fe3O4 Nanocrystals and Their Application in Lithium-Ion Batteries. *Chemistry of Materials* **2009,** *21* (6), 1162-1166.

148. Guo, P.; Song, H. H.; Chen, X. H., Electrochemical performance of graphene nanosheets as anode material for lithium-ion batteries. *Electrochem. Commun.* **2009,** *11* (6), 1320-1324.

149. Pan, D. Y.; Wang, S.; Zhao, B.; Wu, M. H.; Zhang, H. J.; Wang, Y.; Jiao, Z., Li Storage Properties of Disordered Graphene Nanosheets. *Chem. Mat.* **2009,** *21* (14), 3136-3142.

150. Wang, G. X.; Shen, X. P.; Yao, J.; Park, J., Graphene nanosheets for enhanced lithium storage in lithium ion batteries. *Carbon* **2009,** *47* (8), 2049-2053.

151. Yoo, E.; Kim, J.; Hosono, E.; Zhou, H.; Kudo, T.; Honma, I., Large reversible Li storage of graphene nanosheet families for use in rechargeable lithium ion batteries. *Nano Lett.* **2008,** *8* (8), 2277-2282.

152. Kim, H. K.; Bak, S. M.; Kim, K. B., Li4Ti5O12/reduced graphite oxide nano-hybrid material for high rate lithium-ion batteries. *Electrochem. Commun.* **2010,** *12* (12), 1768-1771.

153. Wang, J. Z.; Zhong, C.; Wexler, D.; Idris, N. H.; Wang, Z. X.; Chen, L. Q.; Liu, H. K., Graphene-Encapsulated Fe3O4 Nanoparticles with 3D Laminated Structure as Superior Anode in Lithium Ion Batteries. *Chemistry-a European Journal* **2011,** *17* (2), 661-667.

154. Zhang, M.; Lei, D. N.; Yin, X. M.; Chen, L. B.; Li, Q. H.; Wang, Y. G.; Wang, T. H., Magnetite/graphene composites: microwave irradiation synthesis and enhanced cycling and rate performances for lithium ion batteries. *Journal of Materials Chemistry* **2010,** *20* (26), 5538-5543.

155. Zhou, G. M.; Wang, D. W.; Li, F.; Zhang, L. L.; Li, N.; Wu, Z. S.; Wen, L.; Lu, G. Q.; Cheng, H. M., Graphene-Wrapped Fe3O4 Anode Material with Improved Reversible Capacity and Cyclic Stability for Lithium Ion Batteries. *Chem. Mat.* **2010,** *22* (18), 5306-5313.

156. Wang, H. L.; Cui, L. F.; Yang, Y. A.; Casalongue, H. S.; Robinson, J. T.; Liang, Y. Y.; Cui, Y.; Dai, H. J., Mn3O4-Graphene Hybrid as a High-Capacity Anode Material for Lithium Ion Batteries. *J. Am. Chem. Soc.* **2010,** *132* (40), 13978-13980.

157. Zhu, J. X.; Zhu, T.; Zhou, X. Z.; Zhang, Y. Y.; Lou, X. W.; Chen, X. D.; Zhang, H.; Hng, H. H.; Yan, Q. Y., Facile synthesis of metal oxide/reduced graphene oxide hybrids with high lithium storage capacity and stable cyclability. *Nanoscale* **2011,** *3* (3), 1084-1089.

158. Matarredona, O.; Rhoads, H.; Li, Z. R.; Harwell, J. H.; Balzano, L.; Resasco, D. E., Dispersion of single-walled carbon nanotubes in aqueous solutions of the anionic surfactant NaDDBS. *J. Phys. Chem. B* **2003,** *107* (48), 13357-13367.

159. Can, M. M.; Ozcan, S.; Firat, T., Magnetic behaviour of iron nanoparticles passivated by oxidation. *Physica Status Solidi C - Current Topics in Solid State Physics, Vol 3, No 5* **2006**, 1271-1278.

160. Khomutov, G. B.; Kislov, V. V.; Gainutdinov, R. V.; Gubin, S. P.; Obydenov, A. Y.; Pavlov, S. A.; Sergeev-Cherenkov, A. N.; Soldatov, E. S.; Tolstikhina, A. L.; Trifonov, A. S., The design, fabrication and characterization of controlled-morphology nanomaterials and functional planar molecular nanocluster-based nanostructures. *Surface Science* **2003,** *532*, 287-293.

161. Livage, J.; Henry, M.; Sanchez, C., SOL-GEL CHEMISTRY OF TRANSITION-METAL OXIDES. *Prog. Solid State Chem.* **1988,** *18* (4), 259-341.

162. Gash, A. E.; Tillotson, T. M.; Satcher, J. H.; Poco, J. F.; Hrubesh, L. W.; Simpson, R. L., Use of epoxides in the sol-gel synthesis of porous iron(III) oxide monoliths from Fe(III) salts. *Chem. Mat.* **2001,** *13* (3), 999-1007.

163. Gash, A. E.; Satcher, J. H.; Simpson, R. L., Strong akaganeite aerogel monoliths using epoxides: Synthesis and characterization. *Chem. Mat.* **2003,** *15* (17), 3268-3275.

164. Walker, J. D.; Tannenbaum, R., Characterization of the sol-gel formation of iron(III) oxide/hydroxide nanonetworks from weak base molecules. *Chem. Mat.* **2006,** *18* (20), 4793-4801.

165. Lukic, B.; Seo, J. W.; Bacsa, R. R.; Delpeux, S.; Beguin, F.; Bister, G.; Fonseca, A.; Nagy, J. B.; Kis, A.; Jeney, S.; Kulik, A. J.; Forro, L., Catalytically grown carbon nanotubes of small diameter have a high Young's modulus. *Nano Lett.* **2005,** *5* (10), 2074-2077.

166. Kimura, T.; Ago, H.; Tobita, M.; Ohshima, S.; Kyotani, M.; Yumura, M., Polymer composites of carbon nanotubes aligned by a magnetic field. *Adv. Mater.* **2002,** *14* (19), 1380-1383.

167. Millan, A.; Palacio, F.; Falqui, A.; Snoeck, E.; Serin, V.; Bhattacharjee, A.; Ksenofontov, V.; Gutlich, P.; Gilbert, I., Maghemite polymer nanocomposites with modulated magnetic properties. *Acta Mater.* **2007,** *55* (6), 2201-2209.

168. White, W. B.; Deangeli.Ba, INTERPRETATION OF VIBRATIONAL SPECTRA OF SPINELS. *Spectrochimica Acta Part a-Molecular Spectroscopy* **1967,** *A 23* (4), 985-&.

169. deFaria, D. L. A.; Silva, S. V.; deOliveira, M. T., Raman microspectroscopy of some iron oxides and oxyhydroxides. *J. Raman Spectrosc.* **1997,** *28* (11), 873-878.

170. Hyeon, T.; Lee, S. S.; Park, J.; Chung, Y.; Bin Na, H., Synthesis of highly crystalline and monodisperse maghemite nanocrystallites without a size-selection process. *J. Am. Chem. Soc.* **2001,** *123* (51), 12798-12801.

171. Sun, Z. Y.; Yuan, H. Q.; Liu, Z. M.; Han, B. X.; Zhang, X. R., A highly efficient chemical sensor material for H2S: alpha-Fe2O3 nanotubes fabricated using carbon nanotube templates. *Adv. Mater.* **2005,** *17* (24), 2993-+.

172. Jorio, A.; Pimenta, M. A.; Souza, A. G.; Saito, R.; Dresselhaus, G.; Dresselhaus, M. S., Characterizing carbon nanotube samples with resonance Raman scattering. *New J. Phys.* **2003,** *5*, 17.

173. Fermigier, M.; Gast, A. P., STRUCTURE EVOLUTION IN A PARAMAGNETIC LATEX SUSPENSION. *J. Colloid Interface Sci.* **1992,** *154* (2), 522-539.

174. Pascal, C.; Pascal, J. L.; Favier, F.; Moubtassim, M. L. E.; Payen, C., Electrochemical synthesis for the control of gamma-Fe2O3 nanoparticle size. Morphology, microstructure, and magnetic behavior. *Chem. Mat.* **1999,** *11* (1), 141-147.

175. Sousa, M. H.; Rubim, J. C.; Sobrinho, P. G.; Tourinho, F. A., Biocompatible magnetic fluid precursors based on aspartic and glutamic acid modified maghemite nanostructures. *J. Magn. Magn. Mater.* **2001,** *225* (1-2), 67-72.

176. Sincai, M.; Ganga, D.; Bica, D.; Vekas, L., The antitumor effect of locoregional magnetic cobalt ferrite in dog mammary adenocarcinoma. *J. Magn. Magn. Mater.* **2001,** *225* (1-2), 235-240.

177. Butter, K.; Bomans, P. H.; Frederik, P. M.; Vroege, G. J.; Philipse, A. P., Direct observation of dipolar chains in ferrofluids in zero field using cryogenic electron microscopy. *J. Phys.-Condes. Matter* **2003,** *15* (15), S1451-S1470.

178. Weber, M.; Kamal, M. R., Estimation of the volume resistivity of electrically conductive composites. *Polym. Compos.* **1997,** *18* (6), 711-725.

179. Mei, Y.; Zhou, Z. J.; Luo, H. L., ELECTRICAL-RESISTIVITY OF RF-SPUTTERED IRON-OXIDE THIN-FILMS. *J. Appl. Phys.* **1987,** *61* (8), 4388-4389.

180. Kim, I. T.; Nunnery, G. A.; Jacob, K.; Schwartz, J.; Liu, X. T.; Tannenbaum, R., Synthesis, Characterization, and Alignment of Magnetic Carbon Nanotubes Tethered with Maghemite Nanoparticles. *J. Phys. Chem. C* **2010,** *114* (15), 6944-6951.

181. Kim, I. T.; Tannenbaum, A.; Tannenbaum, R., Anisotropic conductivity of magnetic carbon nanotubes embedded in epoxy matrices. *Carbon* **2011,** *49* (1), 54-61.

182. Kaur, J.; Shofner, M. L., Surface Area Effects in Hydroxyapatite/Poly(epsilon-caprolactone) Nanocomposites. *Macromolecular Chemistry and Physics* **2009,** *210* (8), 677-688.

183. Lu, Y. L.; Zhang, G. B.; Feng, M.; Zhang, Y.; Yang, M. S.; Shen, D. Y., Hydrogen bonding in polyamide 66/clay nanocomposite. *Journal of Polymer Science Part B-Polymer Physics* **2003,** *41* (19), 2313-2321.

184. Chen, B. Q.; Evans, J. R. G., Poly(epsilon-caprolactone)-clay nanocomposites: Structure and mechanical properties. *Macromolecules* **2006,** *39* (2), 747-754.

185. Zhu, L.; Cheng, S. Z. D.; Calhoun, B. H.; Ge, Q.; Quirk, R. P.; Thomas, E. L.; Hsiao, B. S.; Yeh, F. J.; Lotz, B., Crystallization temperature-dependent crystal orientations within nanoscale confined lamellae of a self-assembled crystalline-amorphous diblock copolymer. *J. Am. Chem. Soc.* **2000,** *122* (25), 5957-5967.

186. Takahash.Y; Tadokoro, H., STRUCTURAL STUDIES OF POLYETHERS, (-(CH2)M-O-)N .10. CRYSTAL-STRUCTURE OF POLY(ETHYLENE OXIDE). *Macromolecules* **1973,** *6* (5), 672-675.

187. Wang, H. P.; Keum, J. K.; Hiltner, A.; Baer, E., Impact of Nanoscale Confinement on Crystal Orientation of Poly(ethylene oxide). *Macromolecular Rapid Communications 31* (4), 356-361.

188. Wang, W. Q.; Liu, W. J.; Tudryn, G. J.; Colby, R. H.; Winey, K. I., Multi-Length Scale Morphology of Poly(ethylene oxide)-Based Sulfonate Ionomers with Alkali Cations at Room Temperature. *Macromolecules 43* (9), 4223-4229.

189. Zheng, X.; Xu, Q., Comparison Study of Morphology and Crystallization Behavior of Polyethylene and Poly(ethylene oxide) on Single-Walled Carbon Nanotubes. *Journal of Physical Chemistry B* **2010,** *114* (29), 9435-9444.

190. Baskaran, D.; Mays, J. W.; Bratcher, M. S., Noncovalent and nonspecific molecular interactions of polymers with multiwalled carbon nanotubes. *Chemistry of Materials* **2005,** *17* (13), 3389-3397.

191. O'Connell, M. J.; Boul, P.; Ericson, L. M.; Huffman, C.; Wang, Y. H.; Haroz, E.; Kuper, C.; Tour, J.; Ausman, K. D.; Smalley, R. E., Reversible water-solubilization of single-walled carbon nanotubes by polymer wrapping. *Chemical Physics Letters* **2001,** *342* (3-4), 265-271.

192. Lorenzo, A. T.; Arnal, M. L.; Albuerne, J.; Muller, A. J., DSC isothermal polymer crystallization kinetics measurements and the use of the Avrami equation to fit the data: Guidelines to avoid common problems. *Polym. Test* **2007,** *26* (2), 222-231.

193. Lin, C. C., THE RATE OF CRYSTALLIZATION OF POLY(ETHYLENE-TEREPHTHALATE) BY DIFFERENTIAL SCANNING CALORIMETRY. *Polym. Eng. Sci.* **1983,** *23* (3), 113-116.

194. Haggenmueller, R.; Fischer, J. E.; Winey, K. I., Single wall carbon nanotube/polyethylene nanocomposites: Nucleating and templating polyethylene crystallites. *Macromolecules* **2006,** *39* (8), 2964-2971.

195. Trujillo, M.; Arnal, M. L.; Mueller, A. J.; Bredeau, S.; Bonduel, D.; Dubois, P.; Hamley, I. W.; Castelletto, V., Thermal Fractionation and isothermal crystallization of polyethylene nanocomposites prepared by in situ polymerization. *Macromolecules* **2008,** *41* (6), 2087-2095.

196. Liu, S. Y.; Yu, Y. N.; Cui, Y.; Zhang, H. F.; Mo, Z. S., Isothermal and nonisothermal crystallization kinetics of nylon-11. *Journal of Applied Polymer Science* **1998,** *70* (12), 2371-2380.

197. Run, M. T.; Yao, C. G.; Wang, Y. J., Morphology, isothermal and non-isothermal crystallization kinetics of poly(methylene terephthalate). *European Polymer Journal* **2006,** *42* (3), 655-662.

198. Geng, H. Z.; Rosen, R.; Zheng, B.; Shimoda, H.; Fleming, L.; Liu, J.; Zhou, O., Fabrication and properties of composites of poly(ethylene oxide) and functionalized carbon nanotubes. *Advanced Materials* **2002,** *14* (19), 1387-1390.

199. Jung, Y. C.; Muramatsu, H.; Park, K. C.; Shimamoto, D.; Kim, J. H.; Hayashi, T.; Song, S. M.; Kim, Y. A.; Endo, M.; Dresselhaus, M. S., Transparent and Conductive Polyethylene Oxide Film by the Introduction of Individualized Single-Walled Carbon Nanotubes. *Macromolecular Rapid Communications* **2009,** *30* (24), 2084-2088.

200. Jeong, H. K.; Lee, Y. P.; Lahaye, R.; Park, M. H.; An, K. H.; Kim, I. J.; Yang, C. W.; Park, C. Y.; Ruoff, R. S.; Lee, Y. H., Evidence of graphitic AB stacking order of graphite oxides. *J. Am. Chem. Soc.* **2008,** *130* (4), 1362-1366.

201. Buchsteiner, A.; Lerf, A.; Pieper, J., Water dynamics in graphite oxide investigated with neutron scattering. *J. Phys. Chem. B* **2006,** *110* (45), 22328-22338.

202. Hontorialucas, C.; Lopezpeinado, A. J.; Lopezgonzalez, J. D. D.; Rojascervantes, M. L.; Martinaranda, R. M., STUDY OF OXYGEN-CONTAINING GROUPS IN A SERIES OF GRAPHITE OXIDES - PHYSICAL AND CHEMICAL CHARACTERIZATION. *Carbon* **1995,** *33* (11), 1585-1592.

203. Guo, H. L.; Wang, X. F.; Qian, Q. Y.; Wang, F. B.; Xia, X. H., A Green Approach to the Synthesis of Graphene Nanosheets. *ACS Nano* **2009,** *3* (9), 2653-2659.

204. Stankovich, S.; Dikin, D. A.; Piner, R. D.; Kohlhaas, K. A.; Kleinhammes, A.; Jia, Y.; Wu, Y.; Nguyen, S. T.; Ruoff, R. S., Synthesis of graphene-based nanosheets via chemical reduction of exfoliated graphite oxide. *Carbon* **2007,** *45* (7), 1558-1565.

205. Yang, S. B.; Cui, G. L.; Pang, S. P.; Cao, Q.; Kolb, U.; Feng, X. L.; Maier, J.; Mullen, K., Fabrication of Cobalt and Cobalt Oxide/Graphene Composites: Towards High-Performance Anode Materials for Lithium Ion Batteries. *Chemsuschem* **2010,** *3* (2), 236-239.

206. He, Y.; Huang, L.; Cai, J. S.; Zheng, X. M.; Sun, S. G., Structure and electrochemical performance of nanostructured Fe3O4/carbon nanotube composites as anodes for lithium ion batteries. *Electrochimica Acta* **2010,** *55* (3), 1140-1144.

207. Muraliganth, T.; Murugan, A. V.; Manthiram, A., Facile synthesis of carbon-decorated single-crystalline Fe3O4 nanowires and their application as high performance anode in lithium ion batteries. *Chem. Commun.* **2009,** (47), 7360-7362.

208. Zhang, W. M.; Wu, X. L.; Hu, J. S.; Guo, Y. G.; Wan, L. J., Carbon Coated Fe3O4 Nanospindles as a Superior Anode Material for Lithium-Ion Batteries. *Advanced Functional Materials* **2008,** *18* (24), 3941-3946.

209. Ji, L. W.; Tan, Z. K.; Kuykendall, T. R.; Aloni, S.; Xun, S. D.; Lin, E.; Battaglia, V.; Zhang, Y. G., Fe3O4 nanoparticle-integrated graphene sheets for high-performance half and full lithium ion cells. *Physical Chemistry Chemical Physics* **2011,** *13* (15), 7139-7146.

210. Li, B. J.; Cao, H. Q.; Shao, J.; Qu, M. Z.; Warner, J. H., Superparamagnetic Fe3O4 nanocrystals@graphene composites for energy storage devices. *Journal of Materials Chemistry* **2011,** *21* (13), 5069-5075.

211. Liu, H.; Wang, G. X.; Wang, J. Z.; Wexler, D., Magnetite/carbon core-shell nanorods as anode materials for lithium-ion batteries. *Electrochemistry Communications* **2008,** *10* (12), 1879-1882.

212. Ban, C. M.; Wu, Z. C.; Gillaspie, D. T.; Chen, L.; Yan, Y. F.; Blackburn, J. L.; Dillon, A. C., Nanostructured Fe3O4/SWNT Electrode: Binder-Free and High-Rate Li-Ion Anode. *Advanced Materials* **2010,** *22* (20), E145-+.

213. Yuan, S. M.; Zhou, Z.; Li, G., Structural evolution from mesoporous alpha-Fe2O3 to Fe3O4@C and gamma-Fe2O3 nanospheres and their lithium storage performances. *Crystengcomm* **2011,** *13* (14), 4709-4713.

VITA

IL TAE KIM

IL TAE KIM was born in Seoul, South Korea. He received a B.S. in Chemical and Biological Engineering from Korea University, Seoul, South Korea in 2004, and M.S. in Chemical and Biomolecular Engineering from Korea Advanced Institue of Science and Technology (KAIST) in 2006. He then went on to Georgia Institute of Technology to receive his PhD in Materials Science Engineering in 2011.